FIRE-ASSOCIATED CHANGE IN SURFACE AND FROZEN GROUND CONDITIONS IN NUNATSIAVUT, LABRADOR

YIFENG WANG

Thesis submitted to the University of Ottawa
in partial fulfillment of the requirements for the
Master of Science degree in Geography

Department of Geography, Environment and Geomatics
Faculty of Arts
University of Ottawa

ABSTRACT

Forest fires are a significant natural surface disturbance to permafrost landscapes. However, post-fire permafrost literature is mainly derived from research in the western North American boreal forest. This thesis research, conducted in collaboration with a multi-disciplinary, multi-institutional team of researchers, is the first investigation of post-fire frozen ground conditions in the coastal boreal forests of the eastern Canadian subarctic, where precipitation amounts are greater and fire intervals are much longer than in the West.

Ground thermal conditions and related environmental variables were evaluated from summer and winter measurements at three historic forest fire sites in Nunatsiavut, coastal Labrador. Electrical resistivity tomography was used to assess the presence and distribution of frozen ground. Abiotic and biotic variables, thought to be associated with post-fire permafrost persistence, were subject to a series of exploratory data analyses, including a Principal Components Analysis (PCA). Based on the literature, it was hypothesized that ground temperatures would be lower in the undisturbed, closed-canopy forest than in the adjacent burned areas, due to greater interception of snow, a thick and undisturbed organic mat, and greater shading of the ground. Burned areas were expected to have lesser organic mat thicknesses and greater shrub cover. It was expected that permafrost, if present, would be located beneath forest cover, while degrading in the burned areas. Numerical modelling was also performed for two of the sites to investigate future change in post-fire ground thermal conditions as the climate warms.

Frozen ground conditions varied at the three sites. Near Nain, some patches of perennially frozen ground were identified in the undisturbed sections along the transects, with their presence and persistence relating to the intact canopy cover and the fine-grained sediments. Thermal modelling simulations to the end of this century demonstrated the resilience of this thin permafrost to at least 2060, even when subjected to fire disturbance and continued climate warming. No

permafrost was identified along the transects at the southernmost site near Postville, reflecting the warmer climate at this site. Post-fire vegetation cover at all three sites was dominated by shrubs, but their snow-trapping effect, which is commonly observed in tundra environments, was limited by the deep (>1.3 m) snow cover throughout the sites and the presence of other erect vegetation, including regenerating trees or standing dead. The PCA did not reveal consistent associations between any of the biotic or abiotic variables, reflecting the complexity of the post-fire ecosystem. However, the PCA did show that burned sections differ in terms of canopy cover and snow depth, underlining the critical role of an intact forest canopy in the ecological protection of sensitive, discontinuous permafrost. Despite the absence of clear links between the variables, this research provides important first insights into fire-associated ecosystem change and its impact on permafrost in eastern Canada.

ACKNOWLEDGEMENTS

I would like to thank Polar Knowledge Canada, the Northern Scientific Training Program, the Natural Sciences and Engineering Council of Canada, and the W. Garfield Weston Foundation for their generous financial support of this research. My master's experience was also greatly enriched by support provided through the RemoteEx Partnership Exchange Programme and Transport Canada's Northern Transportation Adaptation Initiative.

Thank you to my supervisor, Dr. Antoni Lewkowicz, for providing a positive and supportive learning experience and for your unwavering confidence in my abilities. I appreciate your advice, guidance, and expertise, and I thank you for sharing your passion for permafrost with me. I would also like to thank my committee members, Dr. Denis Lacelle and Dr. Konrad Gajewski, for their guidance throughout this process. Denis, thank you for all of the opportunities that you have provided to me, from taking me on as a student during my B.Sc. to bringing me along as a field assistant during my M.Sc. Konrad, thank you for welcoming me into the LPC and for providing me with the resources to complete my thesis. This would not have been possible without your generosity.

I am grateful to Paul Sokoloff for showing me how to differentiate between black and white spruce, Brittany Main for teaching me how to dig and sample snow pits, and Dr. Anders Knudby for providing access to his computing resources. I would like to thank Mr. Jean Bjornson for his assistance with my laboratory-based analyses and field logistics. I am also grateful to Dr. Luke Copland for generously equipping me with winter field gear from the LCR and for always making time for a quick chat. Thank you to my office mates and fellow basement and sub-basement dwellers for the snack runs – a dozen Subway cookies never seems like too many when they are shared with colleagues and friends like you.

I feel very lucky to have had the opportunity to work with such a wonderful group of researchers from the Food, Fire, and Ice Team, led by Dr. Carissa Brown. To Dr. Luise Hermanutz, Dr. Alain Cuerrier, and Lucas Brehaut, thank you for teaching me the tips and tricks of living inside a bug jacket and for carrying cables and electrodes through the burn woods. I am especially thankful to the world's best field partner, Frédéric Dwyer-Samuel, for always being ready for a day of frost probing or snow pit digging. Our hikes have brought me to some of my favourite spots in Nunatsiavut, and I now always associate apple crumble with Nain. I am also very grateful to Dr. Robert Way for sharing his expertise and knowledge of permafrost science, fieldwork, and Labrador.

Thank you for not openly judging me for being bad at snowmobiling – maybe I'll go above 30 km/h next time (unlikely).

This research would not have been possible without the in-kind support provided by Caitlin Lapalme and by Liz Pijogge, Carla Pamak, Paul McCarney, and Rodd Laing from the Nunatsiavut Government and Research Centre. To Harold, Shirley, and Jim, your kindness and hospitality make Postville feel like a home away from home. Ches, thank you for sharing your knowledge of the land. Joe, thank you for always staying nearby.

I am also incredibly thankful for the network of friends that I have had the privilege of meeting over the past two years. To my climbing and camping crew, thank you for the adventures and for pushing me to top out, rather than tap out. Francois, thank you for pretending to care about taliks as much as I do. Thank you to Patricia, Michelle, Megan, Kayla, Chaim, and Brianna for always welcoming me back to Labrador with open arms.

Finally, mom, dad, and sis, thank you for your unconditional love and for supporting my dreams to *zuo da chuan*, *chi can guan*, *zhu lu guan*.

« *D'où vient donc l'étrange attirance de ces régions polaires, si puissante, si tenace qu'après en être revenu on oublie les fatigues morales et physiques pour ne songer qu'à retourner vers elles?* »

Jean-Baptiste Charcot

TABLE OF CONTENTS

LIST OF FIGURES

LIST OF TABLES

LIST OF ABBREVIATIONS

a.s.l.	above sea level
BEST	Berkeley Earth Surface Temperature
BP	before present
BR	Beaver River
c_f	frozen heat capacity
c_{ice}	volumetric heat capacity of ice
c_{min}	volumetric heat capacity of mineral material
c_{org}	volumetric heat capacity of organic material
CSV	comma separated values
c_u	unfrozen heat capacity
c_{water}	volumetric heat capacity of water
dBD	dry bulk density
DW	dry weight/mass
ERT	electrical resistivity tomography
FDD	freezing degree days
GIPL	Geophysical Institute Permafrost Laboratory
GMC	gravimetric moisture content
k_f	frozen thermal conductivity
k_{ice}	thermal conductivity of ice
k_{min}	thermal conductivity of mineral material
k_{org}	thermal conductivity of organic material
k_u	unfrozen thermal conductivity
k_{water}	thermal conductivity of water
LIS	Laurentide Ice Sheet
LOI	loss on ignition
MAAT	mean annual air temperature
MAGST	mean annual ground surface temperature
NEST	Northern Ecosystem Soil Temperature
n_f	freezing n-factor
n_t	thawing n-factor
RCP	representative concentration pathway
SDD	snow depth days
SWE	snow water equivalent
TB	Tikkoatokak Bay
TDD	thawing degree days
TTOP	temperature at top of permafrost
UAV	unmanned aerial vehicle
V	volume
VMC	volumetric moisture content
WB	Webb Bay
WW	wet weight/mass

LIST OF EQUATIONS

$$surface\ offset\ (°C) = MAGST\ (°C) - MAAT\ (°C) \tag{1-1}$$

$$thermal\ offset\ (°C) = TTOP\ (°C) - MAGST\ (°C) \tag{1-2}$$

$$GMC\ (g/g) = \frac{WW\ (g) - DW(g)}{DW\ (g)} \tag{3-1}$$

$$organic\ matter\ content\ (\%) = LOI_{550}(\%) = \frac{DW_{105}\ (g) - DW_{550}\ (g)}{DW_{105}\ (g)} \times 100\ \% \tag{3-2}$$

$$dBD_{org-min}\ (g/cm^3) = 0.075\ +\ 1.301^{-0.06 \times organic\ matter\ content\ (\%)} \tag{3-3}$$

$$dBD_{org}\ (g/cm^3) = \frac{DW(g)}{V\ (cm^3)} \tag{3-4}$$

$$VMC\ (cm^3/cm^3) = GMC\ (g/g) \times dBD\ (g/cm^3) \tag{3-5}$$

$$\begin{aligned} &volumetric\ organic\ content\ (cm^3/cm^3) \\ &\quad = gravimetric\ organic\ content\ (g/g) \times dBD\ (g/cm^3) \end{aligned} \tag{3-6}$$

$$\begin{aligned} &volumetric\ mineral\ content\ (cm^3/cm^3) \\ &\quad = 1 - (volumetric\ organic\ content\ (cm^3/cm^3) \\ &\quad + VMC\ (cm^3/cm^3)) \end{aligned} \tag{3-7}$$

$$\begin{aligned} k_f(W/m/K) &= {fraction_{org}}^{k_{org}(W/m/K)} \times {fraction_{min}}^{k_{min}(W/m/K)} \\ &\quad \times {fraction_{ice}}^{k_{ice}(W/m/K)} \end{aligned} \tag{3-8}$$

$$\begin{aligned} k_u(W/m/K) &= {fraction_{org}}^{k_{org}(W/m/K)} \times {fraction_{min}}^{k_{min}\ (W/m/K)} \\ &\quad \times {fraction_{water}}^{k_{water}(W/m/K)} \end{aligned} \tag{3-9}$$

$$\begin{aligned} c_f(MJ/m^3/K) &= \left(fraction_{org} \times c_{org}\ (MJ/m^3/K)\right) \\ &\quad + (fraction_{min} \times c_{min}\ (MJ/m^3/K)) \\ &\quad + (fraction_{ice} \times c_{ice}\ (MJ/m^3/K)) \end{aligned} \tag{3-10}$$

$$c_u(MJ/m^3/K) = \left(fraction_{org} \times c_{org}\ (MJ/m^3/K)\right) + (fraction_{min} \times c_{min}\ (MJ/m^3/K)) + (fraction_{water} \times c_{water}\ (MJ/m^3/K)) \tag{3-11}$$

$$n_f = \frac{FDD_{ground\ surface}\ (degree\ days)}{FDD_{air}\ (degree\ days)} \tag{3-12}$$

$$n_t = \frac{TDD_{ground\ surface}\ (degree\ days)}{TDD_{air}\ (degree\ days)} \tag{3-13}$$

CHAPTER 1 : INTRODUCTION

1.1 Introduction

Permafrost, or perennially frozen ground, is a geological and climatological phenomenon that refers to ground or earth materials that remain at or below 0°C for at least two consecutive years. Permafrost can be classified by its thickness and extent into zones of continuous, extensive discontinuous, sporadic discontinuous, and isolated patches of permafrost (Heginbottom et al., 1995). However, its extent and thickness, and therefore its distribution and stability, are intricately linked with past and present conditions in the physical landscape, climate, and vegetation of the surrounding environment.

Permafrost distribution, particularly in the northern hemisphere, relies on a combination of regional relief, aspect, ground material properties, vegetation, snow cover, and hydrology (French, 2017). This thesis concerns the presence and post-disturbance response of frozen ground in forested lowland locations in coastal Labrador, Canada. The distribution and persistence of permafrost in coastal Labrador, to a southern limit of 51.4°N (Heginbottom et al., 1995), is primarily linked to the climatic influence of the cold Labrador Current, which carries Arctic waters down the eastern coast of mainland Canada (Foster 1983; Banfield and Jacobs, 1998; Roberts et al., 2006). In Labrador, permafrost is primarily found in tundra and unvegetated areas with relatively thin snow cover (Way and Lewkowicz, 2018). However, permafrost has also been detected under forest cover in northern and central coastal Labrador (Way et al., in preparation), and under thick layers of organic material in southern Labrador (Way and Lewkowicz, 2018; Way et al., 2018).

Other than coastal Labrador, the Kamchatka Peninsula and the Bristol Bay region of southwestern Alaska are some of the only other coastal regions in the northern hemisphere where permafrost exists south of 60°N (Figure 1-1). Understanding the drivers of permafrost distribution in these comparable regions helps to contextualize the permafrost in coastal Labrador (Table 1-1).

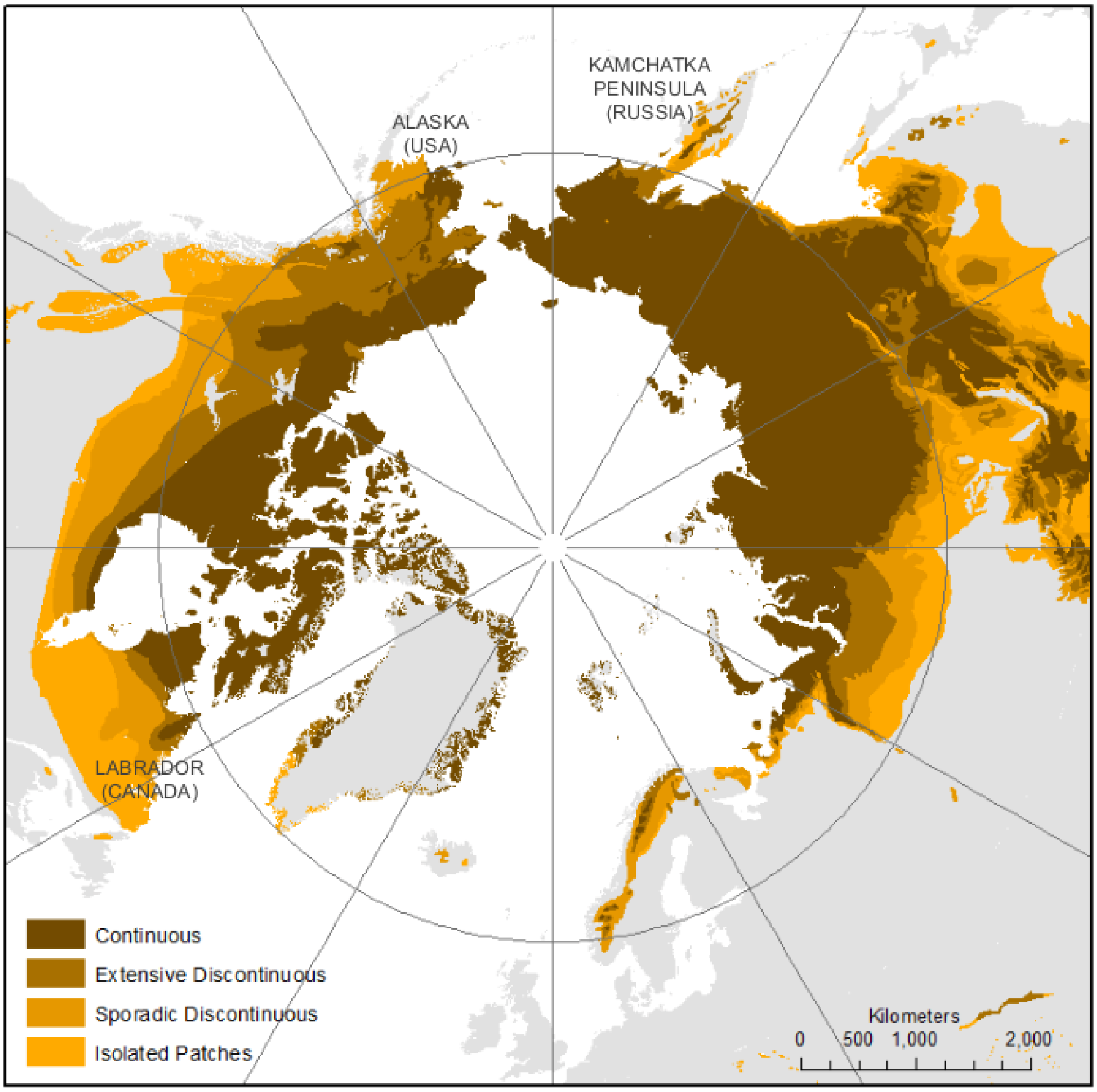

Figure 1-1. Distribution of Permafrost Zones in the Northern Hemisphere (Brown et al., 2002). Comparable low latitude (south of 60°N) coastal permafrost regions to Labrador are labelled and identified. Parallel at 60°N is identified by a grey line.

Table 1-1. Comparison of Low Latitude (south of 60°N) Coastal Permafrost Regions in the Northern Hemisphere.

Region	Temperature of Adjacent Ocean Masses and Currents	Permafrost Presence in Lowland Locations	Permafrost Presence in Elevated Regions	Permafrost Distribution Patterns	Selected Relevant References
Coastal Labrador (Canada)	COLD	YES	YES	Permafrost is primarily found in tundra and unvegetated sites with little snow cover. Permafrost can also be found in some forested locations, and in locations with thick organic mats in southern Labrador.	Bell et al., 2011; Way & Lewkowicz, 2016; Way & Lewkowicz, 2018
Kamchatka Peninsula (Russia)	COLD	NO	YES	Permafrost is found in elevated regions with little snow cover.	Sone et al., 2006; Abramov et al., 2008; Bakalin & Vetrova, 2008; Fukui et al., 2008; Jones & Solomina, 2015
Bristol Bay Region on Alaska Peninsula (USA)	WARM and COLD	YES	YES	Permafrost is found in elevated regions. In lowland regions, permafrost is found in areas with favourable sediments, little snow cover, and thick organic mats.	Muller, 1955; Pastick et al., 2015

The Kamchatka Peninsula in Russia is the most comparable region to Labrador in terms of latitude. It is a mountainous region, bordered to the east by the Bering Sea and the Pacific Ocean and to the west by the Sea of Okhotsk (Jones and Solomina, 2015). As with Labrador, its climate is linked to the influence of cold ocean currents, but despite this, little permafrost is reported south of 57°N (Fukui et al., 2008; Jones and Solomina, 2015). North of 57°N, discontinuous permafrost is present at elevations above several hundred m a.s.l. in the mountainous central and northern parts of the peninsula (Sone et al., 2006; Abramov et al., 2008; Bakalin and Vetrova, 2008; Jones and Solomina, 2015). The lack of permafrost below this latitudinal and altitudinal boundary is attributed to mild winters and deep snow cover (Jones and Solomina, 2015). In coastal Labrador, permafrost persists at both lower latitudes and elevations (Bell et al., 2011; Way and Lewkowicz, 2016; Way and Lewkowicz, 2018; Way et al., 2018).

Coastal Alaska, on the western edge of the North American continent, also exhibits permafrost at latitudes south of 60°N. Permafrost distribution in Alaska is generally controlled by a combination of low mean annual air temperatures and little winter and annual precipitation (Pastick et al., 2015). In the Bristol Bay region, at the northern neck of the Alaska Peninsula, discontinuous permafrost is mainly present in lowland areas with relatively shallow snow cover, favourable ground materials like silt and fine sand, and a thick organic mat (Muller, 1955). In winter, many lowland sections in this region of coastal Alaska are blown free of snow, permitting permafrost persistence at latitudes south of 60°N (Muller, 1955). Further south along the Alaska Peninsula, the influence of the warm Alaska Current causes higher mean annual air temperatures and greater annual precipitation, which are not favourable for permafrost formation or persistence (Muller, 1955).

The consideration of permafrost distribution in eastern Russia and southwestern Alaska, (Table 1-1), helps place that of coastal Labrador in a geographic context (Figure 1-1). Permafrost in these coastal, low latitude regions is particularly susceptible to climate warming. Rapid changes to permafrost environments have been observed and predicted throughout the North, through warming of ground temperatures and degradation and loss of frozen ground in both discontinuous and continuous permafrost zones (Anisimov and Nelson, 1997).

The response of permafrost to current climate warming trends can be complicated by surface disturbance, such as forest fire. Forest fires, which are the most widespread natural surface disturbance to discontinuous permafrost, destroy vegetation and organic matter, which are important natural buffers to the ground (Barrett et al., 2010). Fire is a common and natural element of the boreal forest ecosystem, but recent climatic warming, associated with prolonged droughts and more severe thunderstorm activity (Nash and Johnson, 1996), has resulted in changed fire regimes (Flannigan et al., 2005). The number of fires and the corresponding area burned in the Canadian boreal forest has increased and is projected to continue to grow through the rest of this century (Flannigan et al., 2005; Balshi et al., 2009; Wotton et al., 2010). This trend is especially apparent in the continental boreal forests of western Canada and Alaska (Holloway et al., 2020), where the fire interval is reported to be as short as 50 to 150 years (Coops et al., 2018). In contrast, there have been no previous investigations of frozen ground conditions following fire in the northeastern Canadian boreal forest. The main objective of this dissertation is to address the current gap in post-fire permafrost literature for the eastern Canadian subarctic. This information will improve our understanding of how frozen ground responds to forest fires in coastal Labrador.

1.2 Research Goals and Objectives

The goal of this thesis is to examine post-fire ground thermal conditions at three recent forest fire sites in Nunatsiavut, in coastal Labrador. This was achieved through three main research objectives:

1) To describe frozen ground conditions at each site. Subsurface conditions are portrayed along burned to unburned transects using geophysical surveys, validated by other permafrost field techniques (Chapter 4).
2) To investigate the major factors influencing ground thermal properties. Statistical analyses are used to examine relationships between ground conditions and other site characteristics, including snow depth, organic layer thickness, soil temperature and moisture, canopy cover, and shrub height and density, in both burned and unburned sections of the study sites (Chapter 4).

3) To model the long-term post-fire response of frozen ground at two of the sites under a warming climate. One-dimensional thermal modelling, based on field data, is used to hindcast changes in frozen ground conditions since the forest fire events and forecast future changes to 2100 under moderate and aggressive climate warming scenarios (Chapter 5). Modelling is not undertaken for the southernmost site (Beaver River) where permafrost does not appear to be extant.

This research enhances our understanding of the effects of forest fire disturbance on ground thermal conditions in the boreal forests of coastal Labrador. It was conducted in collaboration with a multi-disciplinary group of researchers from Memorial University, Université de Montréal, and Queen's University.

1.3 Background

1.3.1 Permafrost and the Ground Thermal Regime

Permafrost is defined as ground or earth materials that remain at or below a temperature of 0°C for at least two consecutive years. Permafrost is found in high latitude and/or high elevation regions (Heginbottom et al., 1995; Figure 1-1), where low air temperatures and other associated climatic variables favour its formation and persistence.

At all scales, the surface energy balance controls ground temperatures and the ground thermal regime. At a regional scale, the distribution of permafrost is closely related to the mean annual air temperature (MAAT) isotherms. For example, the southern boundary of the continuous permafrost zone generally corresponds to the -8°C isotherm (Heginbottom et al., 1995). At a local scale, however, the relationship between mean annual air temperature and the ground thermal regime is complicated by other environmental and ecosystem-related variables, including snow cover, vegetation cover, organic layer thickness, and soil thermal conductivity (Williams and Smith, 1989;

French, 2017). At a given site, the structure and state of permafrost can be conceptualized as being linked to surface and thermal offsets, based on relationships between the MAAT, the mean annual ground surface temperature (MAGST), and the temperature at the top of the permafrost (TTOP) (Smith and Riseborough, 2002; Figure 1-2).

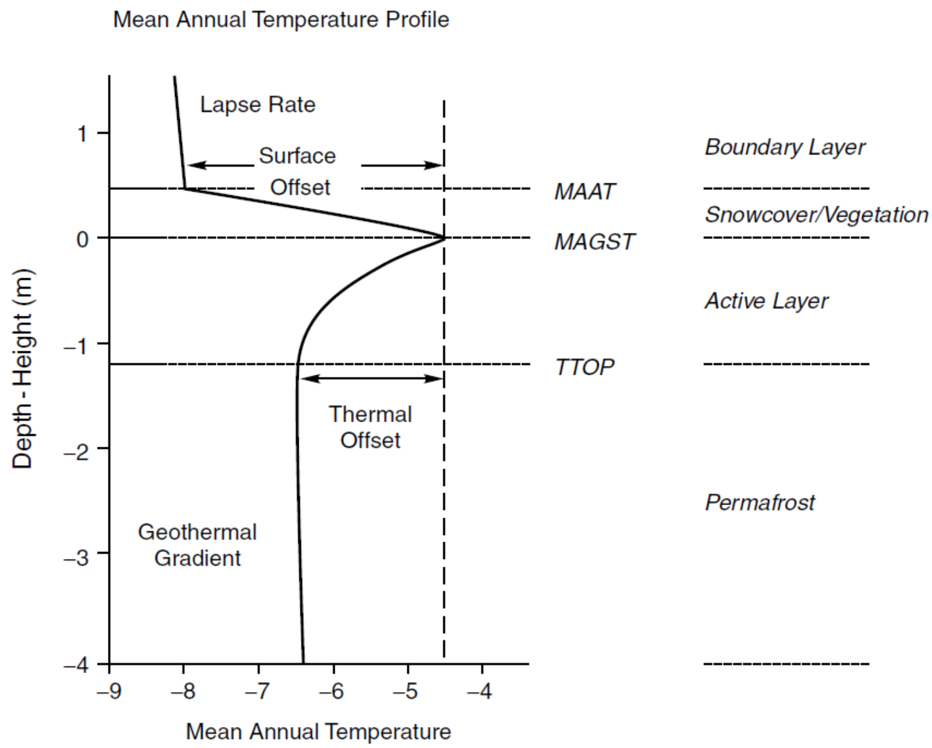

Figure 1-2. Idealized Schematic of Mean Annual Air, Ground Surface, and Ground Temperatures (from Smith and Riseborough, 2002).

The surface offset is defined as:

$$surface\ offset\ (°C) = MAGST\ (°C) - MAAT\ (°C) \qquad (1\text{-}1)$$

It is a combination of the vegetation offset, based on the cooling effects of vegetation shading during summer, and the nival offset, representing the insulating effects of snow cover during winter (Smith and Riseborough, 2002). During summer, vegetation decreases ground surface temperatures through interception of incoming solar radiation and evapotranspiration processes (Williams and Smith, 1989; Smith and Riseborough, 2002). During winter, vegetation also indirectly influences ground surface temperatures by either intercepting falling snow, resulting in thinner snow cover and lower ground temperatures, or by trapping of blowing snow, resulting in thicker snow cover and higher ground temperatures (Sturm et al., 2005; Lawrence and Swenson, 2011). At most sites, the surface offset is dominated by this nival offset, so the MAGST tends to be greater than the MAAT (Smith and Riseborough, 2002). The nival offset is responsible for patterns of permafrost distribution at the boundary between the continuous and discontinuous permafrost zones (Smith and Riseborough, 2002).

Further south, in regions with less favourable climate conditions, permafrost is primarily restricted to peatland locations (Zoltai, 1972; Payette et al., 2004). Permafrost occurrence in these regions is largely attributed to the thermal offset (Smith and Riseborough, 2002; Shur and Jorgenson, 2007), which is defined as:

$$thermal\ offset\ (°C) = TTOP\ (°C) - MAGST\ (°C) \qquad (1\text{-}2)$$

The thermal offset is controlled by the difference in soil thermal conductivity when frozen and unfrozen (Williams and Smith, 1989), due to the higher thermal conductivity of ice (2.230 W/m/K) compared to that of water (0.605 W/m/K; Johnston, 1981). At low moisture contents, frozen and unfrozen thermal conductivities do not differ significantly (Burn and Smith, 1988), so little or no thermal offset is expected (e.g., in massive bedrock). In contrast, the variation in moisture contents and thermal conductivities of organic materials is much greater, resulting in a large thermal offset. A thick organic mat discourages heat penetration in summer and promotes heat loss in winter, ultimately favouring lower mean annual ground temperatures (Williams and Smith, 1989).

The ground thermal regime at a given site can be visualized from trumpet curves, composed of annual minimum and maximum temperatures that converge at the depth of zero annual amplitude (Figure 1-3). The depths of the base of the active layer, the top of the permafrost, and the base of the permafrost can also be identified from such trumpet curves (Figure 1-4).

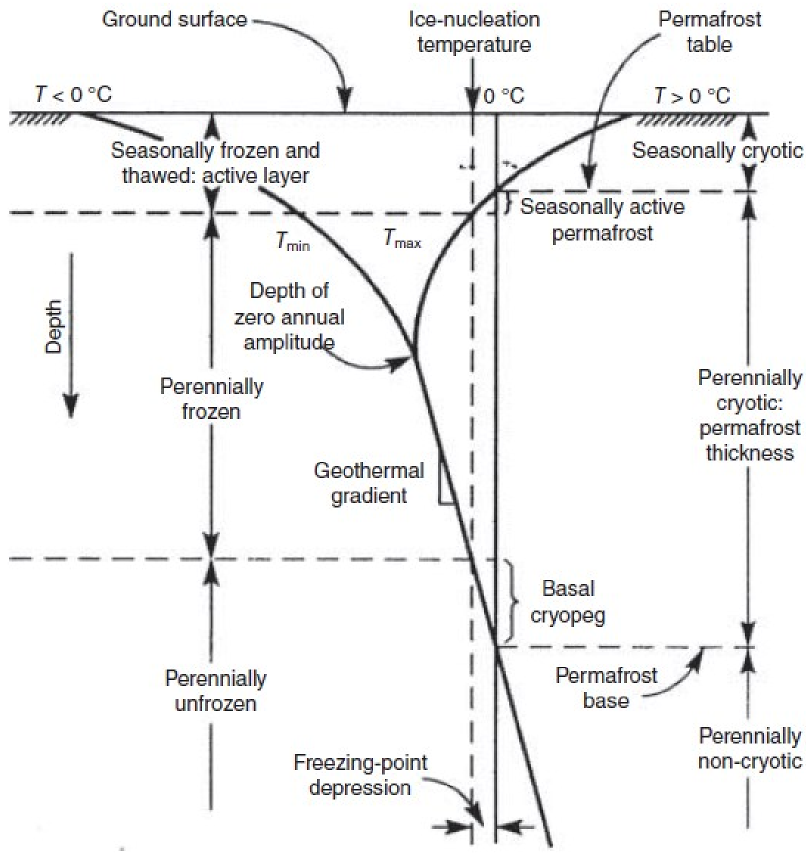

Figure 1-3. Schematic of the Ground Thermal Regime (from French, 2017, after Ferrians et al., 1969).

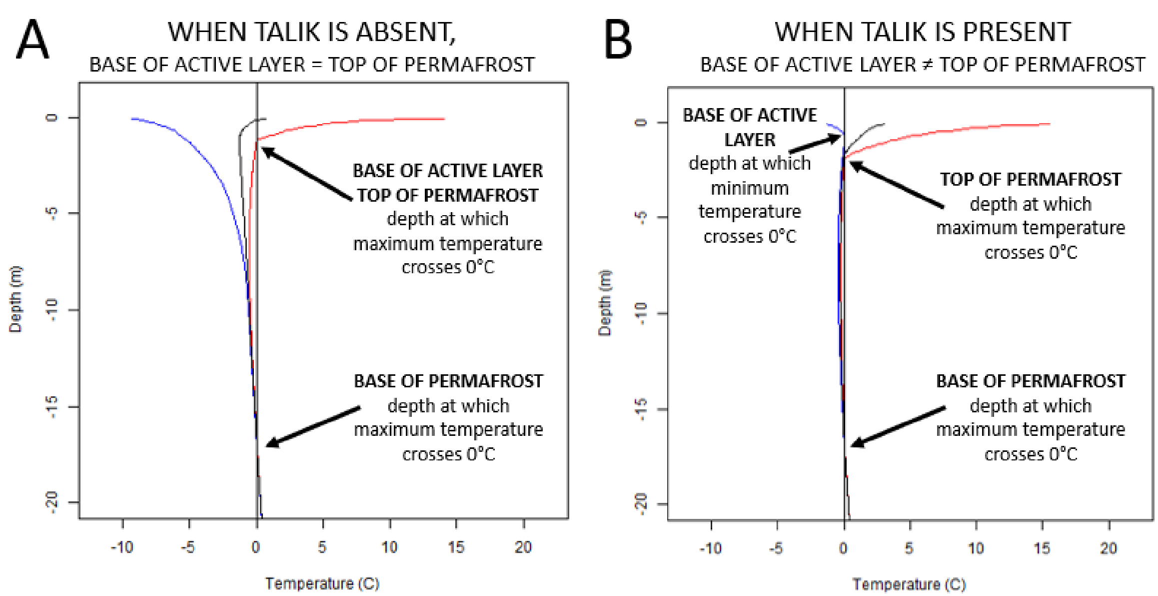

Figure 1-4. Identification of Base of Active Layer, Top of Permafrost, Base of Permafrost, and Talik A) Absence or B) Presence using Trumpet Curves. Annual maximum, mean, and minimum temperature curves are shown in red, black, and blue, respectively.

The depth of zero annual amplitude is the depth at which the range between the maximum and minimum temperatures converges to less than 0.1 K. This represents the shallowest depth at which seasonal variation in the air temperature no longer influences ground temperature. The temperature at the depth of zero annual amplitude is conventionally referred to as the mean annual ground temperature (MAGT).

The top of the permafrost is defined as the depth at which the maximum temperature curve crosses 0°C. At most sites, the top of permafrost coincides with the base of the active layer (Figure 1-4-A), which is defined as the layer of ground that undergoes annual thawing and freezing. In the absence of a talik, which is a body of perennially unfrozen ground, the base of the active layer represents the depth to which seasonal thawing occurs. However following surface disturbance and/or climate warming, a supra-permafrost talik may develop. When a talik is present, the base of the active layer is defined as the depth at which the minimum temperature curve exceeds 0°C, i.e., the depth to which seasonal freezing occurs (Figure 1-4-B).

The base of the permafrost is defined as the depth at which the maximum temperature curve crosses 0°C. Below the base of permafrost, the ground is unfrozen, due to the geothermal heat flux.

1.3.2 Permafrost Classification

Shur and Jorgenson (2007) summarized the effects of climate warming and ecosystem disturbance and succession on perennially frozen ground by defining five main classes of permafrost: 1) climate-driven permafrost; 2) climate-driven, ecosystem-modified permafrost; 3) climate-driven, ecosystem-protected permafrost; 4) ecosystem-driven permafrost; and 5) ecosystem-protected permafrost (Figure 1-5). Classes 1 through 3 typically describe permafrost that formed under previous colder climate conditions. In certain cases, such as in deltas and other areas of new sedimentation, climate-driven permafrost aggradation can still occur under current climate conditions. Climate-driven, ecosystem-modified permafrost is affected by ecological succession, resulting in change to the permafrost thickness and temperature, such as by thickening of the organic layer. Climate-driven, ecosystem-protected permafrost is presently buffered by ecological succession, despite warmer climate conditions that are unfavourable for permafrost formation and persistence. Ecosystem-driven permafrost is formed as a direct result of ecological succession. Ecosystem-protected permafrost is similar to climate-driven, ecosystem-protected permafrost, in that it formed under colder climate conditions, but its persistence is directly attributed to the later stages of ecological succession. Ecosystem-protected permafrost is the most sensitive of the five classes, as it cannot be re-established following disturbance, such as forest fire.

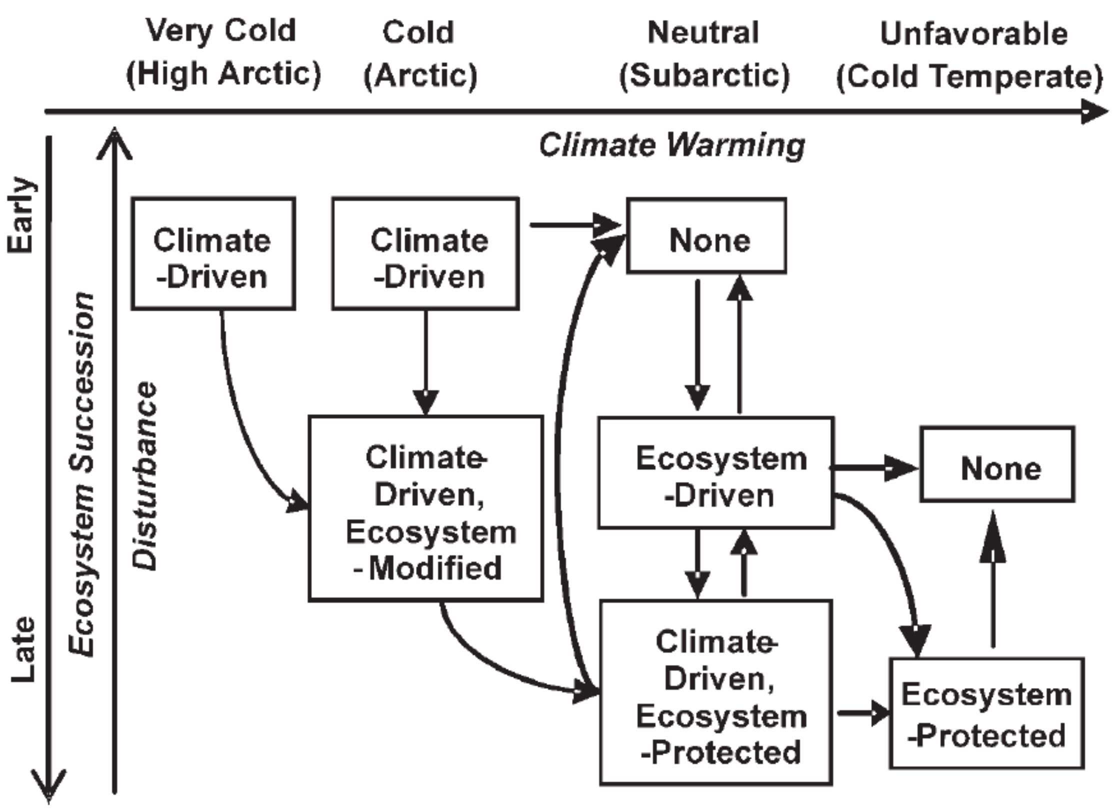

Figure 1-5. Classification of Permafrost According to Climate, Disturbance, and Ecological Succession Conditions (from Shur and Jorgenson, 2007).

1.3.3 Post-Fire Permafrost Response

Forest fires are widespread surface disturbances that can have both short- and long-term impacts on the ground thermal regime. Immediately following fire, increased heat penetration occurs during summer, while heat loss from the ground is reduced during winter (Gibson et al., 2018). These effects are attributed to post-fire loss of shade and snow-intercepting canopy, removal of insulating organic material, and lowering of site albedo due to darkening of the ground surface (Dyrness et al., 1986; Gibson et al., 2018). Post-fire increases in ground temperatures have been reported in permafrost regions throughout the North American boreal forest, particularly in Alaska and the Northwest Territories (Jafarov et al., 2013; Nossov et al., 2013; Fisher et al., 2016; Gibson et al., 2018; Holloway et al., 2020). This increase in ground temperatures causes thickening of the active layer (Holloway et al., 2020). In the western North American boreal forest, active layer thicknesses increase by approximately 60% within the first decade following fire, but they are reported to stabilize and return to pre-fire conditions within the next decade (Smith et al., 2015; Gibson et al., 2018; Holloway et al., 2020). In some cases, the net increase of heat flow into the ground also facilitates the development of supra-permafrost taliks that persist for several decades and that do not begin to recover until active layer thicknesses have returned to pre-fire conditions (Gibson et al., 2018). Some models also show enhanced post-fire permafrost thaw occurring from the base of permafrost (Zhang et al. 2015).

The impacts of fire disturbance on the ground thermal regime can last for decades (Holloway et al., 2020). Post-fire vegetation recovery has been modelled to occur along a two-segment linear pattern in which the forest canopy recovers to 66% of the pre-fire conditions over 25 years and achieves full recovery to pre-fire conditions during a second 25-year period (Zhang et al., 2015). This estimate accords with a remote sensing-based study that found that forests in central Labrador reached a standard 80% reforestation threshold after an average of 44 years following fire disturbance (Miranda et al., 2016). Following fire, ice-poor permafrost is subject to three potential trajectories (Figure 1-6), based on a combination of conditions during the pre-fire period, the fire disturbance itself, and the post-fire period (Holloway et al., 2020). In trajectory A, the active layer experiences temporary thickening. Active layer thicknesses may return to pre-fire conditions within the first decade following fire (Holloway et al., 2020). In trajectories B and C, the development of a supra-permafrost talik is initiated. This talik could recover, as outlined in trajectory B, or it could continue to deepen, potentially resulting in the total loss of permafrost, as outlined in trajectory C.

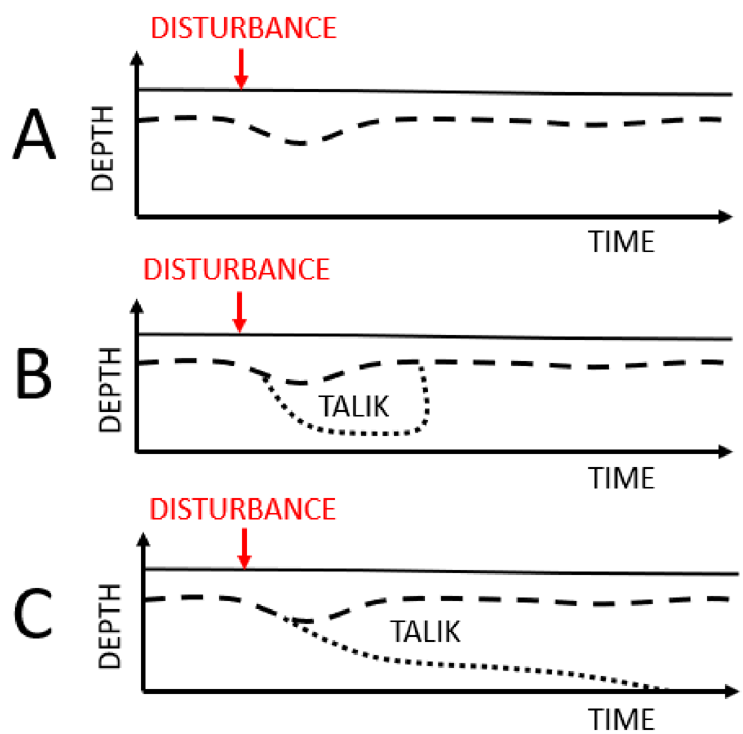

Figure 1-6. Schematic of Possible Post-Fire Trajectories of Ice-Poor Permafrost (adapted from Holloway et al., 2020). Trajectory A describes temporary thickening and deepening of the active layer. Trajectory B describes the development of a talik, followed by permafrost recovery. Trajectory C describes the development of a talik, followed by long-term permafrost degradation and possible loss of permafrost.

Permafrost modelling is a useful approach for providing insight into the response of frozen ground to various disturbances, over a variety of time scales. One-dimensional thermal modelling of the post-fire permafrost response has been applied in many studies within the North American boreal forest. The most frequently used models are NEST (Zhang et al., 2003) and GIPL (Marchenko et al., 2008). The NEST model has been applied to examine spatial and temporal effects of fire in forested and tundra regions in the Northwest Territories (Zhang et al., 2015), while GIPL has been used to investigate the effects of climate warming and fire disturbance on frozen ground in forested regions in Alaska (Jorgenson et al., 2010; Jafarov et al., 2013; Treat et al., 2013; Brown et al., 2015). TONE, developed by Goodrich (1978), is also commonly used in permafrost modelling applications, but it has never been used for post-fire simulations. Like post-fire permafrost field studies, modelling of post-fire ground conditions in the North American boreal forest are concentrated in the West, particularly in Alaska and the Northwest Territories (Holloway et al., 2020). No previous investigations of the long-term impacts of fire disturbance on ground thermal conditions have been conducted in the boreal forests of coastal Labrador.

1.4 Thesis Structure

This thesis consists of six chapters. This first chapter outlines the context and thesis objectives. Chapter 2 describes the climate, physical landscape, and vegetation of the coastal Labrador region and the study sites. The third chapter contains detailed descriptions and justifications for the methodology used. Chapters 4 and 5 constitute the results and correspond to two manuscripts that will be submitted to a peer-reviewed journal or conference proceedings publication volume. Chapter 4 is an exploratory analysis of ground, vegetation, and snow conditions at three recent forest fire sites in Nunatsiavut. Using a combination of field investigations, standard to permafrost science, ecology, and snow science, it provides a qualitative interpretation of inter-site differences and intra-site conditions, based on observations collected during both summer and winter. Forest canopy is identified as being critical to ground thermal conditions at the study sites, while the deep snowpack limits the impact of shrubs on the ground thermal regime. Chapter 4 was generated with guidance from co-authors Dr. Antoni Lewkowicz, Dr. Luise Hermanutz, and Dr. Robert Way. Chapter 5 contains a thermal modelling analysis of frozen ground conditions at two forest fire sites near Nain, Nunatsiavut. Numerical modelling using TEMP/W was applied to estimate the sensitivity and response of permafrost to fire disturbance under both moderate and aggressive climate warming scenarios. This contribution demonstrates that frozen ground in lowland forested regions in central coastal Nunatsiavut are resilient to fire disturbance, and, despite post-fire talik development, permafrost typically manages to recover from the degradational impacts of fire disturbance. The results from this analysis agree with similar post-fire permafrost modelling studies that demonstrate that fire accelerates the loss of permafrost, but that permafrost loss is ultimately attributed to an increase in air and ground temperatures. Chapter 5 was generated with guidance from co-authors Dr. Antoni Lewkowicz, Jean Holloway, and Dr. Robert Way. Finally, Chapter 6 contains concluding statements and a discussion of the limitations of this research.

1.5 References

Abramov, A., Gruber, S., Gilichinsky, D. (2008). Mountain Permafrost on Active Volcanoes: Field Data and Statistical Mapping, Klyuchevskaya Volcano Group, Kamchatka, Russia. *Permafrost and Periglacial Processes*, 19: 261-277.

Anisimov, O.A. and Nelson, F.E. (1997). Permafrost Zonation and Climate Change in the Northern Hemisphere: Results from Transient General Circulation Models. *Climatic Change*, 35: 241-258.

Bakalin, V.A. and Vetrova, V.P. (2008). Vegetation-Permafrost Relationships in the Zone of Sporadic Permafrost Distribution in the Kamchatka Peninsula. *Russian Journal of Ecology*, 39(5): 318-326.

Balshi, M.S., McGuire, D., Duffy, P., Flannigan, M., Walsh, J., Melillo, J. (2009). Assessing the Response of Area Burned to Changing Climate in Western Boreal North America Using a Multivariate Adaptive Regression Splines (MARS) Approach. *Global Change Biology*, 15: 578-600.

Banfield, C.E. and Jacobs, J.D. (1998). Regional Patterns of Temperature and Precipitation for Newfoundland and Labrador During the Past Century. *The Canadian Geographer/Le Géographe canadien*, 42(4): 354-364.

Barrett, K., Kasischke, E.S., McGuire, A.D., Turetsky, M.R., Kane, E.S. (2010). Modeling Fire Severity in Black Spruce Stands in the Alaskan Boreal Forest Using Spectral and Non-Spectral Geospatial Data. *Remote Sensing of Environment*, 114: 1494-1503.

Bell, T., Putt, M., Sheldon, T. (2011). Landscape Hazard Assessment in Nain: Phase I: Inventory of Surficial Sediment Types and Infrastructure Damage, Final Report to Nunatsiavut Government and Nain Inuit Community Government.

Berstad, I.M., Sejrup, H.P., Klitgaard-Kristensen, D., Haflidason, H. (2003). Variability in Temperature and Geometry of the Norwegian Current Over the Past 600 Yr; Stable Isotope and Grain Size Evidence from the Norwegian Margin. *Journal of Quaternary Science*, 18(7): 591-602.

Brown, J., Ferrians, O., Heginbottom, J.A., Melnikov, E. (2002). Circum-Arctic Map of Permafrost and Ground-Ice Conditions, Version 2. *NSIDC: National Snow and Ice Data Center*.

Brown, D.R.N., Jorgenson, M.T., Douglas, T.A., Romanovsky, V.E., Kielland, K., Hiemstra, C., Euskirchen, E.S., Ruess, R.W. (2015). Interactive Effects of Wildfire and Climate on Permafrost Degradation in Alaskan Lowland Forests. *Journal of Geophysical Research: Biogeosciences*, 120: 1619-1637.

Burn, C.R. and Smith, C.A.S. (1988). Observations of the Thermal Offset in Near-Surface Mean Annual Ground Temperatures at Several Sites near Mayo, Yukon Territory, Canada. *Arctic*, 41(2): 99-104.

Dyrness, C.T., Viereck, L.A., Van Cleve, K. (1986). Fire in Taiga Communities of Interior Alaska, in K. Van Cleve, F.S. Chapin III, P.W. Flanagan, L.A. Viereck, and C.T. Dyrness (Eds). Forest Ecosystems in the Alaskan Taiga, Ecological Studies 57. Springer Verlag.

Einarsson, M.A. (1984). Climate of Iceland. In Van Loon, H. (Ed)., Climate of the Oceans: World Survey of Climatology. Elsevier Science Publishers.

Flannigan, M.D., Logan, K.A., Amiro, B.D., Skinner, W.R., Stocks, B.J. (2005). Future Area Burned in Canada. *Climatic Change*, 72: 1-16.

Fisher, J.P., Estop-Aragones, C., Thierry, A., Charman, D.J., Wolfe, S.A., Hartley, I.P., Murton, J.B., Williams, M., Phoenix, G.K. (2016). The Influence of Vegetation and Soil Characteristics on Active-Layer Thickness of Permafrost Soils in Boreal Forest. *Global Change Biology*, 22: 3127-3140.

Foster, D.R. (1983). The History and Pattern of Fire in the Boreal Forest of Southeastern Labrador. *Canadian Journal of Botany*, 61(9): 2459-2471.

French, H.M. (2017). The Periglacial Environment, Fourth Edition. John Wiley and Sons.

Fukui, K., Sone, T., Yamagata, K., Otsuki, Y., Sawada, Y., Vetrova, V., Vyatkina, M. (2008). Relationships Between Permafrost Distribution and Surface Organic Layers Near Esso, Central Kamchatka, Russian Far East. *Permafrost and Periglacial Processes*, 19: 85-92.

Gibson, C.M., Chasmer, L.E., Thompson, D.K., Quinton, W.L., Flannigan, M.D., Olefeldt, D. (2018). Wildfire as a Major Driver of Recent Permafrost Thaw in Boreal Peatlands. *Nature Communications*, 9:3041.

Goodrich, L.E. (1978). Efficient Numerical Technique for One-Dimensional Thermal Problems with Phase Change. *International Journal of Heat Mass Transfer*, 21: 615-621.

Guymon, G.L and Luthin, J.N. (1974). A Coupled Heat and Moisture Transport Model for Arctic Soils. *Water Resources Research*, 10(5): 995-1001.

Hansson, K., Simunek, J., Mizoguchi, M., Lundin, L.-C., van Genutchen, M.T. (2004). Water Flow and Heat Transport in Frozen Soil: Numerical Solution and Freeze-Thaw Applications. *Vadose Zone Journal*, 3: 693-704.

Heginbottom, J.A., Dubreuil, M.A., Harker, P.A. (1995). Canada Permafrost, in National Atlas of Canada, 5th edition, Natural Resources Canada.

Holloway, J.E., Lewkowicz, A.G., Douglas, T.A., Li, X., Turetsky, M.R., Baltzer, J.L., Jin, H. (2020). Impact of Wildfire on Permafrost Landscapes: A Review of Recent Advances and Future Prospects. *Permafrost and Periglacial Processes*, DOI: 10.1002/ppp.2048.

Jafarov, E.E., Romanovsky, V.E., Genet, E., McGuire, A.D., Marchenko, S.S. (2013). The Effects of Fire on the Thermal Stability of Permafrost in Lowland and Upland Black Spruce Forests of Interior Alaska in a Changing Climate. *Environmental Research Letters*, 8: 035030.

Jiang, Y., Rocha, A.V., O'Donnell, J.A., Drysdale, J.A., Rastetter, E.B., Shaver, G.R., Zhuang, Q. (2015). Contrasting Soil Thermal Responses to Fire in Alaskan Tundra and Boreal Forest. *Journal of Geophysical Research: Earth Surface*, 120: 363-378.

Jiang, Y., Zhuang, Q., O'Donnell, J.A. (2012). Modeling Thermal Dynamics of Active Layer Soils and Near-Surface Permafrost Using a Fully Coupled Water and Heat Transport Model. *Journal of Geophysical Research*, 117: D11110.

Johnston, G.H. (Ed). (1981). Permafrost: Engineering Design and Construction. John Wiley and Sons.

Jones, V. and Solomina, O. (2015). The Geography of Kamchatka. *Global Planetary Change*, 134: 3-9.

Jorgenson, M.T., Romanovsky, V., Harden, J., Shur, Y., O'Donnell, J., Schuur, E.A.G., Kanevskiy, M., Marchenko, S. (2010). Resilience and Vulnerability of Permafrost to Climate Change. *Canadian Journal of Forest Research*, 40: 1219-1236.

Lawrence, D.M. and Swenson, S.C. (2011). Permafrost Response to Increasing Arctic Shrub Abundance Depends on the Relative Influence of Shrubs on Local Soil Cooling versus Large-Scale Climate Warming. *Environmental Research Letters*, 6: 045504.

Lémus-Lauzon, I., Bhiry, N., Arsenault, D., Woollett, J., Delwaide, A. (2018). Tree-Ring Evidence of Changes in the Subarctic Forest Cover Linked to Human Disturbance in Northern Labrador (Canada). *Ecoscience*, 25(2): 135-151.

Luthin, J.N. and Guymon, G.L. (1974). Soil Moisture-Vegetation-Temperature Relationships in Central Alaska. *Journal of Hydrology*, 23: 233-246.

Marchenko, S., Romanovsky, V., Tipenko, G. (2008). Numerical Modeling of Spatial Permafrost Dynamics in Alaska. In Proceedings of the Ninth International Conference on Permafrost, in Fairbanks, United States.

Miranda, B.R., Sturtevant, B.R., Schmelzer, I., Doyon, F., Wolter, P. (2016). Vegetation Recovery Following Fire and Harvest Disturbance in Central Labrador – A Landscape Perspective. *Canadian Journal of Forest Research*, 46: 1009-1018.

Muller, E.H. (1955). Bristol Bay Region, in D.M. Hopkins, T.N.V. Karlstrom, R.F. Black, J.R. Williams, T.L. Péwé, A.T. Fernald, E.H. Muller. Permafrost and Ground Water in Alaska. United States Government Printing Office.

Nash, C.H. and Johnson, E.A. (1996). Synoptic Climatology of Lightning-Caused Forest Fires in Subalpine and Boreal Forests. *Canadian Journal of Forest Reseaarch*, 26: 1859-1874.

Nossov, D.R., Jorgenson, M.T., Kielland, K., Kanevskiy, M.Z. (2013). Edaphic and Microclimatic Controls Over Permafrost Response to Fire in Interior Alaska. *Environmental Research Letters*, 8: 035013.

Pastick, N.J., Jorgenson, M.T., Wylie, B.K., Nield, S.J., Johnson, K.D., Finley, A.O. (2015). Distribution of Near-Surface Permafrost in Alaska: Estimates of Present and Future Conditions. *Remote Sensing of Environment*, 168: 301-315.

Payette, S., Delwaide, A., Caccianiga, M., Beauchemin, M. (2004). Accelerated Thawing of Subarctic Peatland Permafrost Over the Last 50 Years. *Geophysical Research Letters*, 31: L18208.

Roberts, B.A., Simon, N.P.P., Deering, K.W. (2006). The Forests and Woodlands of Labrador, Canada: Ecology, Distribution and Future Management. *Ecological Research*, 21: 868-880.

Shur, Y.L. and Jorgenson, M.T. (2007). Patterns of Permafrost Formation and Degradation in Relation to Climate and Ecosystems. *Permafrost and Periglacial Processes*, 18: 7-19.

Smith, M.W. and Riseborough, D.W. (2002). Climate and the Limits of Permafrost. *Permafrost and Periglacial Processes*, 13: 1-15.

Sone, T., Yamagata, K., Otsuki, Y., Sawada, Y., Vyatkina, M. (2006). Distribution of Permafrost on the West Slope of Mt. Itchinsky, Kamchatka, Russia. *Bulletin of Glaciological Research*, 23: 69-75.

Sturm, M., Schimel, J., Michaelson, G., Welker, J.M., Oberbauer, S.F., Liston, G.E., Fahnestock, J., Romanovsky, V. (2005). Winter Biological Processes Could Help Convert Arctic Tundra to Shrubland. *Bioscience*, 55: 17-26.

Treat, C.C., Wisser, D., Marchenko, S., Frolking, S. (2013). Modelling the Effects of Climate Change and Disturbance on Permafrost Stability in Northern Organic Soils. *Mires and Peat*, 12: 1-17.

Way, R.G. and Viau, A.E. (2015). Natural and Forced Air Temperature Variability in the Labrador Region of Canada During the Past Century. *Theoretical and Applied Climatology*, 121(5): 413-424.

Way, R.G., Lewkowicz, A.G., Zhang, Y. (2018). Characteristics and Fate of Isolated Permafrost Patches in Coastal Labrador, Canada. *The Cryosphere*, 12: 2667-2688.

Way, R.G., Lewkowicz, A.G., Wang, Y. (2020). Analysis of Permafrost Conditions at Nain, Nunatsiavut, Labrador. *Manuscript in preparation*.

Williams, P.J. and Smith, M.W. (1989). The Frozen Earth, Fundamentals of Geocryology. Cambridge University Press.

Wotton, B.M., Nock, C.A., Flannigan, M.D. (2010). Forest Fire Occurrence and Climate Change in Canada. *International Journal of Wildland Fire*, 19: 253-271.

Zhang, Y., Chen, W., Cihlar, J. (2003). A Process-Based Model for Quantifying the Impact of Climate Change on Permafrost Thermal Regimes. *Journal of Geophysical Research*, 108(D22): 4695.

Zhang, Y., Wolfe, S.A., Morse, P.D., Olthof, I., Fraser, R.H. (2015). Spatiotemporal Impacts of Wildfire and Climate Warming on Permafrost Across a Subarctic Region, Canada. *Journal of Geophysical Research: Earth Surface*, 120: 2338-2356.

Zoltai, S.C. (1972). Palsas and Peat Plateaus in Central Manitoba and Saskatchewan. *Canadian Journal of Forest Research*, 2: 291-302.

CHAPTER 2 : STUDY AREA AND SITE SELECTION

Labrador, located in northeastern Canada, is the continental portion of the Canadian province of Newfoundland and Labrador. Field investigations and modelling efforts for this project are concentrated at three sites within Nunatsiavut, an Inuit land claim zone covering approximately 15,800 km^2 of land in northern coastal Labrador (Roberts et al., 2006). The following sections comprise an overview of the climate, glacial history, permafrost distribution, and forest composition of Nunatsiavut and the greater coastal Labrador region.

2.1 Climate

Labrador's climate is strongly influenced by the Labrador Current that carries cold Arctic waters down the Atlantic coast of Canada (Foster 1983; Banfield and Jacobs, 1998; Roberts et al., 2006). Throughout Nunatsiavut and much of Labrador, winters tend to be long and cold, and summers tend to be short and cool (Hare, 1950; Banfield and Jacobs, 1998). The proximity of the region to the Atlantic Ocean makes the air temperatures particularly sensitive and responsive to changes in ocean surface temperatures and climatic oscillations, such as the Arctic Oscillation, the Atlantic Multidecadal Oscillation, and the El Niño Southern Oscillation (Way and Viau, 2015). Since the end of the 19^{th} century, the Labrador region has experienced an overall increase in air temperature of approximately 1.5°C (Way and Viau, 2015). However, this warming trend has not been evenly distributed among the four major seasons, nor has it been linear through time. From 1880 to 2010, the greatest warming trend (+2.03°C) was during the winter, and the smallest warming trend was during the spring (+0.96°C) (Way and Viau, 2015). The prominent winter warming signal has been linked to changes in snow depth, snow distribution, and sea ice formation and break-up (Way and Viau, 2015). Warming in Labrador was gradual from the 1880s to the 1960s, but cooling then took place through to the mid-1990s. A notable increase in air temperature from the mid-1990s to present is attributed to a combination of both natural and anthropogenic influences (Way and Viau, 2015).

Labrador is characterized by some of the highest precipitation levels in the North American boreal zone (Hare, 1950; Banfield and Jacobs, 1998). The largest snowfalls in northeastern Canada are in Nunatsiavut, due to the high moisture availability and relief of the region and the high frequency of winter storm systems passing directly through the area (Brown and Lemay, 2012). Much of the current knowledge on precipitation trends for the Labrador and northern Quebec region is informed by a combination of traditional knowledge, remote sensing, and spatial modelling (Brown and Lemay, 2012). Precipitation in Nunatsiavut increased by approximately 13% from 1950 to 2001 (Brown and Lemay, 2012). In contrast, satellite imagery shows that the annual snow cover duration of approximately 200 days has decreased by up to 1 month over the last half-century (Brown and Lemay, 2012). These changes suggest that rainfall is being favoured over snowfall, which has implications for local travel, access to traditional foods and fuelwood, and local ecosystem and vegetation dynamics.

2.2 Physical Landscape

Labrador is composed of segments of the Grenville, Makkovic, Nain, Churchill, and Superior structural provinces of the Canadian Shield (Roberts et al., 2006). The landscape is largely characterized by igneous and metamorphic bedrock terrain (Figure 2-1), covered by a thin layer of soil that originates from the last glaciation (Roberts et al., 2006; Bell et al., 2011).

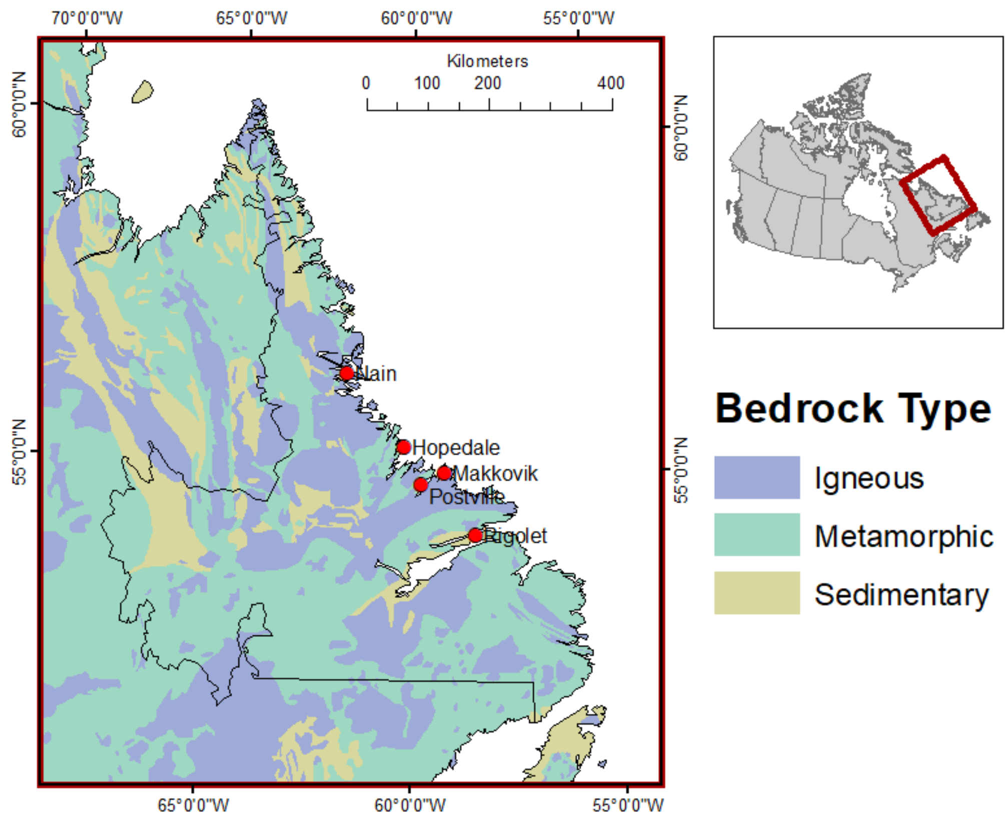

Figure 2-1. Distribution of Bedrock Types Across Labrador (Gowan et al., 2018). Nunatsiavut communities are identified and labelled.

During the last glacial maximum, much of Labrador and its surrounding regions were covered by the Laurentide Ice Sheet (LIS) (Dyke, 2004; Bell et al., 2011). The LIS, after reaching its maximum extent and thickness during the Late Wisconsinan, experienced sequential westward retreat across Labrador, from approximately 12 to 6 k years BP (Figure 2-2), with the locations of the coastal communities of Nunatsiavut undergoing deglaciation approximately 9 to 8 k years BP (Foster, 1983; Bell et al., 2011). During and following the retreat of the LIS, layers of frost-susceptible, fine-grained sediments were deposited throughout the valley bottoms and lowlands of coastal Labrador, located between steep bedrock ridges that were shaped by the flow of the LIS (Bell et al., 2011). Some Nunatsiavut communities are now constructed on these glaciofluvial and glaciomarine sediments (Bell et al., 2011). From south to north along the coast of Labrador, the marine limit decreases in elevation (Fulton, 1989). Near Nain, the marine limit is approximately 40 m a.s.l. (Johnson, 1969), but marine deposits were only found in the first 10 or 20 m a.s.l. during a local landscape hazard assessment (Bell et al., 2011). The salinity of these sediments is unknown but is probably low, due to the low salinity of the adjacent Labrador Sea and high amounts of precipitation that would have leached out salts after emergence.

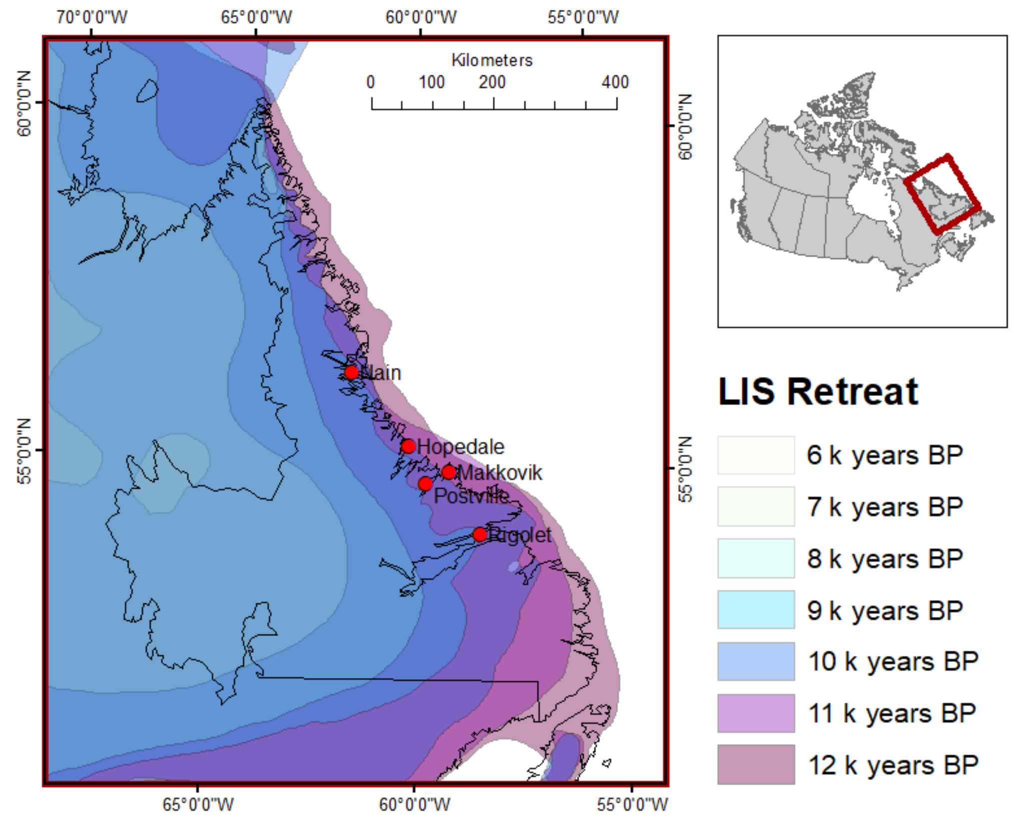

Figure 2-2. Approximate Extent of Laurentide Ice Sheet (LIS) During Retreat Across Labrador from 12 to 6 k years BP (Natural Resources Canada, 2016). Nunatsiavut communities are identified and labelled.

2.3 Permafrost Distribution

The presence of permafrost throughout coastal Labrador is associated with the unique climate of the region, which is greatly influenced by the cold Labrador current. The coastal Labrador region is also characterized by an extremely low geothermal heat flux, which facilitates the development and persistence of warm and thick bodies of permafrost (Mareschal et al., 2010).

According to the Permafrost Map of Canada (Heginbottom et al., 1995), permafrost distribution within Nunatsiavut ranges from zones of continuous permafrost in the Torngat Mountains National Park to isolated patches of permafrost, within which the community of Rigolet is located (Figure 2-3-A). The other four Nunatsiavut communities are located in the sporadic discontinuous permafrost zone (Heginbottom et al., 1995).

However, the distribution of permafrost in the Labrador region can be complicated by variations in physiography, topography, and vegetation. Way and Lewkowicz (2016) address these local complexities by incorporating snow depths in relation to land cover in their recent modelling efforts (Figure 2-3-B). Their results indicate less continuous permafrost compared to previous classifications (e.g., Heginbottom et al., 1995). Nain and Hopedale remain classified within the sporadic discontinuous permafrost zone, while Makkovik and Postville are re-classified within the isolated patches zone.

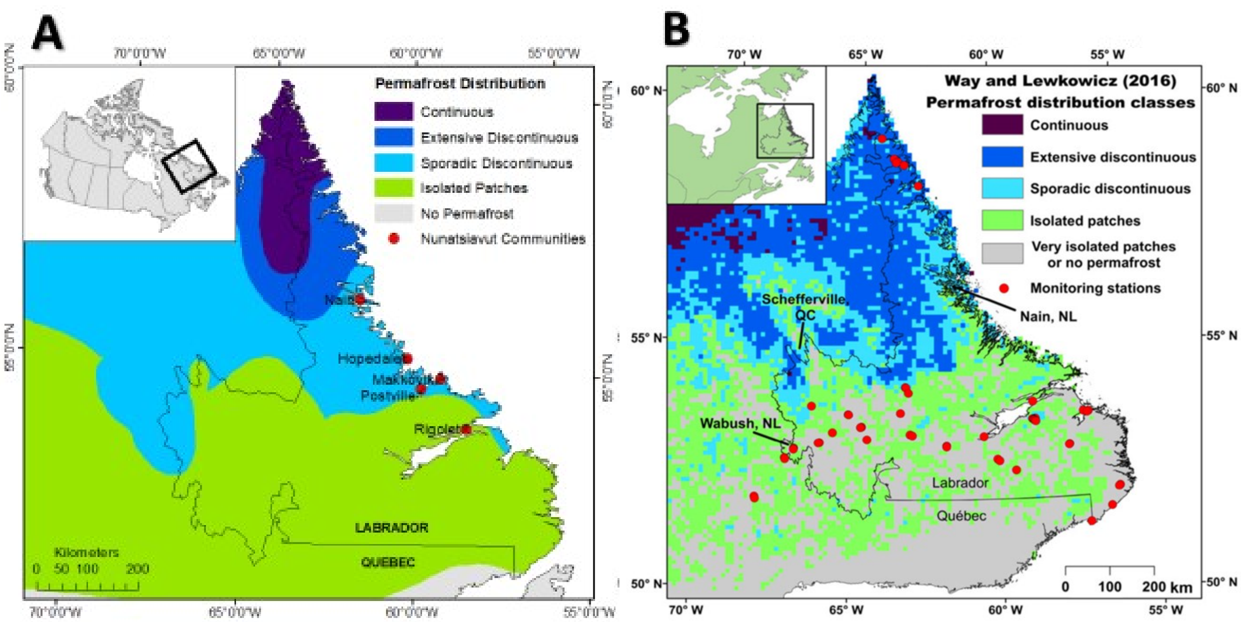

Figure 2-3. (A) Permafrost Distribution in Labrador According the 1995 Permafrost Map of Canada (Heginbottom et al., 1995; Brown et al., 2002). (B) Permafrost Distribution in Labrador According to Way and Lewkowicz (2016) (from Way and Lewkowicz, 2018).

2.4 Vegetation and Forest Fire

Vegetation establishment in Nunatsiavut and coastal Labrador occurred following the retreat of the LIS (Lamb, 1980; Payette, 2007; Lévesque et al., 2012). Ten ecoregions are present (Figure 2-4), ranging from alpine and high subarctic tundra in the north, through coastal barrens and mid-subarctic forest, to low subarctic forest and high boreal forest in the south (Roberts et al., 2006).

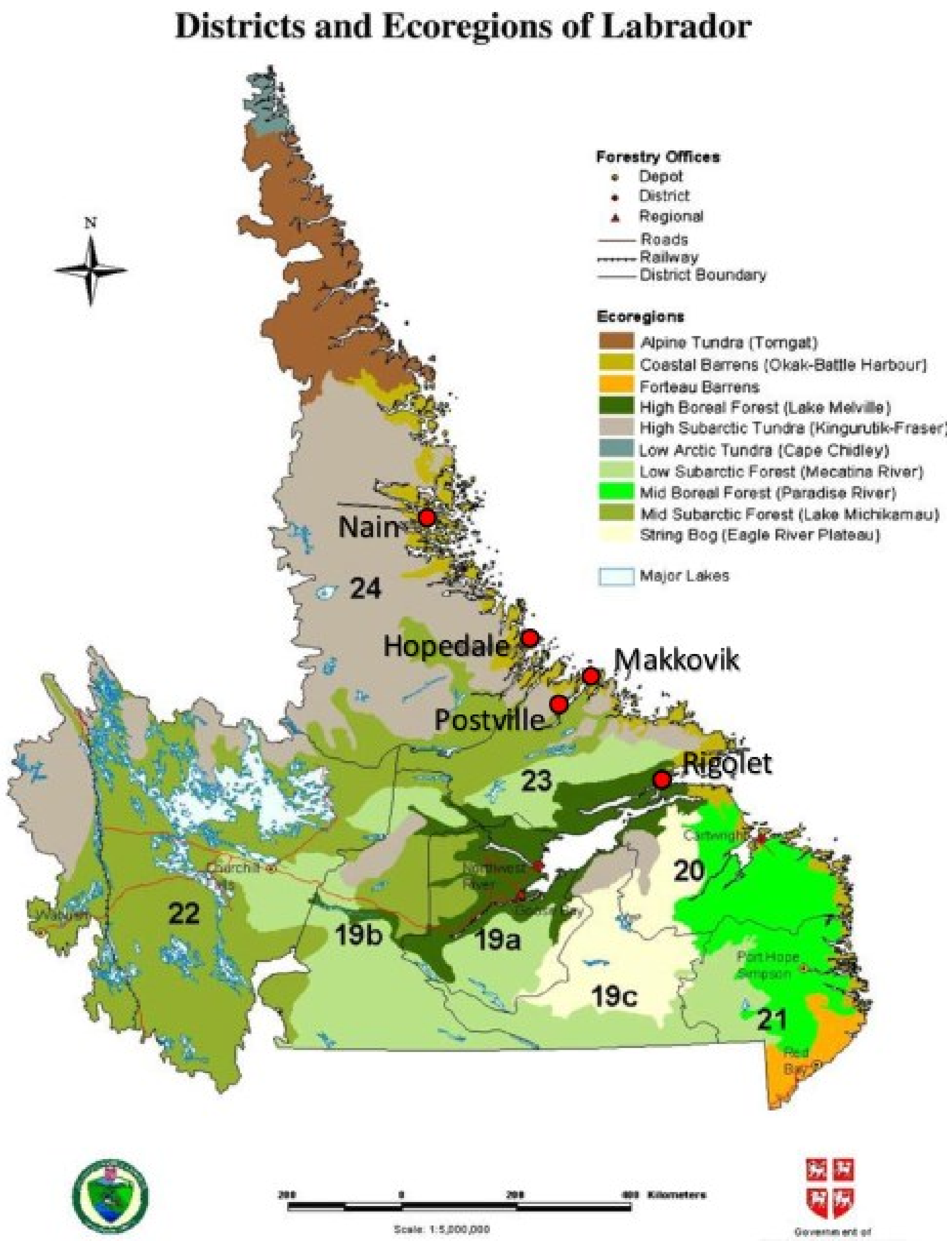

Figure 2-4. Spatial Distribution of Districts and Ecoregions of Labrador (from Roberts et al., 2006).

The boreal forests of Labrador are primarily composed of black spruce (*Picea mariana* [Mill.] B.S.P.), but white spruce (*Picea glauca* [Moench] Voss), balsam fir (*Abies balsamea* [L.] Mill.), and eastern larch (*Larix laricina* [Du Roi] K. Koch) are also common. For example, white spruce has recently expanded northwards into suitable and otherwise unoccupied sites in southern coastal Nunatsiavut (Payette, 2007; Lévesque et al., 2012), and it is predicted that continued climate warming will result in forests and latitudinal treelines throughout Labrador being dominated by eastern larch (Trant and Hermanutz, 2014). However, tree establishment is complicated by the steep and irregular topography of coastal Labrador, which may serve as a physical barrier (Payette, 2007). Despite this, recent afforestation has been observed in and around the northernmost community of Nain (Lémus-Lauzon et al., 2018) and is attributed to a combination of climate warming and land use activities, including tree harvesting (Lémus-Lauzon et al., 2012).

Eastern boreal stands have longer fire intervals than western boreal stands in North America, so they are typically older and more structurally complex, with dynamic canopy dominance and trees of varying ages (Foster, 1983; Kneeshaw and Gauthier, 2003). While the majority of Canadian boreal forest fires are ignited through lightning activity (Nash and Johnson, 1996), eastern Canada is characterized by a wetter climate, with fewer and less intense lightning storms than in the western and central North American boreal forest (Coops et al., 2018). This results in estimated fire intervals of 500 to 5000 years in Labrador's boreal forest, which are much longer than the 50 to 200 years reported for the West (Foster, 1983; Coops et al., 2018).

2.5 Study Sites

This thesis investigates frozen ground conditions at three forest fire sites in Nunatsiavut. These sites were selected based on their proximity to and accessibility by boat in the summer and by snowmobile in the winter from communities within Nunatsiavut. This narrowed the list of possible forest fire sites to four: the Tikkoatokak Bay (TB) burn of 2001 near Nain, the Webb Bay (WB) burn of 2004 near Nain, the Beaver River (BR) burn of 1996 near Postville, and the Guloo Point Burn of 1967 near Postville.

The Guloo Point Burn of 1967 was omitted from this study for two reasons. First, the fire was considered to have occurred too long ago to fit within the scope of this study. Fire-disturbed forests in southern Labrador typically require an average of 44 years to reach their recovery threshold, corresponding to 80% of the pre-fire conditions (Miranda et al. 2016). Based on these findings, the vegetation at the Guloo Point Burn could have reached its recovery threshold approximately a decade before the current study began. Second, this thesis is part of a larger multi-disciplinary, multi-institutional project, led by Dr. Carissa Brown (Memorial University). The final selection of the study sites was performed in consultation with other project members. A component of the project, led by Frédéric Dwyer-Samuel (Université de Montréal), investigates the practice of "wooding", in which residents harvest wood from surrounding forests for fuel. Burned forests are preferred because the wood has already been dried and cured by the fire (Lémus-Lauzon et al., 2012; Oberndorfer, 2020). In Postville, the wood at the Guloo Point Burn is generally considered to be too old to be used as good fuel wood, and residents prefer to go wooding in the more recent BR location. For these reasons, the Guloo Point Burn was not examined.

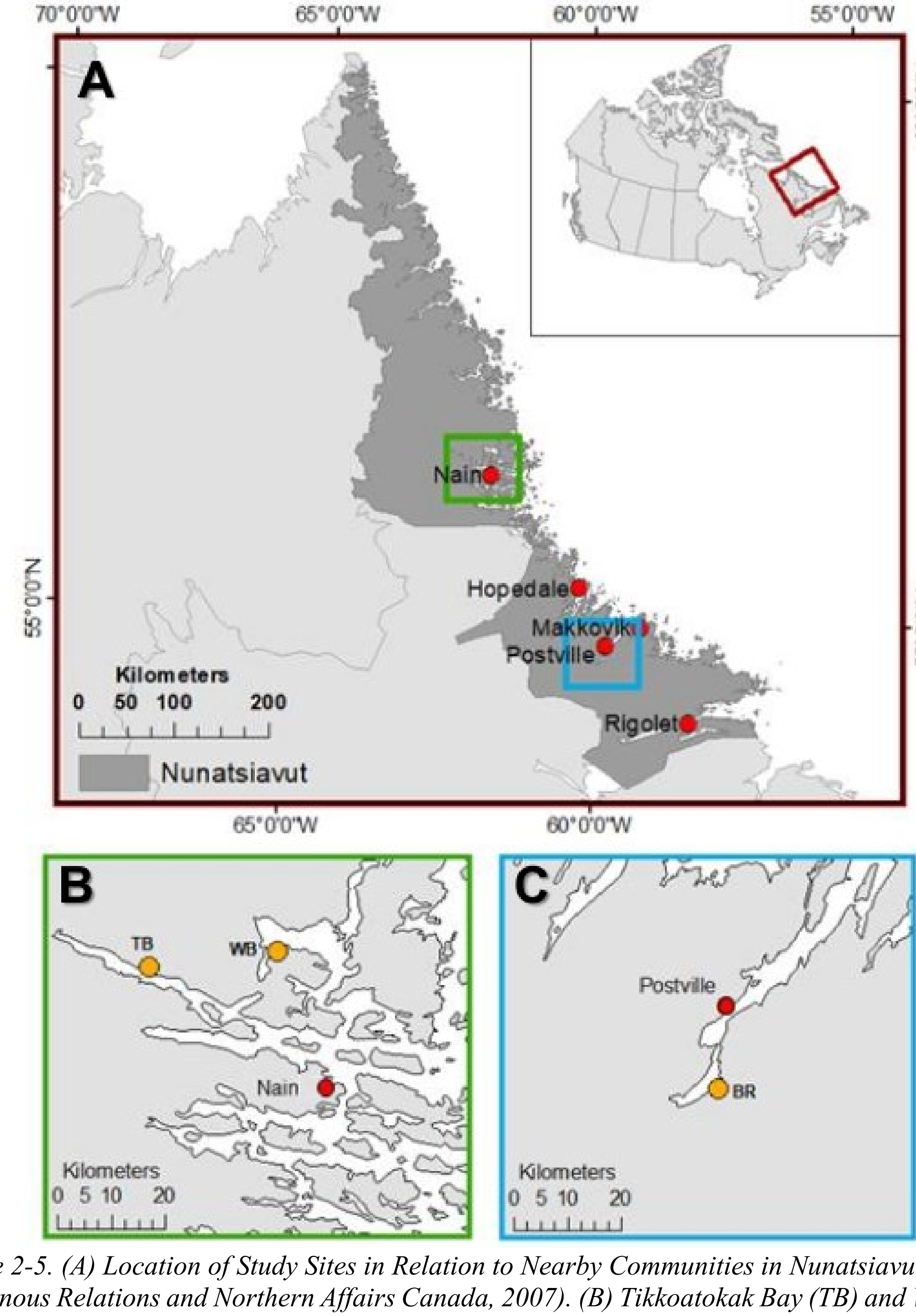

Figure 2-5. (A) Location of Study Sites in Relation to Nearby Communities in Nunatsiavut (Crown-Indigenous Relations and Northern Affairs Canada, 2007). (B) Tikkoatokak Bay (TB) and Webb Bay (WB) fire sites near Nain; (C) Beaver River (BR) fire site near Postville.

The TB burn, commonly referred to by Nain residents as "the burnt woods", is located approximately 30 km northwest of the community (Figure 2-5-B). It occurred in summer 2001 on a south-facing slope and covered approximately 3 km^2. The site is composed of a series of raised beaches, and exposed bedrock is observed in adjacent areas (Figure 2-6).

Figure 2-6. Photographs of the TB Site. The burn occurred in 2001. The vegetation cover in the burned area is shrub-dominated.

The WB burn, commonly called the "sandy point burn" by the residents of Nain, is located approximately 25 km north of the community (Figure 2-5-B). It occurred in summer 2004 on a north-facing slope and has an area of only 1 km^2. The site is located on a series of raised beaches, but erratics are also present (Figure 2-7).

Figure 2-7. Photographs of the WB Site. The burn occurred in 2004. The vegetation cover in the burned area is shrub-dominated.

The BR burn, referred to by Postville residents as “the burn up the bay”, is located 15-20 km southwest of the community, on the southern shore of the innermost segment of Kaipokok Bay (Figure 2-5-C). The fire occurred in summer 1996 and was much larger than the two near Nain, stretching across approximately 150 km^2 of black spruce-dominated forest (Figure 2-8). The BR fire is located near the mapped boundary between the sporadic discontinuous permafrost zone and the zone of isolated patches of permafrost (Heginbottom et al., 1995). The site is underlain by a combination of alluvial material and wave-washed till and has numerous large erratics.

Figure 2-8. Photographs of the BR Site. The burn occurred in 1996. The vegetation cover of the burned area is dominated by shrubs.

Key characteristics of the three study sites (Figure 2-5) are summarized in Table 2-1.

Table 2-1. Summary of Key Characteristics for the Tikkoatokak Bay (TB), Webb Bay (WB), and Beaver River (BR) Study Sites.

Variable	Tikkoatokak Bay (TB)		Webb Bay (WB)		Beaver River (BR)
Year of Burn	2001		2004		1996
Approximate Size of Burn (km^2)	3		1		150
Nearest Community	Nain		Nain		Postville
Latitude (°N)	56.755		56.706		54.781
Longitude (°W)	61.869		62.209		59.808
Elevation (m a.s.l.)	18		16		11
Aspect	South-facing		North-facing		North-facing
Slope (°)	7		6		1 (Mostly Flat)
Mean Annual Air Temperature (°C)	-2.4[a]	-3.0[b]	-1.9[b]	-2.5[a]	-3.2[b]
Thawing Degree Days	1221[a]	1132[b]	1429[b]	1166[a]	1083[b]
Freezing Degree Days	2112[a]	2214[b]	2131[b]	2083[a]	2265[b]
Snow-on-Ground Season Length (days)	227[a]	213[b]	219[b]	239[a]	236[b]
Forest Species Composition	Mixed black spruce, white spruce, tamarack, balsam fir		Mixed black spruce, white spruce, tamarack, balsam fir		Primarily black spruce, some balsam fir
Ecoregion[c]	Coastal Barrens		Coastal Barrens		Mid-Subarctic Forest
Ecozone[d]	Boreal Shield East		Boreal Shield East		Boreal Shield East
Fire Regime Zone[d]	Eastern Subarctic Zone		Eastern Subarctic Zone		North Atlantic Zone
Estimated Fire Return Interval (years)[d]	1,501-5,000		1,501-5,000		501-1,500
Permafrost Zone[e]	Sporadic Discontinuous		Sporadic Discontinuous		Sporadic Discontinuous
Permafrost Zone[f]	Sporadic Discontinuous		Sporadic Discontinuous		Isolated Patches

[a] measured over one full calendar year from 2017 to 2018.
[b] measured over one full calendar year from 2018 to 2019.
[c] from Roberts et al. (2006).
[d] from Coops et al. (2018).
[e] from Heginbottom et al. (1995).
[f] from Way and Lewkowicz (2016).

2.6 References

Banfield, C.E. and Jacobs, J.D. (1998). Regional Patterns of Temperature and Precipitation for Newfoundland and Labrador During the Past Century. *The Canadian Geographer/Le Géographe canadien*, 42(4): 354-364.

Bell, T., Putt, M., Sheldon, T. (2011). Landscape Hazard Assessment in Nain: Phase I: Inventory of Surficial Sediment Types and Infrastructure Damage, Final Report to Nunatsiavut Government and Nain Inuit Community Government.

Brown, J., Ferrians, O., Heginbottom, J.A., Melnikov, E. (2002). Circum-Arctic Map of Permafrost and Ground-Ice Conditions, Version 2. *NSIDC: National Snow and Ice Data Center*.

Brown, R. and Lemay, M. (2012). Climate Variability and Change in the Canadian Eastern Subarctic IRIS Region (Nunavik and Nunatsiavut). In Nunavik and Nunatsiavut: From Science to Policy. An Integrated Reginal Impact Study (IRIS) of Climate Change and Modernization. ArcticNet Inc.

Coops, N.C., Hermosilla, T., Wulder, M.A., White, J.C., Bolton, D.K. (2018). A Thirty Year, Fine-Scale, Characterization of Area Burned in Canadian Forests Shows Evidence of Regionally Increasing Trends in the Last Decade. *PLoS ONE*, 13(5): e0197218.

Dyke, A.S. (2004). An Outline of North American Deglaciation with Emphasis on Central and Northern Canada. *Developments in Quaternary Sciences*, 2: 373:424.

Foster, D.R. (1983). The History and Pattern of Fire in the Boreal Forest of Southeastern Labrador. *Canadian Journal of Botany*, 61(9): 2459-2471.

Fulton, J.R. (1989). Quaternary Geology of Canada and Greenland. DOI: 10.4095/127905.

Gowan, E.J., Niu, L., Knorr, G., Lohmann, G. (2018). Geology Datasets in North America, Greenland and Surrounding Areas for Use with Ice Sheet Models. *Pangaea*. Retrieved from https://doi.pangaea.de/10.1594/PANGAEA.895889.

Kneeshaw, D. and Gauthier, S. (2003). Old Growth in the Boreal Forest: A Dynamic Perspective at the Stand and Landscape Level. *Environmental Reviews*, 11: S99-S114.

Hare, F.K. (1950). Climate and Zonal Divisions of the Boreal Forest Formation in Eastern Canada. *The Geographical Review*, 40(4): 615-635.

Heginbottom, J.A., Dubreuil, M.A., Harker, P.A. (1995). Canada Permafrost, in National Atlas of Canada, 5th edition, Natural Resources Canada.

Johnson, J.P. (1969). Deglaciation of the Central Nain-Okak Bay Section of Labrador. *Arctic*, 22(4): 373-394.

Lamb, H.F. (1980). Late Quaternary Vegetational History of Southeastern Labrador. *Arctic and Alpine Research*, 12(2): 117-135.

Lémus-Lauzon, I., Bhiry, N., Arsenault, D., Woollett, J., Delwaide, A. (2018). Tree-Ring Evidence of Changes in the Subarctic Forest Cover Linked to Human Disturbance in Northern Labrador (Canada). *Ecoscience*, 25(2): 135-151.

Lémus-Lauzon, I., Bhiry, N., Woollett, J. (2012). Napâttuit: Wood Use by Labrador Inuit and its Impact on the Forest Landscape. Inuit Studies, 36: 113-137.

Lévesque, E., Hermanutz, L., Gérin-Lajoie, J. (2012). Trends in Vegetation Dynamics and Impacts on Berry Productivity. In Nunavik and Nunatsiavut: From Science to Policy. An Integrated Reginal Impact Study (IRIS) of Climate Change and Modernization. ArcticNet Inc.

Mareschal, J.C., Poirier, A., Rolandone, F., Bienfait, G., Gariepy, C., Lapointe, R., Jaupart, C. (2000). Low Mantle Heat Flow at the Edge of the North American Continent, Voisey Bay, Labrador. *Geophysical Research Letters*, 27(6): 823-826.

Miranda, B.R., Sturtevant, B.R., Schmelzer, I., Doyon, F., Wolter, P. (2016). Vegetation Recovery Following Fire and Harvest Disturbance in Central Labrador – A Landscape Perspective. *Canadian Journal of Forest Research*, 46: 1009-1018.

Nash, C.H. and Johnson, E.A. (1996). Synoptic Climatology of Lightning-Caused Forest Fires in Subalpine and Boreal Forests. *Canadian Journal of Forest Research*, 26: 1859-1874.

Natural Resources Canada (2016). Paleo-Environmental Records of Climate Change Across Canada – Vegetation History, Glaciated North America. Retrieved from: https://open.canada.ca/data/en/dataset/a384bada-a787-5b49-9799-f5d589e97bd3.

Oberndorfer, E. (2020). What the Blazes!? A People's History of Fire in Labrador. *Journal of the North Atlantic*, 40: 1-16.

Payette, S. (2007). Contrasted Dynamics of Northern Labrador Tree Lines Caused by Climate Change and Migrational Lag. *Ecology*, 88: 770-780.

Roberts, B.A., Simon, N.P.P., Deering, K.W. (2006). The Forests and Woodlands of Labrador, Canada: Ecology, Distribution and Future Management. *Ecological Research*, 21: 868-880.

Trant, A.J. and Hermanutz, L. (2014). Advancing Towards Novel Tree Lines? A Multispecies Approach to Recent Tree Line Dynamics in Subarctic Alpine Labrador, Northern Canada. *Journal of Biogeography*, 41: 1115-1125.

Way, R.G. and Lewkowicz, A.G. (2016). Modelling the Spatial Distribution of Permafrost in Labrador-Ungava Using the Temperature at the Top of Permafrost. *Canadian Journal of Earth Sciences*, 53: 1010-1028.

Way, R.G. and Viau, A.E. (2015). Natural and Forced Air Temperature Variability in the Labrador Region of Canada During the Past Century. *Theoretical and Applied Climatology*, 121(5): 413-424.

CHAPTER 3 : METHODOLOGY

3.1 Field Investigations

Field observations were made in the summers of 2017, 2018, and 2019 and in winters 2018 and 2019 (Table 3-1). Permafrost-related fieldwork is typically performed in late-summer to prevent misinterpretation of seasonally frozen ground as perennially frozen ground. Due to logistic and operational challenges, including equipment availability, conflicting researcher schedules, and boat-based site access, summer field observations for this study are collected from mid-July to mid-August. Winter field observations were made at the sites near Nain in March 2018, and at the site near Postville in February 2019.

Two 80 m-long transects were established at each of the TB and WB sites, and two 40 m-long transects and one 50 m-long transect were established at the BR site. The timing of field measurement collection along each of these transects is summarized in Table 3-1.

Table 3-1. Timing of Field Data Collection (YY-MM-DD) Along Transects at TB, WB, and BR Sites.

Measurement	TB1	TB2	WB1	WB2	BR1	BR2	BR3
Transect Length (m)	80	80	80	80	40	40	50
Snow Depth	18-03-23	18-03-23	18-03-24	18-03-24	19-02-18	19-02-18	19-02-19
Electrical Resistivity Tomography	18-07-23	18-07-27	17-07-19	18-07-25	18-07-18	18-07-18	N/A
Frost Probing and Instantaneous Temperature	19-08-15	19-07-28	19-07-27	19-07-26	19-07-19	19-07-19	19-07-20
Organic Layer Thickness	18-07-23	18-07-27	18-07-31	18-07-25	18-07-18	18-07-18	19-07-20
Soil Temperature and Moisture	18-07-23	18-08-16	18-07-22	18-07-25	18-07-18	18-07-20	N/A
Canopy Cover Image Collection	19-08-15	19-08-15	19-07-26	19-07-26	19-07-19	19-07-19	19-07-20
Shrub Height and Density	18-08-03	18-08-03	18-07-22	18-07-28	18-08-18	18-07-20	19-07-20

3.1.1 Climate

Weather stations were established in the unburned forest at each of the sites (Figure 3-1-A). The stations were equipped with Hobo Pro v2 Temperature/Relative Humidity U23-001 Data Loggers (Onset), positioned within a solar radiation shield, recording air temperature (±0.21°C accuracy) and relative humidity (±2.5% accuracy) every 2 hours. The stations were also equipped with snow stakes, comprised of a series of vertically arranged Thermochron DS1921G-F5 iButtons (Maxim) for determining snow accumulation and melt patterns during the winter season. Snow stakes were also placed in the burned region at each site (Figure 3-1-B), to permit intra-site comparisons of snow dynamics. The iButtons were placed at heights of 0 cm, 10 cm, 20 cm, 30 cm, 40 cm, 50 cm, 60 cm, 80 cm, 100 cm, 120 cm, 140 cm, and 160 cm above the ground surface and recorded temperature at 4-hour intervals with a resolution of 0.5°C and an accuracy of ±1°C (see Lewkowicz, 2008). Patterns of snow accumulation in the autumn and early winter were manually identified by differences in the amplitude of daily temperature cycles at each measurement level. This interpretation of the vertically arranged data is dependent on the smaller diurnal temperature range that is expected for sensors located beneath the snow compared to those still exposed above the snow surface (Isaksen et al., 2002; Danby and Hik, 2007; Lewkowicz, 2008).

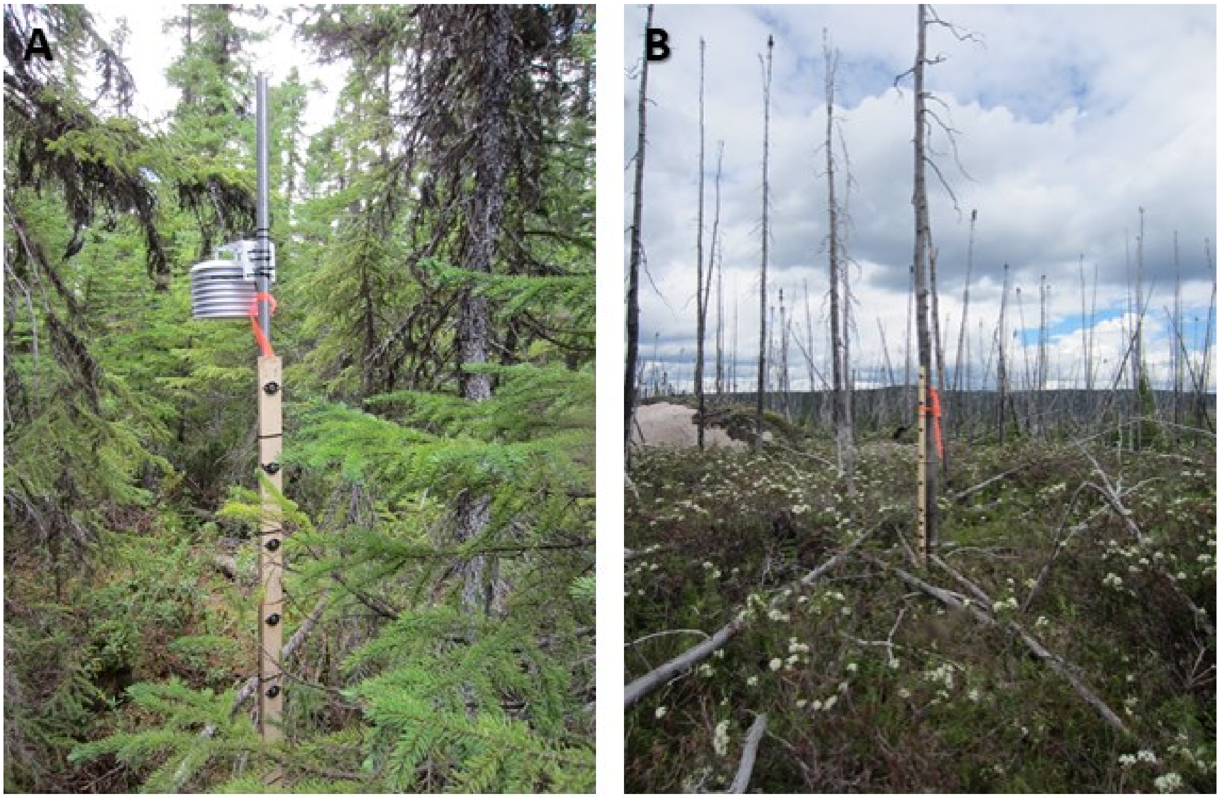

Figure 3-1. (A) Weather Station Located in Unburned Forest at the BR Site. (B) Snow Stake Located in Burned Region at the BR Site.

3.1.2 Geophysical Surveys and their Validation

The presence or absence of frozen ground at the study sites was assessed using electrical resistivity tomography (ERT). Direct current ERT is a geophysical technique that can be used to delimit frozen and unfrozen ground based on electrical contrasts between the two states (Fortier et al., 2008; Kneisel et al., 2008). Cryotic earth materials usually have higher resistivities than non-cryotic earth materials, due to their lower unfrozen moisture contents.

ERT has been applied throughout the Canadian Arctic and subarctic to investigate the presence and thickness of bodies of frozen ground. In western Canada, ERT has been used throughout the Yukon (Lewkowicz et al., 2011) and the Northwest Territories (McClymont et al., 2013). In eastern Canada, ERT has been successfully applied in Nunavik (Fortier et al., 2008) and in both southern (Way et al., 2018) and northern coastal Labrador (Lewkowicz and Way, 2014; Way and Lewkowicz, 2015).

One-dimensional ERT requires a minimum of four electrodes, where an electrical current is run through one pair of electrodes, and the potential difference is measured across the other pair. A two-dimensional profile of ground resistivity can be generated by repeating this process through different sets of electrodes set out in a multi-electrode array (Hilbich et al., 2008). The Wenner electrode configuration was used in the current study, due to its stability in heterogeneous regions and its ability to delineate horizontal structures, such as the top and the base of permafrost (Hauck et al., 2004; Fortier et al., 2008). The electrodes were connected by jumper cables to take-outs, which were connected to an ABEM Terrameter LS profiling system.

In this study, ERT lines, measuring 40 or 80 m in length, were centred along and positioned perpendicular to fire breaks. The electrodes for the 80 m-long surveys at the TB and WB sites were initially placed at 2 m intervals from 0 m to 20 m and 60 m to 80 m and at 1 m intervals from 20 to 60 m. Infilling of the outer sections was performed to a resolution of 1 m, whenever logistically possible. The 80 m-long surveys permitted a depth of investigation of approximately 12 m. For the 40 m-long surveys at the BR site, a total of 41 electrodes were placed at 1 m intervals, permitting a depth of investigation of approximately 6 m.

In the field, the profiling system records apparent resistivities, which are indirect measurements of the subsurface distribution of ground resistivity. These were processed and converted to best-estimate values using RES2DINV inversion software (Loke et al., 2003), which applies a Gauss-Newton algorithm to fit an appropriate subsurface model to the observations (Kneisel et al., 2008; Hilbich et al., 2009). The robust inversion scheme was selected in RES2DINV to minimize smoothing of contrasts in resistivity measurements, especially along the boundaries of bodies of frozen ground (Hilbich et al., 2008). Inversion iterations were permitted until convergence had occurred, marked by a change in the root mean square error between consecutive iterations of less than 5%, or until the fifth iteration, whichever came first. Topography and breaks in slope along the ERT lines were recorded with a clinometer, and topographic corrections were applied to all ERT profiles during the inversion process.

Electrical resistivity can be influenced by various properties, such as particle size, moisture content, pore water salinity, and temperature. The boundary value between frozen and unfrozen material can therefore vary between sites and regions (Fortier et al., 2008), and interpretation of the tomograms often requires additional validation. Our ERT survey results were validated with frost table depths and instantaneous temperature measurements.

The frost table depth was measured at 1 m intervals along the ERT transects by inserting a 120 cm-long probe into the ground to the depth of refusal or to the end of the probe. Interpretation of the nature of the refusal, as due to frozen ground or clasts, was recorded. Select points of refusal, typically those interpreted as possible frozen ground, were verified by instantaneous temperature measurements (adapted from Way and Lewkowicz, 2015). Temperatures were recorded with thermistors that were attached to a long dowel and inserted to the depth of refusal or to the full probe-depth of 120 cm. The temperatures were read-out by a Hobo 4-Channel UX120-006M Analog Data Logger (Onset) for a continuous period of at least 15 minutes to allow equilibration with the ground temperatures. These temperatures (±0.15°C accuracy) were used to confirm if the depth of refusal corresponded to a frost table, at which a temperature of <0°C would be obtained.

3.1.3 Vegetation Canopy Cover, Shrub Height, and Shrub Density

Forest canopies protect permafrost, as they provide shade, promote evapotranspiration, and intercept and reduce ground surface snow cover (Shur and Jorgenson, 2007; Chasmer et al., 2011). Up to 60% of seasonal snowfall can be intercepted by forest canopy, and up to 80% of this intercepted snow is returned to the atmosphere through sublimation (Pomeroy et al., 1998; Varhola et al., 2010). However, interception of seasonal snowfall varies with site conditions, including forest structure and composition (Revuelto et al., 2015).

Hemispherical photographs are widely used to describe and assess canopy structure in forest science (Frazer et al., 1997). In this study, two images were collected at each sampling location along the established vegetation transects. A levelled Samsung Galaxy A5 smartphone with an attachable fisheye lens (Lifetrons Travel Lens Set) was mounted on a selfie stick to ensure that the camera operator was not captured in the image. One image was collected at the ground surface to evaluate the total canopy cover. The second image was collected at shoulder height (1.3 m above the ground surface), with all images taken by the same camera operator. Overstory measurements from the shoulder height images were subtracted from the total canopy cover measurements from the ground level images at the same location to obtain the coverage provided by the understory, which primarily corresponded to shrubs (Figure 3-2). Deciduous shrubs that undergo a notable seasonal increase in biomass, such as dwarf birch (*Betula glandulosa* Mich.), tea-leaf willow (*Salix planifolia* Pursh), gray-leaf willow (*Salix glauca* L.), and green alder (*Alnus viridis* subsp. *crispa* [Aiton] Turr.), are expected to have greater ground-shading abilities than evergreen shrubs, such as Labrador tea (*Rhododendron groenlandicum* [Oeder] Kron and Judd). Computerized image analysis of the canopy structure was performed by batch processing in the open-source image processing program, ImageJ (Rasband, 2014). Due to issues of subjectivity and irreproducibility common to manual thresholding (Jarčuška, 2008), the hemispherical photographs were processed with an automatic threshold and binary conversion in ImageJ, with black representing vegetation and white representing sky (Nobis and Hunziker, 2005; Beckshäfer, 2015). Total gaps in the canopy were estimated using pixel counts, based on the total gap calculation in Bianchi et al. (2017) and adapted from Stewart et al. (2007) and Beckschäfer (2015). Images were not projected onto a hemisphere, as in the traditional canopy openness calculation (Bianchi et al., 2017), so pixels were not weighted according to their position on the hemisphere. This methodology consistently underestimates canopy closure and overestimates canopy openness (Bianchi et al., 2017) but is appropriate for this study, which focuses on relative differences in canopy cover along transects.

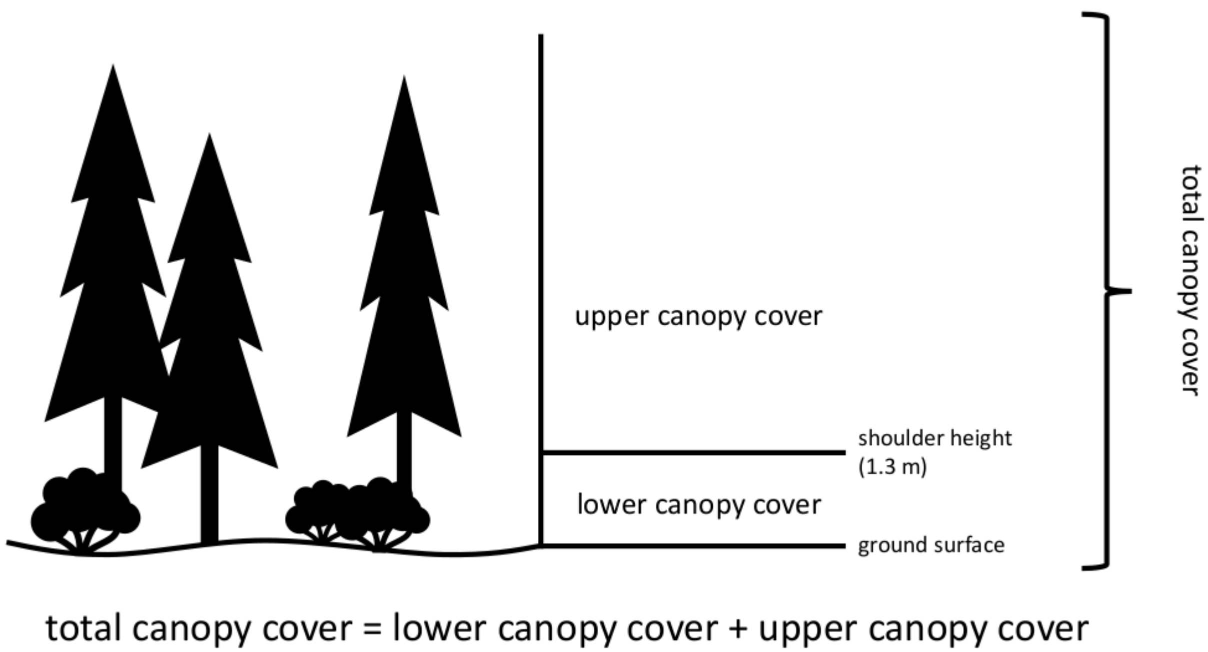

Figure 3-2. Schematic of Breakdown of Total Canopy Coverage.

The role and impact of shrubs on the ground thermal regime was also examined. Shrubs, like trees, may promote the persistence of permafrost through ground shading (Blok et al. 2010), particularly because they tend to have a higher leaf area index than the surrounding coniferous forest. However, unlike trees, shrubs are not especially adept at intercepting snowfall. Instead, trapping of wind-distributed snow can occur around shrubs, ultimately increasing snow depths and warming the ground in winter (Sturm et al., 2001). Where shrubs are tall and protrude above the snowpack, snow melt occurs earlier and the active layer thaws deeper, compared to areas with a later snow-free date (Wilcox et al., 2019) (Figure 3-3).

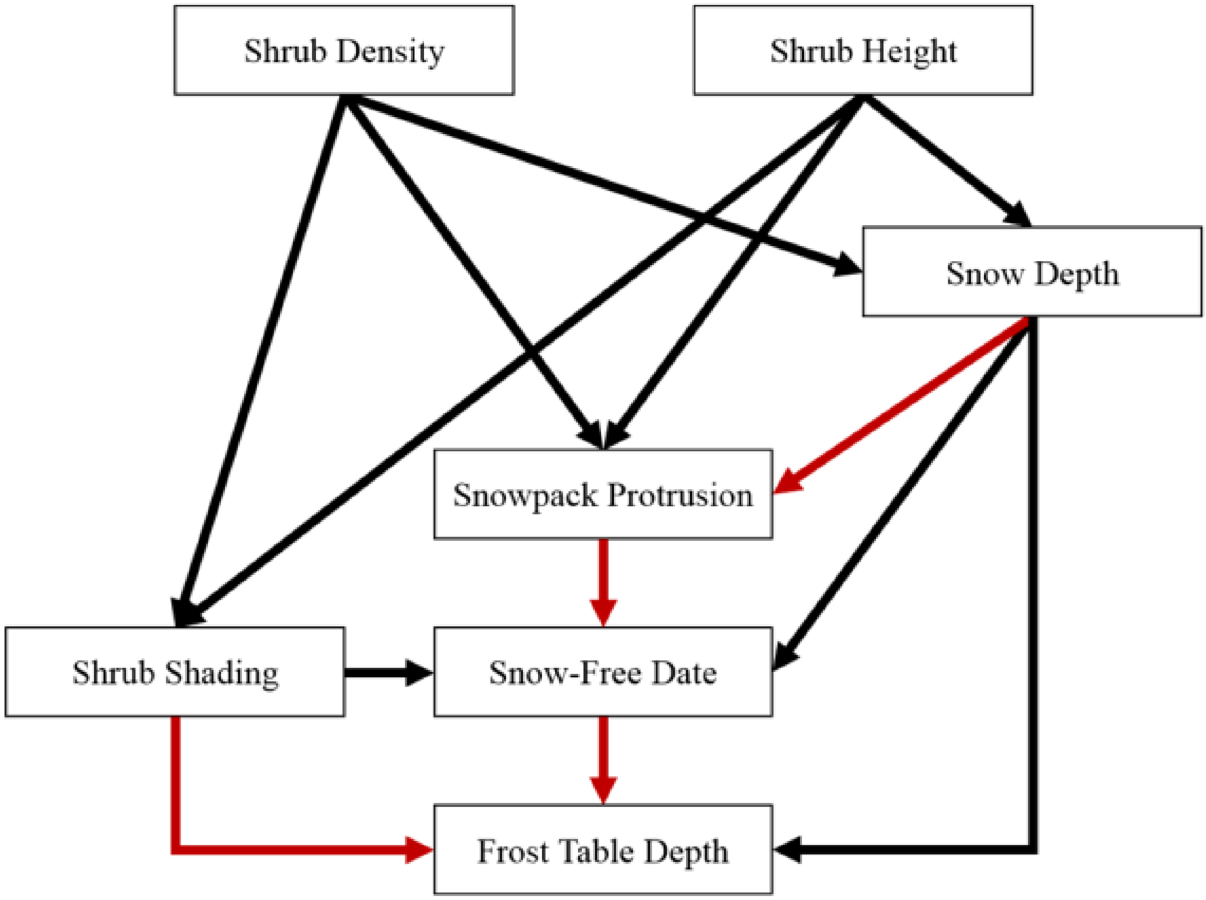

Figure 3-3. Model of Short-Term Physical Influences of Shrubs on Frost Table Depths, from Wilcox et al. (2019). Black arrows represent positive relationships. Red arrows represent negative relationships.

The canopy architecture of the shrub cover was investigated by manually measuring the number of shrub branches and the height of the tallest shrubs of each species within 0.25 m^2 plots, at 1 m intervals along vegetation transects established 1 m downslope of the ERT lines. Maximum heights of each shrub species within the sampling plots were recorded by measuring the vertical height from the ground surface to the tallest part of the shrub (adapted from Bean et al., 2003). Shrub densities were calculated by counting the number of stems and primary branches for each shrub species within each sampling plot (adapted from Caratti, 2006). Shrubs measuring less than 25 cm in height were omitted, as they were expected to have limited snow-trapping and ground-shading impacts.

3.1.4 Snow Depth and Density

Snow is a critical factor in permafrost distribution in discontinuous permafrost zones (Williams and Smith, 1989). The distribution, depth, and density of snow at a given site are influenced by the nature and structure of the vegetation at the site. Snow characteristics have been recently identified as an understudied element in the post-fire permafrost system (Holloway et al., 2020).

Snow depths were measured along the ERT transects using a standard 230 cm-long avalanche probe. At TB and WB, snow depth measurements were made in late-March 2018 (Table 3-1). This was approximately 60% of the way through the snow-on-ground season, representing 85 to 100% of that season’s maximum snow depth at these sites. At the BR site, snow depths were measured on February 18, 2019 (Table 3-1), just past the halfway point of the 214 day-long snow-on-ground season, which lasted from October 23, 2018 to May 25, 2019 (Figure 3-4). At the time of measurement at BR, snow depths had reached 87 and 94% of the maximum depths recorded in the burned and unburned regions, respectively (Figure 3-4).

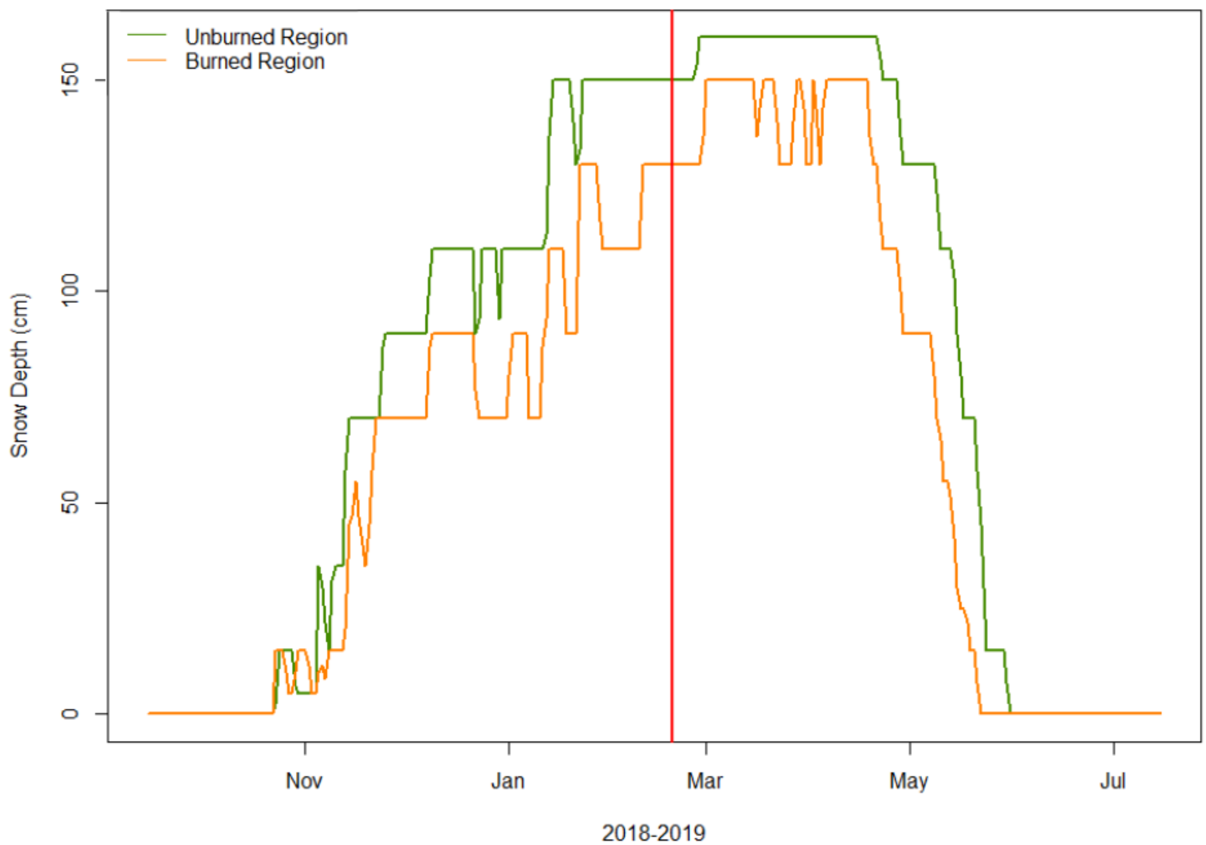

Figure 3-4. Timing of Snow Depth Measurements (shown in red) Relative to Duration of 2018-2019 Snow-On-Ground Season at the BR Site.

3.1.5 Ground Surface and Soil Properties

Near the southern limit of Canadian permafrost, perennially frozen ground is typically restricted to peatlands, or sites with thick organic mats (Zoltai, 1972; Payette et al., 2004). The presence of an organic layer can be crucial for the persistence of permafrost, particularly under unfavourable climate conditions (Shur and Jorgenson, 2007). The cooling effect of organic material is attributed to its large seasonal range in moisture contents and thermal conductivities, resulting in large thermal offsets.

Organic layer thickness was measured at 1 m intervals along the ERT lines by inserting a 50 cm-long aluminum rod to the depth where the mineral soil resisted penetration. Small pits were dug to the top of the mineral soil in several locations at each site to verify the organic layer thickness estimates.

Soil moisture and temperature are important variables that may relate to organic layer thicknesses in black spruce stands (Kasischke and Johnstone, 2005; Barrett et al., 2010). Following fire, soil temperatures and moisture are expected to increase due to loss of vegetation and reduced evapotranspiration (Holloway et al., 2020).

Soil temperature (±1.5°C accuracy) and volumetric moisture content (±0.03 cm^3/cm^3 accuracy) were recorded with a WET Sensor and HH2 Moisture Meter Version 2.3 (Delta-T). Three measurements of volumetric soil moisture and soil temperature were taken and averaged for each sampling location at 1 m intervals along the 40 m-long ERT lines and at 2 m intervals along the 80 m-long ERT lines. While these measurements are instantaneous and do not represent mean annual values, they are useful for evaluating relative differences in intra-site soil temperature and moisture.

3.2 Laboratory Analyses

Soil properties, including gravimetric moisture content (GMC), organic matter content, carbonate content, particle size distribution, and dry bulk density, were derived from organo-mineral soil samples that were collected at each study site. Organic material samples were also collected at the sites, from which dry bulk densities were measured. These parameters were incorporated into calculations of material properties in the thermal modelling process, described in Chapter 5.

3.2.1 Organo-Mineral Sample Collection and Analysis

Eight organo-mineral soil samples were collected at each site, at depths of approximately 40 cm. Samples were limited to this depth by permitting regulations associated with the research project. Samples were collected with a small trowel, stored in Ziploc bags, and shipped to the University of Ottawa for laboratory analysis.

GMC was calculated with the following equation (van Everdingen, 2005), where WW is the wet weight in grams and DW is the dry weight in grams:

$$GMC\ (g/g) = \frac{WW\ (g) - DW(g)}{DW\ (g)} \tag{3-1}$$

The organic matter of the sediment samples were quantified by the loss-on-ignition (LOI) method (Heiri et al., 2001). Subsamples of approximately 3 to 4 g were placed in crucibles and loaded into the Leco Corporation TGA701 Thermogravimetric Analyzer for quantification of the organic matter by mass loss with sequential heating. The samples were first heated to 105ºC to ensure complete sample dryness, followed by heating to 550ºC for loss of organic matter. The content of organic matter in the samples were calculated with the following equation (Heiri et al., 2001), where DW represents dry weight in grams:

$$organic\ matter\ content\ (\%) = LOI_{550}(\%) = \frac{DW_{105}\ (g) - DW_{550}\ (g)}{DW_{105}\ (g)} \times 100\ \% \tag{3-2}$$

All samples were analyzed in reference to a calcium oxalate ($C_2H_2CaO_5$) standard, with a mean organic matter content of 31.35%. Based on this calcium oxalate standard, the analytical accuracy is defined as ±0.01% or ±0.0001 g.

Sediment sample particle size was determined with laser particle analysis. Sediment samples were treated with hydrogen peroxide (H_2O_2) to remove organic matter and to avoid misinterpretation of mineral particle size. The treated mineral samples were suspended in sodium hexametaphosphate ($Na(PO_3)_6$), and loaded into the Microtrac S3500 for particle size and soil texture analysis. The percent composition of sand (<2000 μm and >62.5 μm), silt (<62.5 μm and >3.5 μm), and clay (<3.5 μm and >0. 02 μm) were averaged from duplicates taken for each sample. Sediment textures ranged from silty-sand at TB and WB to sandy-silt at BR. At TB, surficial materials consisted of a silty-sand, with an average composition of 65% sand, 34% silt, and 1% clay (±3% standard deviation). Surficial materials at WB were primarily sand, with an average composition of 86% sand and 14% silt (±2% standard deviation). At BR, surficial materials were more fine-grained than at the two northern sites, and sediments were composed of a mixture of 31% sand, 58% silt, and 11% clay (±2% standard deviation).

The dry bulk density (dBD) of the organo-mineral samples were calculated using the following equation (Hossain et al. 2015), using LOI-derived organic matter content estimates:

$$dBD_{org-min}\ (g/cm^3) = 0.075 + 1.301^{-0.06 \times organic\ matter\ content\ (\%)} \qquad (3\text{-}3)$$

3.2.2 Organic Material Sample Collection and Analysis

At least four organic layer samples of approximately 10 × 10 × 8 cm were collected at each study site to determine dry bulk density of the organic layer. In this study, the samples were collected at the ends of each of the ERT transects. The samples were carefully cut to the base of the organic material and collected with a small saw and trowel. The sampling depth varied at each location, due to local differences in organic material thickness. Samples were stored in Ziploc bags and shipped to the University of Ottawa for laboratory analysis.

The dBD of the organic layer was determined according to the following equation from Heng (2008), where *DW* is the weight in grams, and *V* is the volume of the initial sample in mL:

$$dBD_{org}\ (g/cm^3) = \frac{DW(g)}{V\ (cm^3)} \qquad (3\text{-}4)$$

Calculated and estimated dBD values were found to be consistent with those in the literature (e.g., Boelter, 1968; Pollard and French, 1980).

3.2.3 Application of Laboratory-Based Sediment Properties to Modelling Process

Laboratory-based parameters were used to estimate the volumetric fractions of each of the constituents in the material layers used in the thermal models. The material layers were assumed to be saturated, as in McClymont et al. (2013) and Instanes (2016), so air was absent from all material layers.

The volumetric fraction of moisture or the volumetric moisture content (VMC), as water ($fraction_{water}$) or ice ($fraction_{ice}$), was calculated by multiplying the GMC, measured from collected field samples, by the dBD, as described in Heng (2008):

$$VMC\ (cm^3/cm^3) = GMC\ (g/g) \times dBD\ (g/cm^3) \tag{3-5}$$

Using the principles from Heng (2008) for the VMC, the volumetric fraction of the organic material was also calculated by multiplying the LOI-derived gravimetric organic matter content by its dBD, as follows:

$$volumetric\ organic\ content\ (cm^3/cm^3) = gravimetric\ organic\ content\ (g/g) \times dBD\ (g/cm^3) \tag{3-6}$$

The volumetric fraction of the mineral material was calculated by subtracting the water or ice fraction and the organic material fraction from a total 100%.

$$volumetric\ mineral\ content\ (cm^3/cm^3) = 1 - (volumetric\ organic\ content\ (cm^3/cm^3) + VMC\ (cm^3/cm^3)) \tag{3-7}$$

3.3 Modelling Parameters and Process

Modelling was carried out using TEMP/W (Geoslope), a finite element, geothermal modelling software. TEMP/W has been widely used in infrastructure-related studies for permafrost areas, including modelling of ground temperature change in roads (Darrow, 2011; Batenipour et al., 2013), around pipelines (Smith and Riseborough, 2010), and under buildings (Instanes, 2016; Perreault and Shur, 2016). The simulations in this thesis are one-dimensional, although the software does permit two-dimensional analyses.

The following section contains a description of the thermal modelling methodology used in Chapter 5. Site-specific details of the modelling process are included in this section for justification purposes.

3.3.1 Thermal Modelling Inputs

A one-dimensional idealised material profile was developed for each study site, comprising an upper organic layer, a layer of organo-mineral material, and a silty-sand layer over bedrock. The material stratigraphy and boundaries were estimated from field measurements of organic layer thickness, interpretations of sub-surface geophysical investigations, and our understanding of the physical landscape of the region (Bell et al., 2011). The base of the model was set at 100 m, which is at the high end of previous studies (Table 3-2), but it ensures that long-term heat flows into the permafrost are properly represented in the model.

Table 3-2. Selected Relevant Permafrost Modelling Studies.

Modelling Purpose	Model Used	One- or Two-Dimensional	General Location	Duration of Modelling	Model Domain Thickness (m)	Reference
Investigate effects of varying snow properties on drilling-mud sumps in permafrost	TEMP/W	Two	Northwest Territories, Canada	>40 years	5	Kokelj et al. (2010)
Investigate response of permafrost under a highway embankment to climate warming	TEMP/W	Two	Alaska, United States	55 years	30	Darrow (2011)
Investigate effects of vegetation disturbance and climate warming on permafrost thaw	TEMP/W	Two	Northwest Territories, Canada	50 years (1986-2036)	50	Smith and Riseborough (2010)
Investigate effects of canopy removal and climate warming on permafrost thaw	TEMP/W	Two	Northwest Territories, Canada	6 years (2004-2010)	50	McClymont et al. (2013)
Investigate response of permafrost under a highway embankment to climate warming	TEMP/W	Two	Manitoba, Canada	3 years (2008-2011)	22	Batenipour et al. (2013)
Investigate effects of climate warming on permafrost beneath snow-cleared construction sites	TEMP/W	One	Northwest Russia and Svalbard, Norway	85 years (2015-2100)	20	Instanes (2016)
Investigate impacts of seasonal thermal insulation on underlying permafrost	TEMP/W	Two	Alaska, United States	30 or 45 years	23.8	Perreault and Shur (2016)
Investigate post-fire permafrost response	GIPL	One	Alaska, United States	120 years (from 1983)	20	Jafarov et al. (2013)
Investigate post-fire permafrost response	GIPL	One	Alaska, United States	100 years (2000-2100)	100	Treat et al. (2013)
Investigate post-fire permafrost response	GIPL	One	Alaska, United States	83 years (1930-2013)	100	Brown et al. (2015)
Investigate post-fire permafrost response	NEST	One	Northwest Territories, Canada	157 years (1943-2100)	120	Zhang et al. (2015)

3.3.1.1 Material and Mesh Properties

The TEMP/W thermal modelling program requires user-defined material property inputs of volumetric moisture content, frozen and unfrozen material thermal conductivity, and frozen and unfrozen material specific heat capacity. The thermal conductivities and specific heat capacities require estimates of the volumetric fractions of each of the material's constituents (i.e., organic material, mineral material, and water or ice; Table 3-3). For modelling purposes, the upper organic stratigraphic layer was assumed to contain no mineral material, and the sand and bedrock stratigraphic layers at depth were assumed to contain no organic material. Materials were assumed to be saturated.

Table 3-3. Material Layers and their Constituents.

Material Layer	Constituents
Organic Layer	Organic Material + Water/Ice
Organo-Mineral Layer	Organic Material + Mineral Material + Water/Ice
Mineral Layer	Mineral Material + Water/Ice
Bedrock Layer	Mineral Material + Water/Ice

Model mesh elements increased in thickness with depth. Beneath the organic layer and within the mineral and bedrock layers, elements measured 0.05 m thick to a depth of 3 m, 0.1 m thick from 3 m to 30 m, 0.5 m thick from 30 m to 50 m, 1 m thick from 50 m to 70 m, and 1.5 m thick from 70 m to 100 m. Elements were only 0.01 m thick within the organic layer to facilitate reduction of the organic material thickness due to the burn and accumulation of the organic material over time.

The frozen and unfrozen thermal conductivities of each material layer were calculated using a geometric mean, as in Johansen (1975) and Farouki (1981), based on the volumetric fractions and thermal conductivities of the material's constituents (Table 3-4).

Frozen thermal conductivity (k_f) was calculated according to the following equation:

$$k_f(W/m/K) = fraction_{org}{}^{k_{org}(W/m/K)} \times fraction_{min}{}^{k_{min}(W/m/K)} \times fraction_{ice}{}^{k_{ice}(W/m/K)} \tag{3-8}$$

Unfrozen thermal conductivity (k_u) was calculated according to the following equation:

$$k_u(W/m/K) = fraction_{org}{}^{k_{org}(W/m/K)} \times fraction_{min}{}^{k_{min}\,(W/m/K)} \times fraction_{water}{}^{k_{water}(W/m/K)} \tag{3-9}$$

Table 3-4. Standard Thermal Conductivities of Various Materials. (Source: Williams and Smith, 1989, Table 4.1).

Material	Thermal Conductivity (W/m/K)	Abbreviation
Organic Material	0.250	k_{org}
Mineral Material	2.920	k_{min}
Water	0.560	k_{water}
Ice	2.230	k_{ice}

The frozen and unfrozen heat capacities of each material layer were calculated using a weighted average, as in Johnston (1981), based on the volumetric fractions and heat capacities of the material's constituents (Table 3-5).

Frozen heat capacity (c_f) was calculated according to the following equation:

$$c_f(MJ/m^3/K) = \left(fraction_{org} \times c_{org}\,(MJ/m^3/K)\right) + (fraction_{min} \times c_{min}\,(MJ/m^3/K)) + (fraction_{ice} \times c_{ice}\,(MJ/m^3/K)) \tag{3-10}$$

Unfrozen heat capacity (c_u) was calculated according to the following equation:

$$c_u(MJ/m^3/K) = \left(fraction_{org} \times c_{org}\,(MJ/m^3/K)\right) + (fraction_{min} \times c_{min}\,(MJ/m^3/K)) + (fraction_{water} \times c_{water}\,(MJ/m^3/K)) \tag{3-11}$$

Table 3-5. Standard Volumetric Heat Capacities of Various Materials (Source: Johnston, 1981, Table 3.9).

Material	Heat Capacity (MJ/m³/K)	Abbreviation
Organic Material	2.520	c_{org}
Mineral Material	1.875	c_{min}
Water	4.187	c_{water}
Ice	1.880	c_{ice}

3.3.1.2 Boundary Conditions

The TEMP/W thermal modelling program requires user-defined boundaries of a ground surface boundary at the top of the profile and a geothermal heat flux at the base of the profile.

3.3.1.2.1 Ground Surface Boundary

The ground surface boundary is applied to the top of the organic material layer. Different ground surface boundaries, defined by freezing and thawing n-factors (n_f and n_t), and a daily temperature record, were applied during the spin-up and transient phases of the model. N-factors are ratios of the air temperature to the ground surface temperature at a given site, and they can be used to characterize the effects of seasonal factors such as snow depth, snow density, canopy cover, and overall radiation balance (Karunaratne and Burn, 2004; McClymont et al., 2013). The n-factors were calculated according to the following equations from Karunaratne and Burn (2004), where FDD is freezing degree-days and TDD is thawing degree-days:

$$n_f = \frac{FDD_{ground\,surface}\ (degree\ days)}{FDD_{air}\ (degree\ days)} \tag{3-12}$$

$$n_t = \frac{TDD_{ground\,surface}\ (degree\ days)}{TDD_{air}\ (degree\ days)} \tag{3-13}$$

The historical daily air temperature record that was incorporated into the ground surface boundary was derived and adjusted from the gridded Berkeley Earth Surface Temperature (BEST) analysis product, available through the KNMI Climate Explorer Database. As in Way and Viau (2015), BEST was selected for use because it is homogenized across an extensive meteorological data network, and it has a long record, extending back to 1880 (Rohde et al., 2013). Site-specific historical daily air temperature records were generated for WB and TB using linear regression models (Table 3-6) based on air temperatures measured at the two sites (see Section 3.1.1) during the overlap period of July or August 2017 to May 31, 2018. The equations predict site-specific air temperatures for the two sites as a function of BEST air temperatures.

Table 3-6. Summary of Linear Regression Models to Predict Daily Air Temperatures at WB and TB Sites from the Berkeley Earth Surface Temperature (BEST) Time Series.

Site	Overlap Period (mm-dd-yyyy)	Number of Observations	Linear Regression Model	Adjusted R^2	Residual Standard Error
WB	07-19-2017 to 05-31-2018	315	$y = 1.052x - 0.146$	0.97	1.83 (313 df)
TB	08-11-2017 to 05-31-2018	294	$y = 1.091x + 0.039$	0.97	1.89 (292 df)

Both linear regression models produce normally distributed residuals (Figure 3-5-ABii). The plots of residuals and scale-location as a function of fitted values are both scattered with no distinct pattern, and the line of lowest fit of the residuals versus fitted values plots are very close to 0 (Figure 3-5-ABi/iii). The Cook's distance residuals versus leverage plot shows all residuals being below 1 (Figure 3-5-ABiv). Finally, the p-value of 2.2×10^{-16} for both sites indicates that these models are both statistically significant, and the models were deemed appropriate for predicting site-specific air temperatures based on the BEST time series.

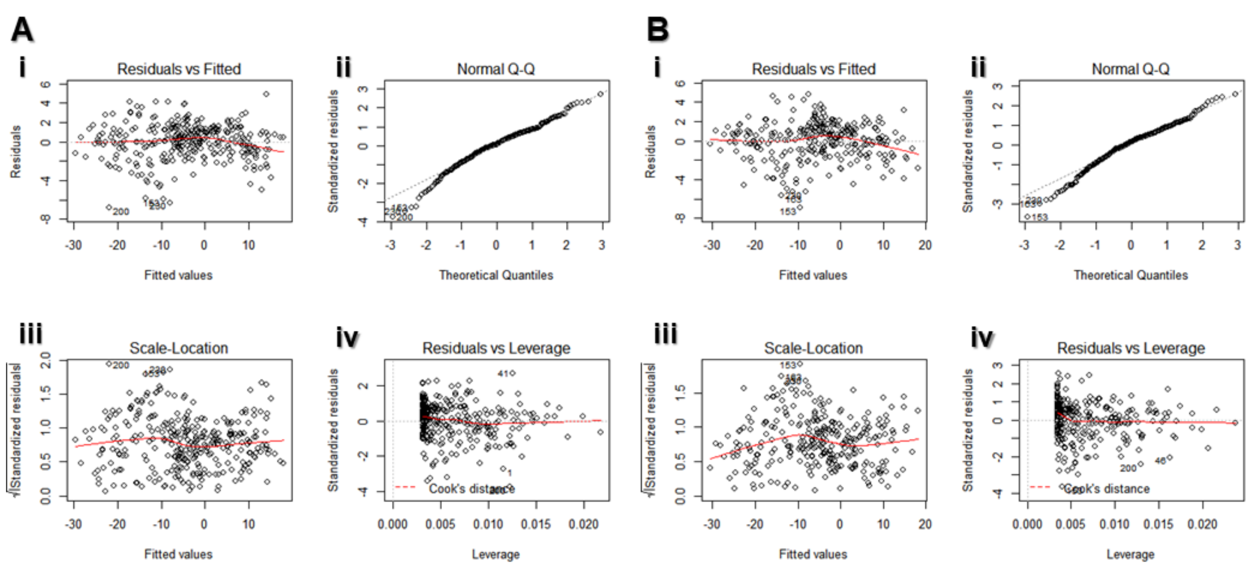

Figure 3-5. Summary of Residuals of Linear Regression Models (i) residuals versus fitted; ii) normal Q-Q; iii) scale-location; iv) residuals versus leverage) for Measured Air Temperatures at A) WB and B) TB Sites as a Function of Berkeley Earth Surface Temperature (BEST) Time Series.

Future air temperature projections were derived from a suite of four statistically downscaled climate scenarios (CanESM2, CESM1-CAM5, HadGEM2-ES, and MIROC-ESM) previously used in a study of national wildfire activity through the 21st century (Hope et al., 2016). All four models were considered under representative concentration pathways (RCP) 4.5 and 8.5, which correspond respectively to scenarios of radiative forcing stabilization shortly after 2100, and of high and continuously increasing greenhouse gas concentration levels (van Vuuren et al., 2011). The lowest pathway, RCP2.6, was not considered, as it now represents an unrealistic reduction in greenhouse gas emissions over time (van Vuuren et al., 2011). A mean projection of the four global circulation models was calculated for both the RCP4.5 and RCP8.5 scenarios. The concept of model democracy was applied to the composite projection, in which equal weight was given to each of the four models.

The projected composite daily temperature record was assembled and adjusted using an overlap period of 7 years between the suite of projected models and the adjusted site-specific BEST historical temperature record. Daily anomalies were generated by comparing an averaged year of data, across 2010 to 2017, from the historical and projected datasets. Daily anomalies were applied to each day of the mean future daily temperature records, from January 1, 2018 to December 31, 2099, to generate a site-specific estimate of future daily air temperatures to the end of this century (Figure 3-6). This step preserved the continuity of the air temperature record, through the shift from the BEST dataset to the composite projected model.

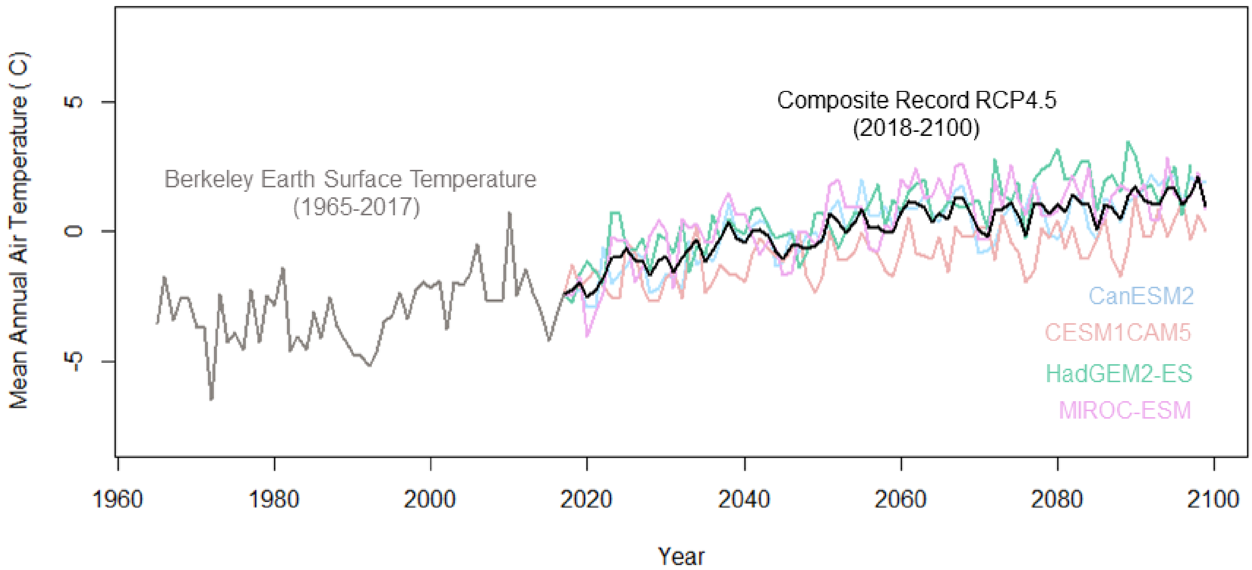

Figure 3-6. Site-Specific Long-Term Mean Annual Air Temperature Record for WB under RCP4.5. The air temperature record combines site-specific historical and projected air temperatures. Daily historical air temperatures (1965-2017) were assembled from a regional Berkeley Earth Surface Temperature record. Daily projected air temperatures (2018-2100) were averaged from statistically downscaled climate scenarios CanESM2, CESM1-CAM5, HadGEM2-ES, and MIROC-ESM.

3.3.1.2.2 Geothermal Heat Flux

The coastal Labrador region is characterized by a low geothermal heat flux (Mareschal et al., 2000; Majorowicz and Minea, 2012), which facilitates the development and persistence of thick, yet warm permafrost. Mareschal et al. (2000) report an extremely low heat flow estimate of 22 mW/m^2 near the Voisey's Bay nickel mine, located approximately 30 km south-west of the community of Nain. This value is consistent with estimates made by Majorowicz and Minea (2015), based on previous work performed by Blackwell and Richards (2004) and Majorowicz and Minea (2012). The marginality of the heat flow is likely attributable to a low concentration of radioelements in the surrounding region's crust (Mareschal et al., 2000).

Initial model calibration attempts using a geothermal heat flux of 22 mW/m^2 and a ground surface temperature boundary obtained with a mean annual air temperature of -3.2°C resulted in an estimate of more than 50 m of permafrost, which is not thought to be representative of regional permafrost conditions. For modelling purposes, therefore, the geothermal heat flux value was increased to 220 mW/m^2, which is justified by considering the potential warming impacts of surrounding unfrozen ground on frozen ground within a discontinuous permafrost region (Buteau et al., 2004). A flux of 220 mW/m^2 is still considerably lower than the 340 mW/m^2 used by Buteau et al. (2004) and 540 mW/m^2 and 1020 mW/m^2 used by Way et al. (2018) for modelling of permafrost mounds in northern Quebec and southern Labrador, respectively.

3.3.2 Thermal Modelling Process

The thermal modelling process comprised an initial spin-up period, followed by a transient model until the time of the fire disturbance, through to 2099 (Figure 3-7). Within the spin-up stage, the model was run over 100-year periods. The first transient stage, from 1965 to the time of the fire disturbance, was run all at once. From the time of the fire disturbance to the end of the century, the model was run on five-year intervals to permit gradual alterations to the organic layer thickness and the freezing and thawing n-factors. Shorter intervals were used within the five years before and after 2018, to account for a shift in the air temperature record input, from the historical record, running from January 1, 1965 to December 31, 2017, to the modelled future record, running from January 1, 2018 to December 31, 2099. In each case, the last ground temperature profile output from the previous model was input as the initial ground temperature profile for the next model.

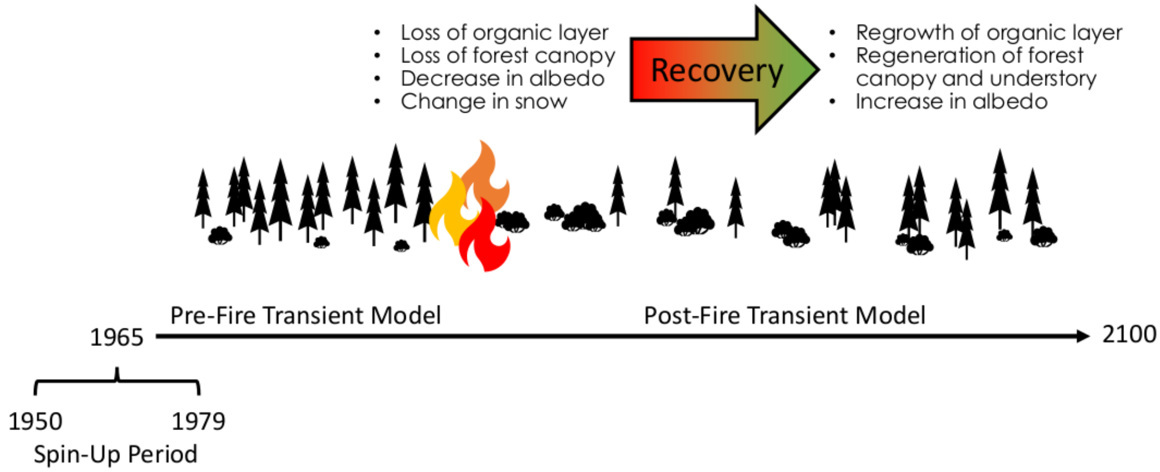

Figure 3-7. Schematic of Modelling Process and Post-Fire Recovery Process.

TEMP/W was run with half-hour time steps and daily air temperature inputs. For each time step, the model was permitted to iterate its solution up to 900 times until convergence within ±0.005 K was achieved.

A total of four basic simulations were run for each site: 1) no disturbance under a moderate emissions scenario (RCP4.5); 2) fire disturbance under a moderate emissions scenario (RCP4.5); 3) no disturbance under an aggressive emissions scenario (RCP8.5), and; 4) fire disturbance under an aggressive emissions scenario (RCP8.5).

3.3.2.1 Spin-Up Period

The thermal model was first initialized with a spin-up period, in which ground conditions were run to equilibrium with air temperatures from the 1950-1979 climate normal. A synthetic year of air temperatures, averaged across the 1950-1979 climate normal, was generated and repeatedly applied to the ground surface boundary until equilibrium was achieved. Ground conditions were considered to be in equilibrium with the applied boundary once the temperature at each node varied by less than 0.01 K over a period of 100 years.

Following spin-up, the initial ground thermal conditions were considered to be in equilibrium with 1965, which marks the middle of the 1950-1979 climate normal period. The model was run forward with the site-specific BEST historical air temperature record from 1965 to the time of the fire disturbance.

3.3.2.2 Fire Disturbance and Post-Fire Recovery Process

The fire disturbance was represented in the model by decreasing the organic layer thickness, decreasing n_f, and increasing n_t. These adjustments were applied on August 1 of the year of the fire disturbance for each site. This date was chosen because it represents the middle of the Labrador fire season, which, for recent years like 2018 and 2019, lasted from May 15 to September 30 (Government of Newfoundland and Labrador, 2019), and because the exact date of the fire disturbances is not known.

The adjustments to the organic layer thickness and n-factors following fire were chosen based on the field data collected from the burned and unburned regions of each of the study sites.

The reduction in organic layer thickness at the time of the fire is linked to burn severity, with a higher burn severity corresponding to a greater decrease. In order to determine the required reduction in organic layer thickness at the time of the fire event, the rate of accumulation of the organic layer was first calculated for each site by comparing the measured organic layer thicknesses in the burned versus unburned regions of the study sites in summer 2018. This calculation requires two assumptions. First, the organic layers in the burned and unburned regions are assumed to be, on average, the same thickness, prior to the fire disturbance. The second assumption is that organic material continues to accumulate at equal linear rates in both the burned and unburned regions. Therefore, the difference between the organic layer thickness in the burned region relative to the unburned region divided by the number of years since the fire disturbance is understood to represent the rate of accumulation of organic material at the site. This resulted in a rate of accumulation of approximately 3 mm/year for both sites. These values are slightly higher than the linear regeneration rate of approximately 2 mm/year calculated from a study of post-fire soil conditions in interior Alaska (Yi et al., 2010). The higher rates reflect the wetter climate of the coastal Labrador region, which promotes the productivity and growth of mosses that make up the upper portion of the organic layer (Williams and Flanagan, 1998). By applying the calculated accumulation rate to the measured organic layer thicknesses, it was possible to estimate the organic layer thicknesses in the unburned and burned regions at the time of the fire disturbance.

N_t incorporates the influence of several variables, including soil moisture and vegetation cover (Klene et al., 2001; Karunaratne and Burn, 2004). N_t tends to remain relatively stable from one year to the next, while n_f, which is primarily influenced by variations in snow cover, density, and distribution, exhibits greater inter-annual variability (Karunaratne and Burn, 2003; Karunaratne and Burn, 2004). However, for modelling purposes, air temperatures varied on an inter-annual basis, but n_f and n_t were kept constant except following fire.

Adjustments to n_f and n_t following fire were applied using a two-segment linear pattern (see Zhang et al., 2015). Full recovery of vegetation to pre-fire conditions took place over 50 years, with 66.6% of the recovery in the first 25 years and 33.3% in the second 25-year period (Zhang et al., 2015). This pattern is consistent with a remote sensing-based study of fire-disturbed forests in southern Labrador, in which an average of 44 years was required to reach a recovery threshold, corresponding to 80% of the pre-fire conditions (Miranda et al., 2016). Recovery for forest fire sites in Nunatsiavut is expected to take longer than in southern Labrador, due to the cooler climate and less suitable conditions for tree establishment.

Following fire, a minimum threshold of 0.05 was applied to n_f, representing a ratio of air FDD to ground surface FDD of 20. This minimum threshold value is the average of n_f values measured by Way and Lewkowicz (2016) at 16 sites located in temperate or subpolar needleleaf forests, subpolar taiga needleleaf forests, and mixed forests in Labrador. In western North America, very few permafrost-related studies have reported n_f values as low as or lower than 0.1 (e.g., Taylor, 1995; Jorgenson et al., 2010; Cable et al., 2016). It is unlikely that n_f would fall below the minimum applied threshold of 0.05, even during the immediate post-fire period.

3.3.3 Model Output Validation

The model was validated using comparisons with measured ground surface temperatures during 2017-2018. Validation of ground temperatures at greater depths could not be performed, as boreholes were not established at the study sites due to permitting regulations associated with the overall research project.

The model was verified at this stage by identifying the depth of the base of permafrost, the depth of zero annual amplitude, the temperature of at the depth of zero annual amplitude, and the active layer thickness from 2017 to 2018. We expected to generate a body of warm permafrost at the WB site of a reasonable thickness, not exceeding 20 m in depth. The active layer was expected to range between 60 cm and 1 m, based on the climatic conditions at the site, and the depth of zero annual amplitude was expected to range between 6 m and 22 m (Lévesque et al., 1990 in Allard et al., 2012).

The thermal offset of -1.0°C that was produced under equilibrium conditions for 1965 was also used to verify the model. The thermal offset refers to the temperature difference between the temperature at the top of permafrost and the mean annual ground surface temperature. Locations with permafrost in Canada with a mean annual air temperature of around -3°C may be expected to have a corresponding thermal offset of around -2°C (Smith and Riseborough, 2002). However, the thermal offset at a given location is greatly influenced by the thermal conductivity of the ground materials, which are based on moisture content, sediment grain size and density, and mineral composition (Williams and Smith, 1989). Thermal offsets ranging between -1°C and -2°C have been measured at north-facing forested sites in mountain permafrost environments in British Columbia (Hasler et al., 2015).

3.3.4 Processing of Model Outputs

The TEMP/W program produced individual CSV files for each model interval of daily temperatures (columns) over the entire period of study for every node (rows) within the model domain of 100 m. This massive data output was processed in R to produce annual trumpet curves for the beginning of the period of study (1965), selected years preceding the fire disturbance, the year preceding the fire disturbance (2000 for TB and 2003 for WB), and every year following the fire disturbance until 2099. The depth of zero annual amplitude, the temperature of the permafrost, the base of the active layer, the top of the permafrost, and the base of the permafrost could be extracted for each year from the maximum, minimum, and mean curves of each trumpet curve, using specified temperature thresholds applied while moving up and/or down the profile.

The depth of zero annual amplitude is defined as the first depth, moving from the surface to the base of the profile, at which the range between the maximum and minimum temperatures is less than 0.1 K. The temperature of the permafrost is the temperature at the depth of zero annual amplitude.

The base of the permafrost is defined as the next depth following the last depth at which the maximum temperature, moving from the base to the surface of the profile, is warmer than the specified threshold.

The top of the permafrost is defined as the first depth at which the maximum temperature, going from the surface to the base of the profile, is cooler than the specified threshold. If no talik has formed, the top of the permafrost is at the same depth as the base of the active layer.

The base of the active layer is defined in two ways, based on the presence or absence of a talik. In the absence of a talik, the active layer is defined by the depth to which seasonal thawing occurs, whereas if a talik is present, the active layer is defined by the depth of seasonal freezing. When a talik is absent, the base of the active layer is the first depth at which the maximum temperature, moving from the surface to the base of the profile, is cooler than the threshold. When a talik is present, the base of the active layer is the first depth at which the minimum temperature, moving from the surface to the base of the profile, is warmer than the threshold.

Based on standard definitions (van Everdingen, 2005), 0°C should normally be used as the threshold temperature for the top and base of permafrost and the boundaries of any taliks present, whereas strictly speaking, the base of the active layer should relate to the temperature at which freezing commences. However, when temperature gradients are very gentle, the boundary between ground temperatures ≤0°C and >0°C can shift rapidly because no latent heat is released in the model at exactly 0°C. For this reason, a range of temperature thresholds was used, representing different unfrozen moisture content values (Table 3-7). As soils are subjected to falling temperatures, some of the water changes to ice at an activation temperature just below 0°C, while the remainder is present in liquid form as films around individual particles (Spaans and Baker, 1996). This unfrozen moisture clings to particles through a combination of capillarity, adsorption, and the presence of dissolved salts, which can depress the freezing point of the body of soil (Spaans and Baker, 1996; French, 2017). The unfrozen moisture content at a given temperature can be defined by an unfrozen moisture content curve, which is also referred to as the soil freezing characteristic curve (Spaans and Baker, 1996). Unfrozen moisture content curves vary by soil type, with coarser soils, like sands, having less unfrozen moisture content than finer soils, like clays, at the same sub-zero temperature (Williams and Smith, 1989; French, 2017). In TEMP/W, a default unfrozen moisture content curve for sand was applied to all material layers. Selected temperature thresholds and their corresponding fractional unfrozen moisture contents are presented in Figure 3-8. Applying a range of temperatures and unfrozen moisture contents improves interpretations of regions of frozen ground (<11.39% unfrozen moisture content, <-0.025°C), unfrozen ground (100% unfrozen moisture content, >0°C), and partially frozen ground (11.40-99.99% unfrozen moisture content, 0°C to -0.025°C).

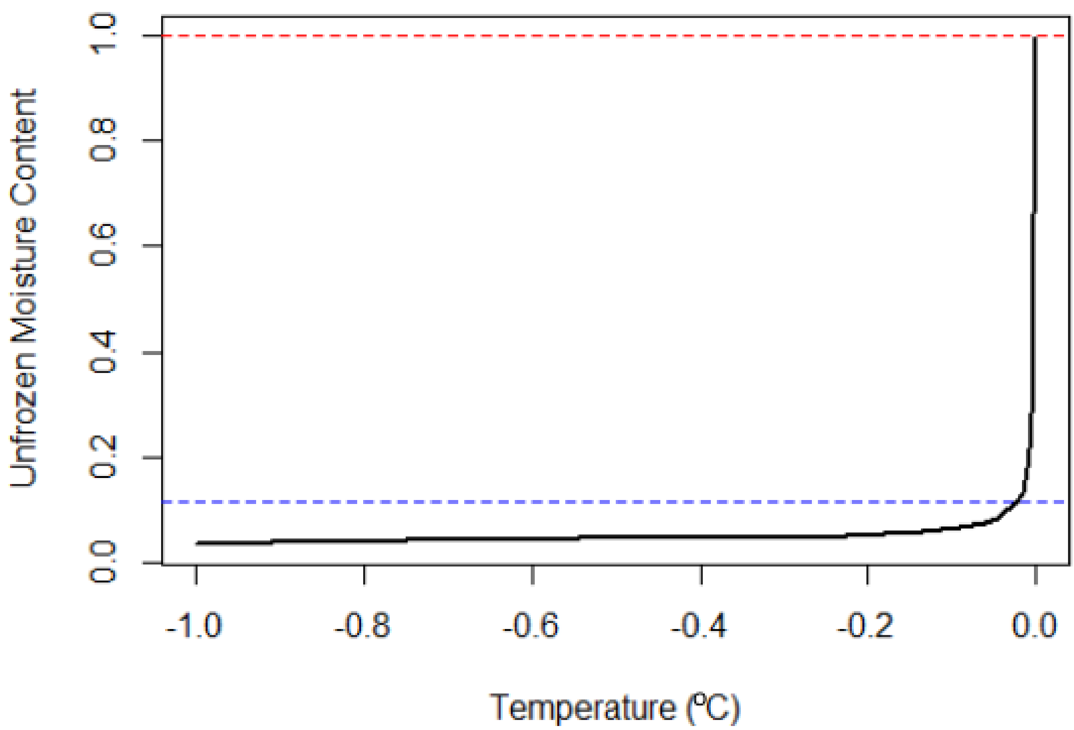

Figure 3-8. Default Unfrozen Moisture Content Curve for Sand in Temp/W. Thresholds for interpretations of unfrozen ground (red) and frozen ground (blue) are shown as dotted lines.

Based on these parameters, the thickness of the active layer, the thickness of the permafrost, and the thickness of a talik, if present, were determined for each year within the period of study.

The R code used to process and visualize the raw TEMP/W output is included in Appendix B. The rowMaxs and rowMins functions from the matrixStats package (Bengtsson et al., 2019) were used to extract the maximum and minimum values across the rows corresponding to a given year. These values were assembled to generate the maximum and minimum curves for each trumpet curve.

3.4 Statistical Analyses

The statistical analyses performed in this thesis were limited to those of an exploratory nature The exploratory data analysis (EDA) involved inter-site comparisons of snow depth, near-surface resistivity, organic layer thickness, average instantaneous soil temperature, average instantaneous soil moisture, total canopy cover, understory canopy cover, maximum shrub height, and shrub density using boxplots. Normality was visually assessed with Q-Q probability plots during the exploratory process. Intra-site relationships between the ecological variables were examined through Principal Components Analysis (PCA). PCA was applied to reduce the dimensionality of these numerical variables in each site. Only complete observations were incorporated into the PCA, resulting in 76 observations for BR, 69 observations for TB, and 78 observations for WB. A correlation matrix was applied to the PCA, and components were retained if eigenvalues were greater than 1 (Kaiser Rule).

More traditional analyses, especially parametric ones, could not be performed, due to the spatially dependent nature of the data (Legendre, 1993; Bataineh et al., 2006a). Some researchers, like Bataineh et al. (2006b), have successfully applied traditional statistical analyses in fire ecology studies. However, their sample size was sufficiently large to produce non-compromised results. The logistical and operational constraints placed on our field investigations and the linear nature of the ERT surveys made it difficult to increase the number of observations across a given site. Techniques to identify and eliminate spatial autocorrelation within these datasets, like Moran's I, were considered. However, these techniques would have significantly reduced the effective sample size of observations that would have been useful and appropriate for analysis (Bataineh et al., 2006a).

Some researchers have developed other corrections to permit the continued use of spatially dependent data in statistical analyses. Dale and Fortin (2002) suggest subsampling, adjusting the Type I error rate, partitioning out or factoring in spatial structure, and applying randomization methods to datasets containing spatially dependent observations. In the context of this research, however, subsampling was deemed to be inappropriate considering our relatively small number of complete observations ($n \leq 80$) per site, and adjustment to the Type I error rate was not adopted because it has been criticized for being too conservative (Dale and Fortin, 2002).

3.5 References

Allard, M., Lemay, M., Barrette, C., L'Herault, E., Sarrazin, D. (2012). Permafrost and Climate Change in Nunavik and Nunatsiavut: Importance for Municipal and Transportation Infrastructures. In Nunavik and Nunatsiavut: From Science to Policy. An Integrated Regional Impact Study (IRIS) of Climate Change and Modernization.

Batenipour, H., Alfaro, M., Kurz, D., Graham, J. (2013). Déformations and Ground Temperatures at a Road Embankment in Northern Canada. *Canadian Geotechnical Journal*, 51: 260-271.

Barrett, K., Kasischke, E.S., McGuire, A.D., Turetsky, M.R., Kane, E.S. (2010). Modeling Fire Severity in Black Spruce Stands in the Alaskan Boreal Forest Using Spectral and Non-Spectral Geospatial Data. *Remote Sensing of Environment*, 114: 1494-1503.

Bataineh, A.L., Oswald, B.P., Bataineh, M., Unger, D., Hung, I.-K., Scognamillo, D. (2006a). Spatial Autocorrelation and Pseudoreplication in Fire Ecology. *Fire Ecology*, 2: 107-118.

Bataineh, A.L., Oswald, B.P., Bataineh, M.M., Williams, H.M., Coble, D.W. (2006b). Changes in Understory Vegetation of a Ponderosa Pine Forest in Northern Arizona 30 Years After A Wildfire. *Forest Ecology and Management*, 235: 283-294.

Bean, D., Henry, G., Rolph, S. (2003). CANTTEX Field Manual – Part B – Additional Methods and Experimental Manipulations. *EmanNorth*. Retrieved from https://nwtdiscoveryportal.enr.gov.nt.ca/geoportaldocuments/canttex_field_manual_B_add.pdf.

Beckschäfer, P. (2015). Hemispherical 2.0 – Batch Processing Hemispherical and Canopy Photographs with ImageJ – User Manual. *Georg-August-Universität Göttingen, Germany.* DOI: 10.13140/RG.2.1.3059.4088.

Bell, T., Putt, M., Sheldon, T. (2011). Landscape Hazard Assessment in Nain: Phase I: Inventory of Surficial Sediment Types and Infrastructure Damage, Final Report to Nunatsiavut Government and Nain Inuit Community Government.

Bengtsson, H., Bravo, H.C., Gentleman, R., Hossjer, O., Jaffee, H., Jiang, D., Langfelder, P., Hickey, P., Montgomery, B. (2019). matrixStats: Functions that Apply to Rows and Columns of Matrices (and to Vectors). R package version 0.55.0. https://cran.r-project.org/web/packages/matrixStats/index.html.

Bianchi, S., Cahalan, C., Hale, S., Gibbons, J.M. (2017). Rapid Assessment of Forest Canopy and Light Regime Using Smartphone Hemispherical Photography. *Ecology and Evolution*, 7: 10556-10566.

Blackwell, D.D. and Richards, M. (2004). Geothermal Map of North America, Scale 1:6,500,000, American Association of Petroleum Geologists.

Blok, D., Heijmans, M.M.P.D., Schaepman-Strub, G., Kononov, A.V., Maximov, T.C., Berendse, F. (2010). Shrub Expansion May Reduce Summer Permafrost Thaw in Siberian Tundra. *Global Change Biology*, 16(4): 1296-1305.

Boelter, D.H. (1968). Important Physical Properties of Peat Materials. In Proceedings of the Third International Peat Congress in Quebec, Canada.

Brown, D.R.N., Jorgenson, M.T., Douglas, T.A., Romanovsky, V.E., Kielland, K., Hiemstra, C., Euskirchen, E.S., Ruess, R.W. (2015). Interactive Effects of Wildfire and Climate on Permafrost Degradation in Alaskan Lowland Forests. *Journal of Geophysical Research: Biogeosciences*, 120: 1619-1637.

Brown, J., Ferrians, O., Heginbottom, J.A., Melnikov, E. (2002). Circum-Arctic Map of Permafrost and Ground-Ice Conditions, Version 2. *NSIDC: National Snow and Ice Data Center*.

Buteau, S., Fortier, R., Delisle, G., Allard, M. (2004). Numerical Simulation of the Impacts of Climate Warming on a Permafrost Mound. *Permafrost and Periglacial Processes*, 15: 41-57.

Cable, W.L., Romanovsky, V.E., Jorgenson, M.T. (2016). Scaling-Up Permafrost Thermal Measurements in Western Alaska Using an Ecotype Approach. *The Cryosphere*, 10: 2517-2532.

Caratti, J.F. (2006). Density (DE) Sampling Method. *USDA Forest Service General Technical Report*, RMRS-GTR-164-CD.

Chasmer, L., Quinton, W., Hopkinson, C., Petrone, R., Whittington, P. (2011). Vegetation Canopy and Radiation Controls on Permafrost Plateau Evolution within the Discontinuous Permafrost Zone, Northwest Territories, Canada. *Permafrost and Periglacial Processes*, 22: 199-213.

Dale, M.R.T. and Fortin, M.-J. (2002). Spatial Autocorrelation and Statistical Tests in Ecology. *Ecoscience*, 9(2): 162-167.

Danby, R.K. and Hik, D.S. (2007). Responses of White Spruce (*Picea glauca*) to Experimental Warming at Subarctic Alpine Treeline. *Global Change Biology*, 13: 437-451.

Darrow, M.M. (2011). Thermal Modeling of Roadway Embankments Over Permafrost. *Cold Regions Science and Technology*, 65: 474-487.

Farouki, O. (1981). The Thermal Properties of Soils in Cold Regions. *Cold Regions Science and Technology*, 5: 67-75.

Fortier, R., LeBlanc, A.-M., Allard, M., Buteau, S., Calmels, F. (2008). Internal Structure and Conditions of Permafrost Mounts at Umiujaq in Nunavik, Canada, Inferred from Field Investigation and Electrical Resistivity Tomography. *Canadian Journal of Earth Sciences*, 45: 367-387.

Frazer, G.W., Trofymow, J.A., Lertzman, K.P. (1997). A Method for Estimating Canopy Openness, Effective Leaf Area Index, and Photosynthetically Active Photon Flux Density Using

Hemispherical Photography and Computerized Image Analysis Techniques. Information Report BC-X-373.
French, H.M. (2017). The Periglacial Environment, Fourth Edition. John Wiley and Sons.
Government of Newfoundland and Labrador. (2001a). News Release. Retrieved January 7, 2020, from https://www.releases.gov.nl.ca/releases/2001/forest/0514n05.htm
Government of Newfoundland and Labrador. (2001b). News Release. Retrieved January 7, 2020, from https://www.releases.gov.nl.ca/releases/2001/forest/1015n03.htm
Government of Newfoundland and Labrador. (2019). Forest Fires: Forest Fire Season 2019. Retrieved January 6, 2020, from https://www.faa.gov.nl.ca/forestry/forest_fires/
Hasler, A., Geertsema, M., Foord, V., Gruber, S., Noetzli, J. (2015). The Influence of Surface Characteristics, Topography and Continentality on Mountain Permafrost in British Columbia. *The Cryosphere*, 9: 1025-1038.
Hauck, C., Isaksen, K., Vonder Mühll, D., Sollid, J.L. (2004). Geophysical Surveys Designed to Delineate the Altitudinal Limit of Mountain Permafrost: An Example from Jotunheimen, Norway. *Permafrost and Periglacial Processes*, 15: 191-205.
Heiri, O., Lotter, A.F., Lemcke, G. (2001). Loss On Ignition As a Method for Estimating Organic and Carbonate Content in Sediments: Reproducibility and Comparability of Results. *Journal of Paleolimnology*, 25: 101-110.
Heng, L.K. (2008). Field Estimation of Soil Water Content: A Practical Guide to Methods, Instrumentation and Sensor Technology. *International Atomic Energy Agency*, Training Course Series Number 30.
Hilbich, C., Hauck, C., Hoelzle, M., Scherler, M., Schudel, L., Völksch, I., Vonder Mühll, D., Mäusbacher, R. (2008). Monitoring Mountain Permafrost Evolution Using Electrical Resistivity Tomography: A 7-Year Study of Seasonal, Annual, and Long-Term Variations at Schilthorn, Swiss Alps. *Journal of Geophysical Research*, 113: F01S90.
Hilbich, C., Marescot, L., Hauck, C., Loke, M.H., Mäusbacher, R. (2009). Applicability of Electrical Resistivity Tomography Monitoring to Coarse Blocky and Ice-Rich Permafrost Landforms. *Permafrost and Periglacial Processes*, 20: 269-284.
Holloway, J.E., Lewkowicz, A.G., Douglas, T.A., Li, X., Turetsky, M.R., Baltzer, J.L., Jin, H. (2020). Impact of Wildfire on Permafrost Landscapes: A Review of Recent Advances and Future Prospects. *Permafrost and Periglacial Processes*, DOI: 10.1002/ppp.2048.
Hope, E.S., McKenney, D.W., Pedlar, J.H., Stocks, B.J., Gauthier, S. (2016). Wildfire Suppression Costs for Canada Under a Changing Climate. *PLoS ONE*, 11(8): e0157425.
Instanes, A. (2016). Incorporating Climate Warming Scenarios in Coastal Permafrost Engineering Design – Case Studies from Svalbard and Northwest Russia. *Cold Regions Science and Technology*, 131: 76-87.
Isaksen, K., Hauck, C., Gudevang, E., Odegard, R.S., Sollid, J.L. (2002). Mountain Permafrost Distribution in Dovrefjell and Jotunheimen, Southern Norway, Based on BTS and DC Resistivity Tomography Data. *Norwegian Journal of Geography*, 56: 122-136.
Jafarov, E.E., Romanovsky, V.E., Genet, E., McGuire, A.D., Marchenko, S.S. (2013). The Effects of Fire on the Thermal Stability of Permafrost in Lowland and Upland Black Spruce Forests of Interior Alaska in a Changing Climate. *Environmental Research Letters*, 8: 035030.
Jarčuška, B. (2008). Methodological Overview to Hemispherical Photography, Demonstrated on an Example of the Software GLA. *Folia Oecologica*, 35: 66-69.

Johansen, O. (1975). Thermal Conductivity of Soils, Ph.D. Thesis. Trondheim, Norway. (Available as USACRREL Draft Translation 637, 1977).

Johnston, G.H. (Ed). (1981). Permafrost: Engineering Design and Construction. John Wiley and Sons.

Karunaratne, K.C. and Burn, C.R. (2003). Freezing N-Factors in Discontinuous Permafrost Terrain, Takhini River, Yukon Territory, Canada. In Proceedings of the Eighth International Conference on Permafrost, in Zurich, Switzerland.

Karunaratne, K.C. and Burn, C.R. (2004). Relations Between Air and Surface Temperature in Discontinuous Permafrost Terrain Near Mayo, Yukon Territory. *Canadian Journal of Earth Sciences*, 41: 1437-1451.

Kasischke, E.S. and Johnstone, J.F. (2005). Variation in Postfire Organic Layer Thickness in a Black Spruce Forest Complex in Interior Alaska and its Effects on Soil Temperature and Moisture. *Canadian Journal of Forest Research*, 35: 2164-2177.

Klene, A.E., Nelson, F.E., Shiklomanov, N.I., Hinkel, K.M. (2001). The N-Factor in Natural Landscapes: Variability of Air and Soil-Surface Temperatures, Kuparuk River Basin, Alaska, U.S.A. *Arctic, Antarctic, and Alpine Research*, 33(2): 140-148.

Kneisel, C., Hauck, C., Fortier, R., Moorman, B. (2008). Advances in Geophysical Methods for Permafrost Investigations. *Permafrost and Periglacial Processes*, 19: 157-178.

Kokelj, S.V., Riseborough, D., Coutts, R., Kanigan, J.C.N. (2013). Permafrost and Terrain Conditions at Northern Drilling-Mud Sumps: Impacts of Vegetation and Climate Change and the Management Implications. *Cold Regions Science and Technology*, 64: 46-56.

Legendre, P. (1993). Spatial Autocorrelation: Trouble or New Paradigm? *Ecology*, 74(6): 1659-1673.

Lévesque, R., Allard, M., Seguin, M.K., Pilon, J. (1990). Données préliminaires sur le régime thermique du pergélisol dans quelques localités du Nunavik, Québec. In Proceedings of the Fifth Canadian Permafrost Conference, Québec, Canada.

Lewkowicz, A.G. (2008). Evaluation of Miniature Temperature-Loggers to Monitor Snowpack Evolution at Mountain Permafrost Sites, Northwestern Canada. *Permafrost and Periglacial Processes*, 19: 323-331.

Lewkowicz, A.G. and Way, R.G. (2014). Overview Report for Nunatsiavut Government on Permafrost Conditions in the Nain Area. DOI: 10.13140/RG.2.1.1910.0240.

Lewkowicz, A.G., Etzelmüller, B., Smith, S. (2011). Characteristics of Discontinuous Permafrost based on Ground Temperature Measurements and Electrical Resistivity Tomography, Southern Yukon, Canada. *Permafrost and Periglacial Processes*, 22: 320-342.

Loke, M.H., Acworth, I., Dahlin, T. (2003). A Comparison of Smooth and Blocky Inversion Methods in 2D Electrical Imaging Surveys. *Exploration Geophysics*, 34: 182-187.

Lundquist, J.D., Dickerson-Lange, S.E., Lutz, J.A., Cristea, N.C. (2013). Lower Forest Density Enhances Snow Retention in Regions with Warmer Winters: A Global Framework Developed from Plot-Scale Observations and Modeling. *Water Resources Research*, 49: 6356-6370.

Majorowicz, J.A. and Minea, V. (2012). Geothermal Energy Potential in the St. Lawrence River Area Quebec. *Geothermics*, 43: 25-36.

Majorowicz, J.A. and Minea, V. (2015). Shallow and Deep Geothermal Energy Potential in low Heat Flow/Cold Climate Environment: Northern Quebec, Canada, Case Study. *Environmental Earth Sciences*, 74(6): 5233-5244.

Mareschal, J.C., Poirier, A., Rolandone, F., Bienfait, G., Gariepy, C., Lapointe, R., Jaupart, C. (2000). Low Mantle Heat Flow at the Edge of the North American Continent, Voisey Bay, Labrador. *Geophysical Research Letters*, 27(6): 823-826.

McClymont, A.F., Hayashi, M., Bentley, L.R., Christensen, B.S. (2013). Geophysical Imaging and Thermal Modeling of Subsurface Morphology and Thaw Evolution of Discontinuous Permafrost. *Journal of Geophysical Research: Each Surface*, 118: 1826-1837.

Miranda, B.R., Sturtevant, B.R., Schmelzer, I., Doyon, F., Wolter, P. (2016). Vegetation Recovery Following Fire and Harvest Disturbance in Central Labrador – A Landscape Perspective. *Canadian Journal of Forest Research*, 46: 1009-1018.

Nobis, M. and Hunziker, U. (2005). Automatic Thresholding for Hemispherical Canopy-Photographs Based on Edge Detection. *Agricultural and Forest Meteorology*, 128; 243-250.

Payette, S., Delwaide, A., Caccianiga, M., Beauchemin, M. (2004). Accelerated Thawing of Subarctic Peatland Permafrost Over the Last 50 Years. *Geophysical Research Letters*, 31: L18208.

Perreault, P. and Shur, Y. (2016). Seasonal Thermal Insulation to Mitigate Climate Change Impacts on Foundations in Permafrost Regions. *Cold Regions Science and Technology*, 132: 7-18.

Pollard, W.H. and French, H.M. (1980). A First Approximation of the Volume of Ground Ice, Richards Island, Pleistocene Mackenzie Delta, Northwest Territories, Canada. *Canadian Geotechnical Journal*, 17: 509-516.

Pomeroy, J.W., Parviainen, J., Hedstrom, N., Gray, D.M. (1998). Coupled Modelling of Forest Snow Interception and Sublimation. *Hydrological Processes*, 12: 2317-2337.

Rasband, W.S. (2014). ImageJ. US National Institutes of Health. Retrieved from http://imagej.nih.gov/ij/.

Revuelto, J., López-Moreno, J.I., Azorin-Molina, C., Vicente-Serrano, S.M. (2015). Canopy Influence on Snow Depth Distribution in a Pine Stand Determined from Terrestrial Laser Data. *Water Resources Research*, 51: 3476-3489.

Rohde, R., Muller, R.A., Jacobsen, R., Muller, E., Perlmutter, S., Rosenfeld, A., Wurtele, J., Groom, D., Wickham, C. (2013). A New Estimate of the Average Earth Surface Land Temperature Spanning 1753 to 2011. *Geoinformation Geostatistics: An Overview*, 1:1.

Shur, Y.L. and Jorgenson, M.T. (2007). Patterns of Permafrost Formation and Degradation in Relation to Climate and Ecosystems. *Permafrost and Periglacial Processes*, 18: 7-19.

Smith, M.W. and Riseborough, D.W. (2002). Climate and the Limits of Permafrost. *Permafrost and Periglacial Processes*, 13: 1-15.

Smith, S. and Riseborough, D.W. (2010). Modelling the Thermal Response of Permafrost Terrain to Right-Of-Way Disturbance and Climate Warming. *Cold Regions Science and Technology*, 60: 92-103.

Spaans, E.J.A. and Baker, J.M. (1996). The Soil Freezing Characteristic: Its Measurement and Similarity to the Soil Moisture Characteristic. *Soil Science Society of America Journal*, 60: 13-19.

Stewart, A.M., Edmisten, K.L., Wells, R., Collins, G.D. (2007). Measuring Canopy Coverage with Digital Imaging. *Communications in Soil Science and Plant Analysis*, 38: 895-902.

Sturm, M., McFadden, J.P., Liston, G.E., Chapin III., F.S., Racine, C.H., Holmgren, J. (2001). Snow-Shrub Interactions in Arctic Tundra: A Hypothesis with Climatic Implications. *Journal of Climate*, 14: 336-344.

Taylor, A.E. (1995). Field Measurements of N-Factors for Natural Forest Areas, Mackenzie Valley, Northwest Territories. *Geological Survey of Canada,* Current Research 1995-B.

Treat, C.C., Wisser, D., Marchenko, S., Frolking, S. (2013). Modelling the Effects of Climate Change and Disturbance on Permafrost Stability in Northern Organic Soils. *Mires and Peat*, 12: 1-17.

van Everdingen, R. (2005). Multi-Language Glossary of Permafrost and Related Ground-Ice Terms. International Permafrost Association.

van Vuuren, D.P., Edmonds, J., Kainuma, M., Riahi, K., Thomson, A., Hibbard, K., Hurtt, G.C., Kram, T., Krey, V., Lamarque, J.-F., Masui, T., Meinshausen, M., Nakicenovic, N., Smith, S.J., Rose, S.K. (2011). The Representative Concentration Pathways: An Overview. *Climatic Change*, 109: 5-31.

Varhola, A., Coops, N.C., Weiler, M., Moore, R.D. (2010). Forest Canopy Effects on Snow Accumulation and Ablation: An Integrative Review of Empirical Results. *Journal of Hydrology*, 392: 219-233.

Way, R.G. and Lewkowicz, A.G. (2015). Investigations of Discontinuous Permafrost in Coastal Labrador with DC Electrical Resistivity Tomography. In Proceedings of GeoQuébec 2015.

Way, R.G. and Lewkowicz, A.G. (2016). Modelling the Spatial Distribution of Permafrost in Labrador-Ungava Using the Temperature at the Top of Permafrost. *Canadian Journal of Earth Sciences*, 53: 1010-1028.

Way, R.G. and Viau, A.E. (2015). Natural and Forced Air Temperature Variability in the Labrador Region of Canada During the Past Century. *Theoretical and Applied Climatology*, 121(5): 413-424.

Way, R.G., Lewkowicz, A.G., Zhang, Y. (2018). Characteristics and Fate of Isolated Permafrost Patches in Coastal Labrador, Canada. *The Cryosphere*, 12: 2667-2688.

Wilcox, E.J., Keim, D., de Jong, T., Walker, B., Sonnentag, O., Sniderhan, A.E., Mann, P., Marsh, P. (2019). Tundra Shrub Expansion May Amplify Permafrost Thaw by Advancing Snowmelt Timing. *Arctic Science*, 5: 202-217.

Williams, T.G. and Flanagan, L.B. (1998). Measuring and Modelling Environmental Influences on Photosynthetic Gas Exchange in Sphagnum and Pleurozium. *Plant, Cell and Environment*, 21: 555-564.

Williams, P.J. and Smith, M.W. (1989). The Frozen Earth, Fundamentals of Geocryology. Cambridge University Press.

Yi, S., McGuire, A.D., Kasischke, E., Harden, J., Manies, K., Mack, M., Turetsky, M. (2010). A Dynamic Organic Soil Biogeochemical Model for Simulating the Effects of Wildfire on Soil Environmental Conditions and Carbon Dynamics of Black Spruce Forests. *Journal of Geophysical Research*, 115: G04015.

Zhang, Y., Wolfe, S.A., Morse, P.D., Olthof, I., Fraser, R.H. (2015). Spatiotemporal Impacts of Wildfire and Climate Warming on Permafrost Across a Subarctic Region, Canada. *Journal of Geophysical Research: Earth Surface*, 120: 2338-2356.

Zoltai, S.C. (1972). Palsas and Peat Plateaus in Central Manitoba and Saskatchewan. *Canadian Journal of Forest Research*, 2: 291-302.

CHAPTER 4 : FIELD OBSERVATIONS OF POST-FIRE FROZEN GROUND, VEGETATION, AND SNOW CONDITIONS NEAR NAIN AND POSTVILLE, NUNATSIAVUT

Authors: Wang, Y.[1], Lewkowicz, A.G.[1], Hermanutz, L.[2], Way, R.G.[3]

Affiliations:

[1]Department of Geography, Environment and Geomatics, University of Ottawa

[2]Department of Biology, Memorial University

[3]Department of Geography and Planning, Queen's University

Authorship Attestation:

I am the primary author of this manuscript. The plan for field data collection was established by Dr. Antoni Lewkowicz, Dr. Luise Hermanutz, Dr. Robert Way, and myself. I collected the field data during the summer 2018, winter 2019, and summer 2019 field seasons, with the assistance of and in collaboration with other members of the Food, Fire, and Ice research team. Previous field observations from summer 2017 and winter 2018 were collected by other members of the Food, Fire, and Ice team. I also collected soil samples in summer 2018 and 2019, and laboratory-based analyses were completed during the following fall semester. I performed the exploratory and statistical analyses in R. This contribution was generated with guidance from Dr. Antoni Lewkowicz, Dr. Luise Hermanutz, and Dr. Robert Way.

4.1 Abstract

The impacts of fire on permafrost are poorly known for forests in coastal Labrador, which are characterized by some of the longest fire intervals and wettest climates of the North American boreal region. We present summer and winter field observations of frozen ground, vegetation, and snow conditions approximately two decades after fire at three sites in the sporadic discontinuous permafrost zone. Burned and unburned sections of our sites differ in terms of snow depth, near-surface electrical resistivity, soil moisture, total canopy cover, and shrub density, but differences are not consistent at all three sites. Permafrost appears to have persisted beneath the unburned forest at two sites located at 56.7°N near Nain, due to ecological protection offered by the intact forest canopy. No near-surface frozen ground was detected in the fire-affected portions of these sites. The third site, located at 54.8°N near Postville, exhibits only seasonally frozen ground. Post-fire shrub establishment at all three sites is promoted by an increase in soil temperature and a lack of competing vegetation. However, the impact of these shrubs on frozen ground conditions is limited because seasonal snowpacks are much deeper and longer lasting in both burned and unburned areas at our sites than in the boreal forests of western North America.

Key Words: Forest Fire, Boreal, Permafrost, Shrub Regeneration, Snow Accumulation, Forest Canopy, Nunatsiavut, Labrador, Canada.

4.2 Introduction

Fires are the largest natural surface disturbance to the North American boreal forest (Hanes et al., 2018). Fire is a natural phenomenon that leads to renewal and regeneration of the forest, but recent climatic warming has caused an increase in its frequency and intensity across northern landscapes (Flannigan et al., 2005; Balshi et al., 2009; Wotton et al., 2010). Following fire, forests undergo succession, with progressive stages of vegetation establishment and abundance that drive the response of the thermal regime of underlying frozen ground (Shur and Jorgenson, 2007; Jorgenson et al., 2010). Post-fire increases in soil temperature, soil moisture (Fisher et al., 2016), and snow depth (Burles and Boon, 2011; Gleason et al., 2013) have been linked to active layer thickening and permafrost thaw (Burn, 1998; Smith et al., 2015; Holloway et al., 2020). These observations are geographically concentrated in the western North American boreal forest (Holloway et al., 2020), and comparable studies have not yet been undertaken in the coastal forests of the eastern Canadian subarctic where the climate and other conditions are substantially different.

This study examines post-fire forest and frozen ground conditions at three burned sites in Nunatsiavut, two near the community of Nain and the third near Postville (Figure 4-1). Based on studies conducted in western North America (e.g., Burn, 1998; Nossov et al., 2013; Smith et al., 2015; Brown et al., 2016), we hypothesized that ground temperatures would be lower in undisturbed forest than in adjacent burned areas, due to greater interception of snow, a thick undisturbed organic mat, and greater ground shading. Burned areas were expected to have thinner organic mats due to combustion, and higher ground temperatures were expected to promote shrub growth, leading to snow-trapping and overall greater snow depths in winter. Permafrost, if present, was expected to be located beneath the unburned forest and absent or degrading in burned areas. Our research provides a description of both summer and winter post-fire site conditions and permits inter- and intra-site comparisons for the three forest fire sites.

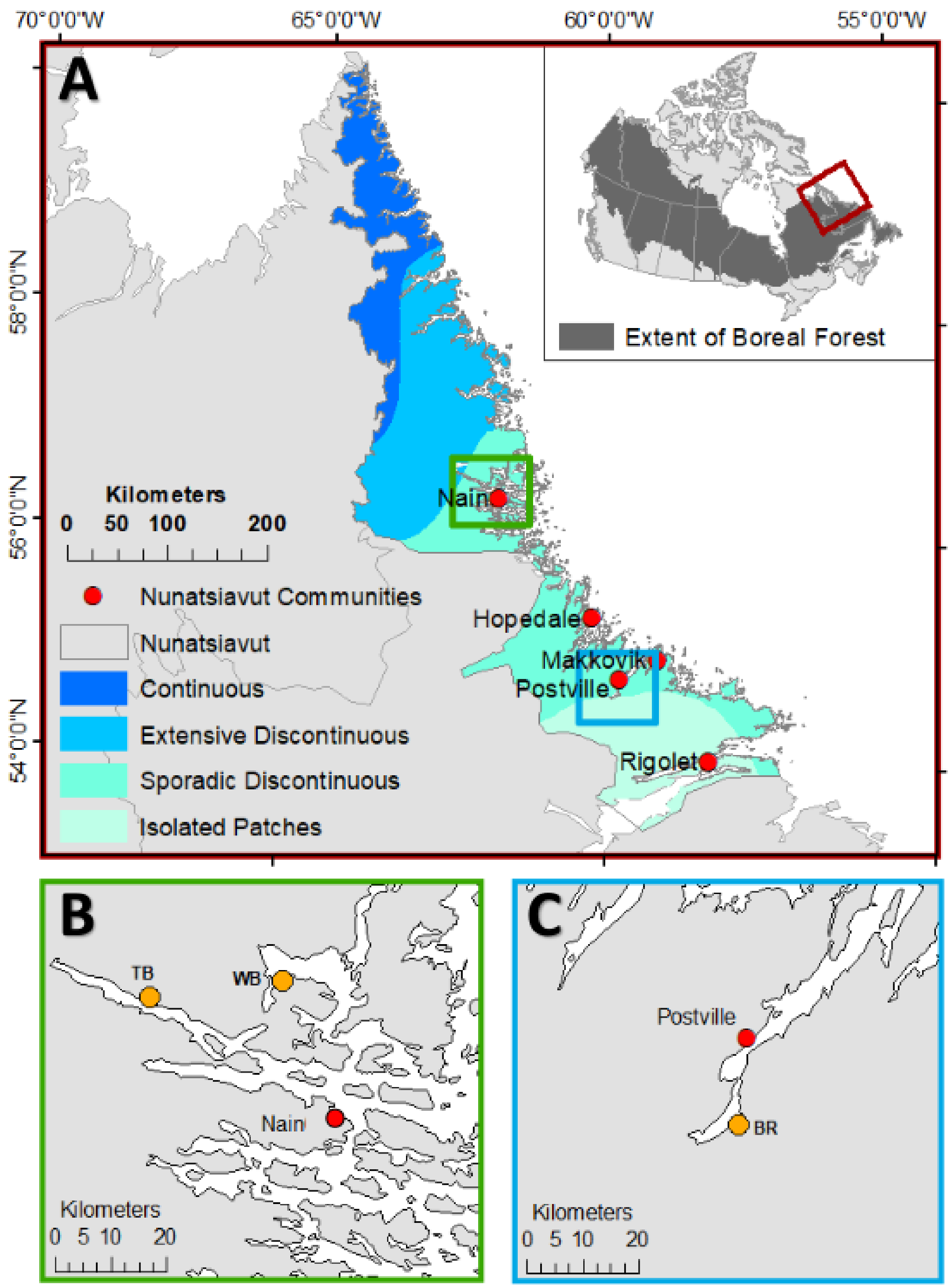

Figure 4-1. Location of Study Sites near Nain and Postville, Nunatsiavut (Crown-Indigenous Relations and Northern Affairs Canada, 2007). (A) Nunatsiavut communities and permafrost zones (Brown et al., 2002); inset shows the location of main map in relation to the Canadian boreal forest (Brandt, 2009); (B) Tikkoatokak Bay (TB) and Webb Bay (WB) fire sites near Nain; (C) Beaver River (BR) fire site near Postville.

4.3 Study Region and Sites

The regional climate of coastal Labrador is strongly influenced by its proximity to the cold Labrador Current, which runs southwards along the Atlantic coast (Banfield and Jacobs, 1998; Roberts et al., 2006). Winters are long and cold, and summers are short and cool throughout the region (Hare, 1950; Banfield and Jacobs, 1998). The mean annual air temperature at Nain (56.5°N; Figure 4-1-A) is -2.5°C (1981-2010), while mean annual precipitation is 925.5 mm, divided into 450.2 mm of rain and 475.3 cm of snow (Environment Canada, 2020). Mean annual air temperature rises southwards to -1.3°C (1981-2010) at Makkovik (55°N; Figure 4-1-A), with similar amounts of precipitation (978.5 mm; Environment Canada, 2020).

The region is part of the Canadian Shield, and the terrain is characterized by thin layers of frost-susceptible surficial deposits over bedrock (Bell et al., 2011). According to the Permafrost Map of Canada (Heginbottom et al., 1995; Figure 4-1-A), Nain and Postville are both located within the sporadic discontinuous permafrost zone, so 10 to 50% of the area around these communities is expected to be underlain by permafrost. A recent regional analysis using the Temperature at the Top of Permafrost model over 10 km grid cells showed the Postville area to be located in the isolated patches zone (Way and Lewkowicz, 2016), implying that less permafrost is expected there than around Nain.

Labrador's forests are comprised of black spruce (*Picea mariana* [Mill.] B.S.P.), white spruce (*Picea glauca* [Moench] Voss), balsam fir (*Abies balsamea* [L.] Mill.), and eastern larch (*Larix laricina* [Du Roi] K. Koch) (Roberts et al., 2006). Near Postville, the forest is dominated by black spruce with some balsam fir, while all four major coniferous species are present near Nain. The regional fire interval is much longer than elsewhere in the North American boreal forest due to the cool and wet climate (Foster, 1983; Coops et al., 2018, Hanes et al., 2018). Adaptations, including semi-serotinous cones, allow for rapid post-fire seed release by some coniferous species (e.g., black spruce), but the long-term accumulation of organic matter associated with the low fire frequency means that a favourable seed bed may not be present (Foster, 1983; Elson et al., 2007). Low post-fire tree regeneration rates have been reported in northern Québec (Sirois and Payette, 1991; Payette et al., 2001) where shrub development is favoured over tree establishment (Lévesque et al., 2012). Slow reforestation provides an extended opportunity for understory development (Foster, 1985; Brehaut and Brown, 2020), so that densities of some ericaceous species rapidly approach, or even exceed, those measured prior to fire (Foster, 1985).

Two sites are located about 25 km from Nain, along the northern edge of Tikkoatokak Bay (TB; 56° 42.275' N, 62° 12.555' W) and the southern edge of Webb Bay (WB; 56° 45.379' N, 61° 52.178' W). These two fires covered areas of 3 km^2 and 1 km^2 in the summers of 2001 and 2004, respectively. At TB and WB, the surficial materials mainly consist of sand, with slightly more silt at TB. Erratics are evident at both TB and WB, and bedrock outcrops are also present in places at TB.

The Beaver River site (BR; 54˚ 46.828' N, 59˚ 48.489' W) is located about 15 km southwest of Postville, along the southern shore of the innermost segment of Kaipokok Bay. The BR fire occurred in summer 1996, when it burned approximately 150 km^2 of black spruce-dominated forest. Surficial materials consist of a mixture of silt and fine sand, with some clay and scattered erratics.

4.4 Methods

4.4.1 Site Set-Up and Climate

Field investigations were conducted in 2017, 2018, and 2019. Two primary parallel transects spaced 60 to 100 m apart, each measuring 80 m at the TB and WB sites (Figure 4-2-A) and 40 m at the BR site, were established perpendicularly to the unburned forest edge. Vegetation data was collected along parallel, untrampled secondary transects, offset 1 m downslope from each primary transect. At the BR site, additional field measurements and observations were made along a supplementary 50 m-long transect.

Air temperature (±0.21°C accuracy) was measured at 2-hour intervals for two years from August 2017 to August 2019 at TB, two years from July 2017 to July 2019 at WB, and one year from July 2018 to July 2019 at BR (Table 4-1). Hobo Pro v2 Temperature/Relative Humidity U23-001 Data Loggers (Onset) were installed in radiation shields within unburned forest stands at each of the sites (Figure 4-2-B).

Table 4-1. Summary of Mean Annual Air Temperature, Mean January and July Air Temperatures, and Thawing and Freezing Indices for the Study Sites (2017-2019) and the Nain A Environment Canada Climate Station (2017-2019 and 1981-2010 normal).

	1981-2010	2017-2018			2018-2019			
Site	Nain A	Nain A[a]	TB[b]	WB[c]	Nain A[a]	TB[d]	WB[e]	BR[f]
Mean Annual Air Temperature (°C)	-2.5	-	-2.4	-2.5	-	-3.0	-3.1	-1.9
Mean January Temperature (°C)	-17.6	-17.4	-18.4	-17.7	-18.8	-19.7	-20.1	-18.8
Mean July Temperature (°C)[g]	10.1	-	11.3	11.1	7.9	9.5	-	-
Thawing Index (degree days)	1188	-	1221	1166	-	1132	1111	1429
Freezing Index (degree days)	2072	-	2112	2083	-	2214	2246	2131

[a] due to missing station data for Nain A, certain values could not be calculated.
[b] for full calendar year from August 11, 2017 to August 10, 2018.
[c] for full calendar year from July 20, 2017 to July 19, 2018.
[d] for full calendar year from August 11, 2018 to August 10, 2019.
[e] for full calendar year from July 20, 2018 to July 19, 2019.
[f] for full calendar year from July 21, 2018 to July 20, 2019.
[g] due to the timing of the site visits, the mean July temperature for 2019 could not be calculated for the WB or BR sites.

Seasonal snow accumulation and melt dynamics were derived from a series of vertically arranged Thermochron iButtons (Maxim), installed on stakes that were placed in both the burned and unburned regions (Figure 4-2-BC). The iButtons were placed at 10 cm intervals from the ground surface to 60 cm and at 20 cm intervals from 60 cm to a maximum height of 140 cm at TB and WB and 160 cm at BR. Snow accumulation and melt patterns were interpreted by examining temperatures recorded at a resolution of 0.5°C and an accuracy of ±1°C every 4 hours by each sensor (Isaksen et al., 2002; Danby and Hik, 2007; Lewkowicz, 2008). Maximum seasonal snow depth and the duration of the snow-on-ground seasons were calculated.

The spatial variation in snow depths was examined during winter site visits on March 23-24, 2018 (TB and WB) and February 18-19, 2019 (BR). Snow depths were measured at 1 m intervals along the primary transects with a 230 cm-long avalanche probe. These snow depths can be used for intra-site comparisons between burned and unburned sections. Inter-site comparisons can also be made for the TB and WB sites since measurements were taken only a few days apart. In relation to the seasonal snow dynamics, these snow depths were measured on dates from 55% (BR) to 60% (TB and WB) of the way through the snow-on-ground season and at 80 to 100% of the maximum seasonal snow depths.

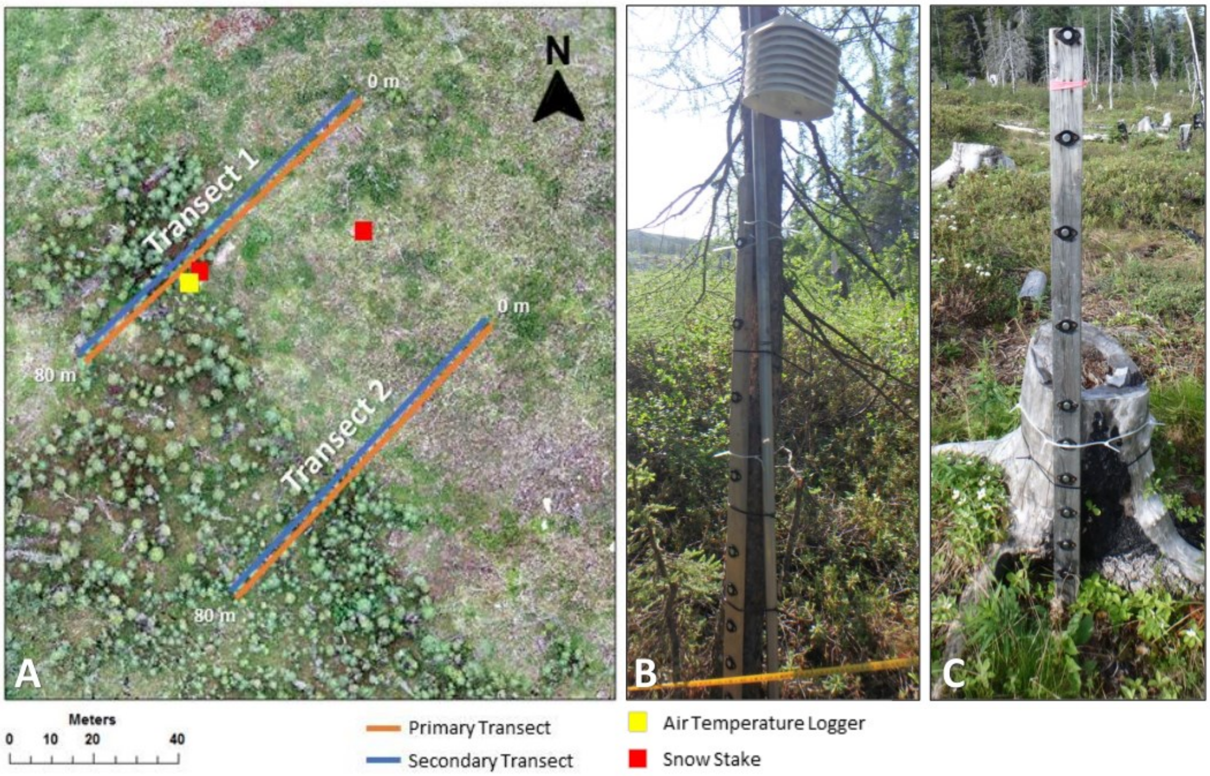

Figure 4-2. (A) Position of Transects and Instrumentation on a UAV image of WB. Transects are perpendicular to the edge of the unburned forest. Primary transects, for ground and snow conditions, are shown in orange. Secondary transects, for vegetation conditions, are located 1 m downslope of the primary transects; (B) An air temperature logger is positioned in the unburned forest; (B-C) Snow stakes, equipped with arrays of iButton temperature loggers for inferring snow depths and dynamics, are positioned in both the burned and unburned areas of the site.

4.4.2 Frozen Ground and Soil Properties

Frozen ground conditions were assessed along the primary transects using electrical resistivity tomography (ERT), supported by frost probing and instantaneous temperature monitoring (Way and Lewkowicz, 2015). Direct current ERT is a geophysical technique that can be used to delimit frozen and unfrozen ground based on electrical contrasts between the solid and liquid states of water (Fortier et al., 2008; Kneisel et al., 2008; Lewkowicz et al., 2011). The Wenner electrode configuration was applied, due to its stability in heterogeneous regions and its ability to delineate horizontal structures, such as the top and base of permafrost (Hauck et al., 2004; Fortier et al., 2008). Aluminum electrodes (50 cm long and 1 cm in diameter) were inserted into the ground at minimum intervals of 1 m. The electrodes were connected by jumper cables to take-outs, which were connected to an ABEM Terrameter LS profiling system. Apparent resistivities were processed and converted to best-estimate values using the robust inversion method in the two-dimensional RES2DINV inversion software (Loke et al., 2003), which applies a Gauss-Newton algorithm to fit an appropriate subsurface model to the observations (Kneisel et al., 2008; Hilbich et al., 2009). Inversion iterations were permitted until convergence had occurred, marked by a change in the root mean square error between consecutive iterations of less than 5%, or until the fifth iteration, whichever came first. Topography and breaks in slope along the ERT lines were recorded with a clinometer, and topographic corrections were applied during the inversion process. Depths of investigation of approximately 12 and 6 m were obtained with the 80 and 40 m surveys, respectively. Near-surface resistivity values, corresponding to the average resistivity over a depth of 0.5 to 1.05 m below the ground surface, were extracted from the processed inversions and assigned to the nearest metre along the profile. The marine limit near Nain is 44 m a.s.l. (Johnson, 1969), so the upper sediment layers at the study sites have likely been marine-affected. No information is available on porewater salinities, but these are expected to be low due to the low salinity of the adjacent Labrador Sea and the high regional precipitation rates that would have permitted leaching of salts whenever permafrost was absent during the Holocene.

Organic layer thicknesses were measured at 1 m intervals along the ERT lines by inserting a 50 cm-long aluminum rod to the depth where the mineral soil resisted penetration. Small pits were dug to the top of the mineral soil in several locations at each site to verify the organic layer thickness estimates.

Soil temperature (±1.5°C accuracy) and volumetric moisture content (±0.03 cm^3/cm^3 accuracy) were recorded with a WET Sensor and HH2 Moisture Meter Version 2.3 (Delta-T) at 1 m intervals at the BR site and at 2 m intervals at the TB and WB sites between the ERT lines and the parallel vegetation transects. The soil temperature and moisture values were each calculated as the average of three measurements. These data are useful for evaluating spatial variations in intra-site soil temperature and moisture at the time of measurement.

4.4.3 Vegetation Characteristics

Total canopy cover, understory canopy cover, and shrub height and density were measured along the secondary transects.

Hemispherical images were obtained at 1 m intervals from the ground surface to evaluate total canopy cover. Additional hemispherical images were obtained at a shoulder height of 1.3 m. The canopy coverage from each image collected at shoulder height was subtracted from the total canopy coverage at the same location to determine the understory coverage, which was primarily attributed to shrubs. Some calculations of understory canopy coverage produced negative values, reflecting the complexity of the layered and branched nature of shrubs and trees. This occurred at locations where coverage by vegetation immediately above the lens was exaggerated in the hemispherical images. These values were not excluded from the exploratory data analysis. Images were collected with a levelled Samsung Galaxy A5 smartphone with an attachable fisheye lens (Lifetrons Travel Lens Set), mounted on a selfie stick to ensure that the camera operator was not captured in the image. Canopy openness and gap light transmission were estimated by automatic thresholding and binary conversion, followed by pixel counts in the ImageJ software (Rasband, 2014).

The number of shrub stems and the height of the tallest shrubs of each species were measured within a 0.25 m^2 plot at 1 m intervals along the secondary transects. Common shrub species included Labrador tea (*Rhododendron groenlandicum* [Oeder] Kron and Judd), dwarf birch (*Betula glandulosa* Mich.), tea-leaf willow (*Salix planifolia* Pursh), gray-leaf willow (*Salix glauca* L.), and green alder (*Alnus viridis* subsp. *crispa* [Aiton] Turr.). Shrubs under 25 cm were omitted, including shorter or prostrate species like crowberry (*Empetrum nigrum* L.) or blueberry (*Vaccinium* spp.), as they were expected to have limited snow-trapping and ground-shading abilities.

4.4.4 Exploratory Data and Statistical Analyses

Principal component analysis (PCA) was performed to reduce the dimensionality of eight numerical variables collected along the transects: snow depth, near-surface resistivity, organic layer thickness, soil temperature (average of three samples), soil moisture (average of three samples), total canopy cover, maximum shrub height, and shrub density. Through PCA, it was possible to identify intra-site associations between these variables. Of a total of 458 observations, only complete observations, in which data for all eight variables were present, were incorporated into the PCA. This resulted in a total of 223 observations, with 69, 78, and 76 observations for the TB, WB, and BR sites, respectively. A correlation matrix was applied to the PCA to account for the range of scales used for variable measurements. Principal components (PC) were retained according to the Kaiser Rule, requiring eigenvalues above 1. Variables whose loadings exceeded 0.4 were retained for interpretation. Exploratory data and statistical analyses were performed in R, and figures were generated using the ggplot2 (Wickham, 2016), ggbiplot (Vu, 2011), and cowplot (Wilke, 2019) packages.

4.5 Results

4.5.1 Climate

For 2017-2018, the TB and WB sites experienced mean annual air temperatures of -2.4°C and -2.5°C, respectively. These values are similar to the mean annual air temperature of -2.5°C for Nain (1981-2010; Table 4-1). The following year was slightly cooler, with mean annual air temperatures of -3.0°C at TB and -3.1°C at WB and lower mean January temperatures of -19.7°C and -20.1°C, respectively. Due to missing station data from Nain, direct comparisons can only be made for January 2018 and 2019, which were up to 1.3°C warmer at Nain than at the TB and WB sites, and July 2019, which was more than 1°C cooler at Nain than at TB. Based on the site records, the TB and WB sites experience similar air temperatures, which are slightly more continental (colder in winter and warmer in summer) than at Nain (Figure 4-1-B). Temperatures during the study years were not abnormal relative to the long-term means. The BR site exhibited the largest thawing index and the smallest freezing index, resulting in a mean annual air temperature of -1.9°C for 2018-2019 and the highest January 2019 temperature of the three sites. At the time of field investigations, there were no nearby government-established stations available for comparison.

Snow cover persisted at the study sites from October to May, and sometimes into June, for at least 200 days of each year (Figure 4-3). At TB and WB, much of the development of the 2017-2018 seasonal snowpack was attributed to major snowfall in mid-December 2017. In 2018-2019, the snowpack began to develop at these two sites two weeks earlier than in the previous year, but major snowfall did not occur until early February. During both winters of study, the snowpack was deeper at WB than at TB. At BR, the 2018-2019 seasonal snowpack accumulated more gradually throughout the season, when compared with the more northern sites. At all sites, snowpack ablation in spring took two to four weeks.

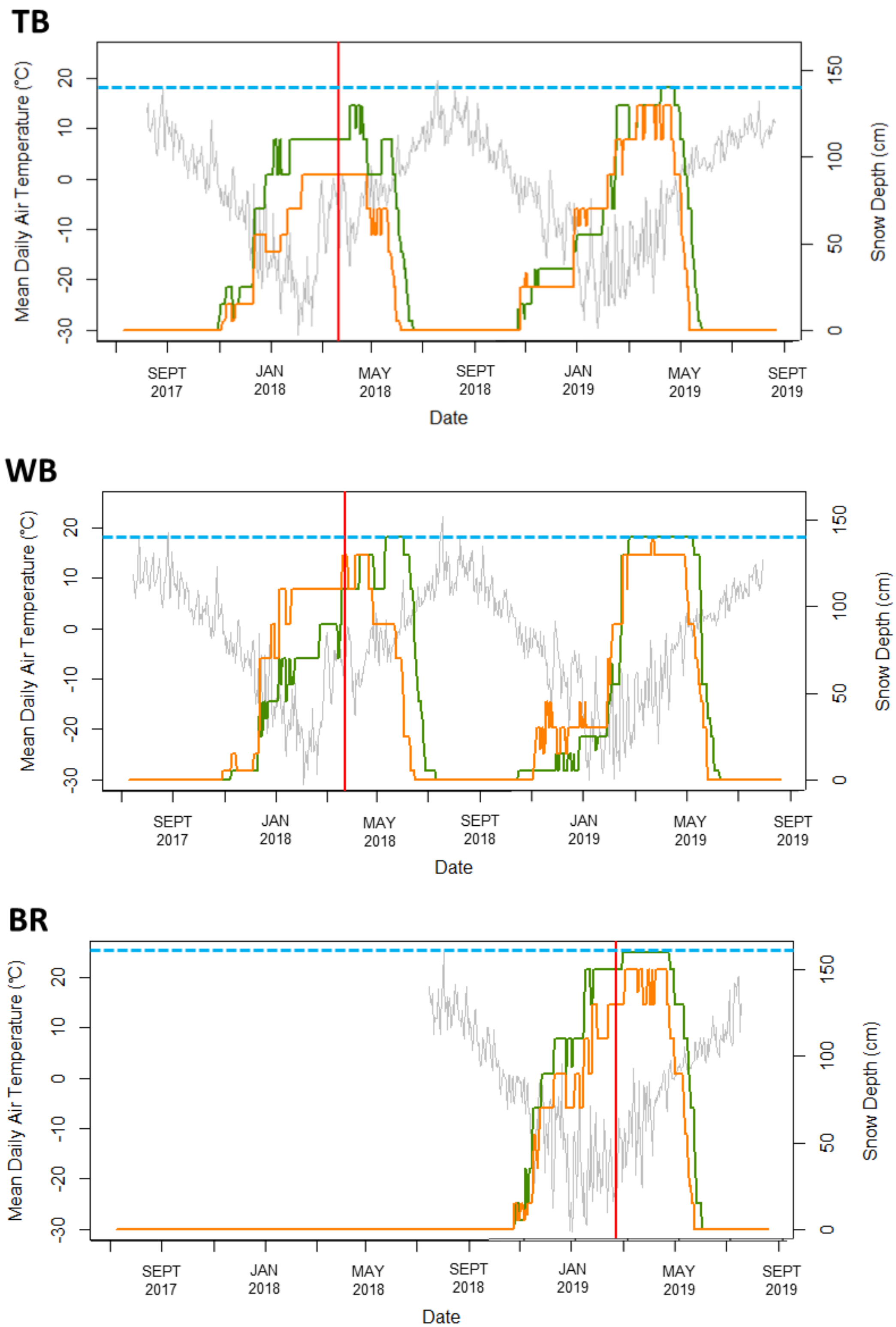

Figure 4-3. Mean Daily Air Temperatures (gray) and Snow Depths in Burned (orange) and Unburned (green) Areas at the TB, WB, and BR Sites for 2017-2019. The date corresponding to transect-based snow depth measurements at each of the sites is identified by a red line. The maximum detection limit of 140 cm at TB and WB and 160 cm at BR is identified by a blue dotted line.

The seasonal snow accumulation and melt patterns showed greater maximum snow depths at our snow stakes in the unburned forest, relative to the burned areas. The duration of the snow-on-ground season was, on average, two weeks longer in the undisturbed forest than in the burned region, due to greater snow depths and later and slower melt. Consequently, snow depth days, which incorporate both the depth and duration of the snowpack, were greater in the unburned forest than the burned region by at least 11% at TB, 3% at WB, and 21% at BR for the 2018-2019 season (Table 4-2). Frequent fluctuations in depth occurred in both burned and unburned snowpacks throughout the season, suggesting minor melt and possible snow redistribution events.

Table 4-2. Summary of Seasonal Snowpack Characteristics Inferred from iButton Stakes at the Study Sites from 2017-2019.

Year	Site	Maximum Snow Depth (cm)		Snow Depth Days (metre days)		Snow-on-Ground Duration (days)	
		UNBURNED	BURNED	UNBURNED	BURNED	UNBURNED	BURNED
2017-2018	TB	130	90	186.5	124.8	227	208
	WB	>140	130	>177.0	176.4	239	225
2018-2019	TB	>140	130	>160.9	143.6	213	197
	WB	>140	>140	>157.7	>153.1	236	222
	BR	>160	150	>252.9	200.0	219	210

The late-winter snow surveys carried out at the study sites provide additional information on spatial differences between the burned areas and the undisturbed forest. As at the snow stakes, mean and median snow depths were greater in the unburned region than the burned region at WB (143 cm versus 110 cm) (Figure 4-4-A; Appendix A). In contrast, the pattern at the snow stakes was not maintained along the transects at the other two sites, so that burned and unburned average snow depths were similar at TB (114 cm versus 120 cm), and lower average snow depths were observed in the unburned portions than in the burned parts at BR (155 cm versus 173 cm). Variability at all sites was high, with ranges that exceeded 100 cm in almost all cases (Appendix A).

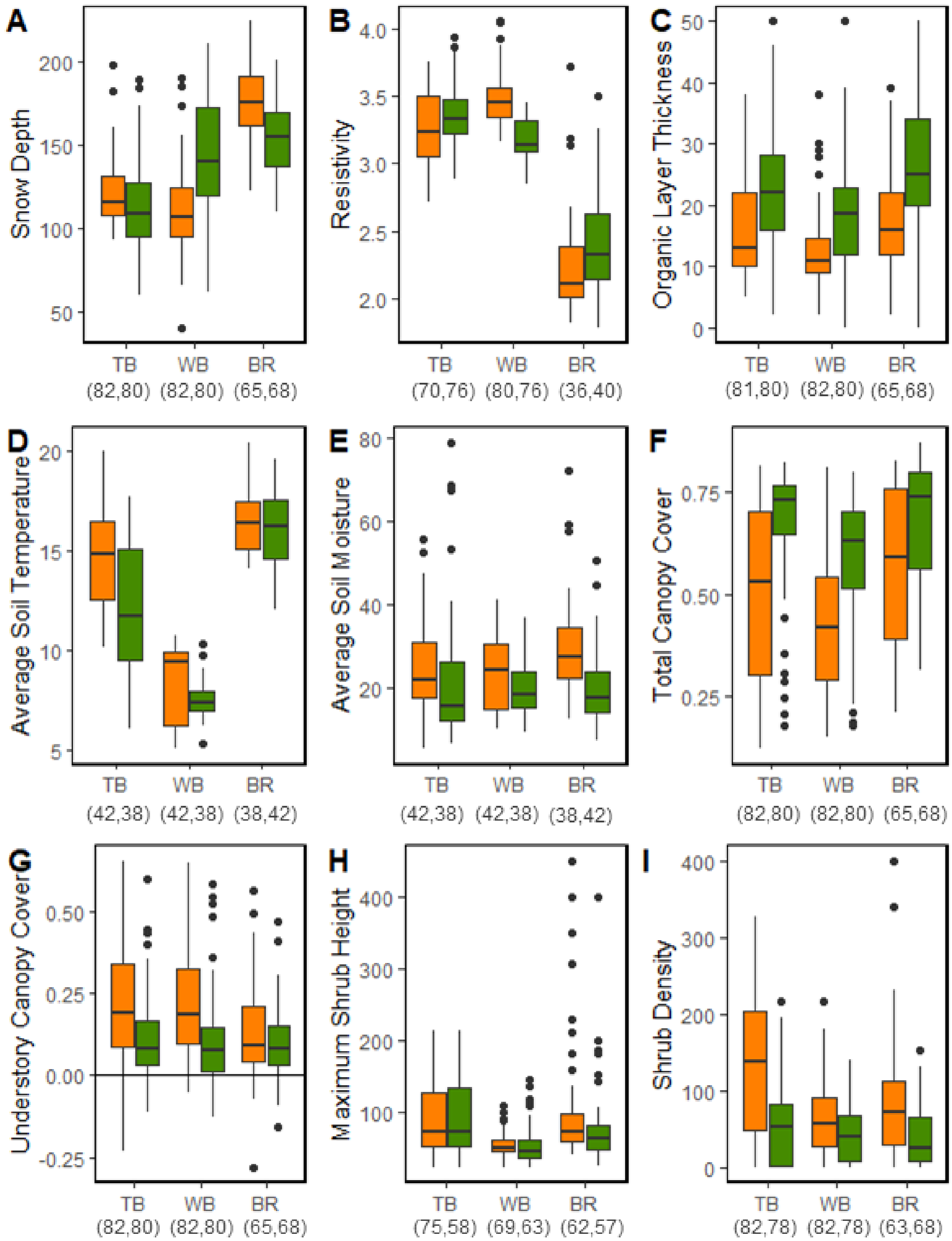

Figure 4-4. Boxplots of measurements in burned (orange) and unburned (green) portions of transects at the Tikkoatokak Bay (TB), Webb Bay (WB), and Beaver River (BR) sites: (A) snow depth (cm); (B) near-surface resistivity (Ωm; logarithmically-transformed); (C) organic layer thickness (cm); (D) average soil temperature (°C); (E) average volumetric soil moisture (cm^3/cm^3); (F) total canopy cover; (G) understory canopy cover; (H) maximum shrub height (cm); and (I) shrub density (stems/m^2). Boxplots represent the median (black line) and the upper and lower quartiles (box boundaries). Whiskers represent the minimum and maximum values. Outliers are identified as points. The number of observations (n) for each boxplot are included in brackets.

4.5.2 Ground Conditions

Two ERT surveys were completed across burned to unburned transitions at each site. Frost probing and instantaneous temperature measurements, where possible, confirmed instances of frozen ground in the unburned forest, typically at depths of 40 to 50 cm. Frozen ground was not detected in any of the fire-disturbed portions of the profiles.

Most of the TB1 tomogram exhibits modelled resistivities below 1600 Ωm. Values in the burned portion of the profile are generally lower than those in the forested section at the same depth, and there are three high resistivity anomalies. The two in the upper 2 m in the burned area between 15 m and 22 m and in the unburned forest between 53 m and 59 m are interpreted as dry soil and shallow rock, respectively. The third anomaly in the middle of the profile at depths of at least 6 m could be bedrock or possibly degrading permafrost. No instances of frozen ground were detected by frost probing in late-July 2019 (Figure 4-5-A). Resistivities along TB2 (Figure 4-5-B) were generally higher than those at TB1, especially beneath the unburned forest. Resistivities decreased with depth in the burned area from 3200 to 6400 Ωm in the upper 4 m to 1000 to 2000 Ωm at greater depths. The former likely reflects dry, well-drained conditions near the start of the transect. In the unburned forest, resistivity patterns were complex, but almost all values exceeded 6400 Ωm, with the deepest layers exceeding 20000 Ωm. Modelled blocks with values below 6400 Ωm between 63 and 80 m in the near-surface corresponded to the location of two small streams that ran perpendicular to the profile. The correlation of the defined frost table and the pattern of resistivities, supplemented by field observations of fine-grained, frost-susceptible sediments, strongly suggests the presence of permafrost beneath the forest at TB2 and its absence beneath the burned area. High resistivities exceeding 10000 Ω at depths of at least 7 m may be frozen ground or bedrock (frozen or unfrozen).

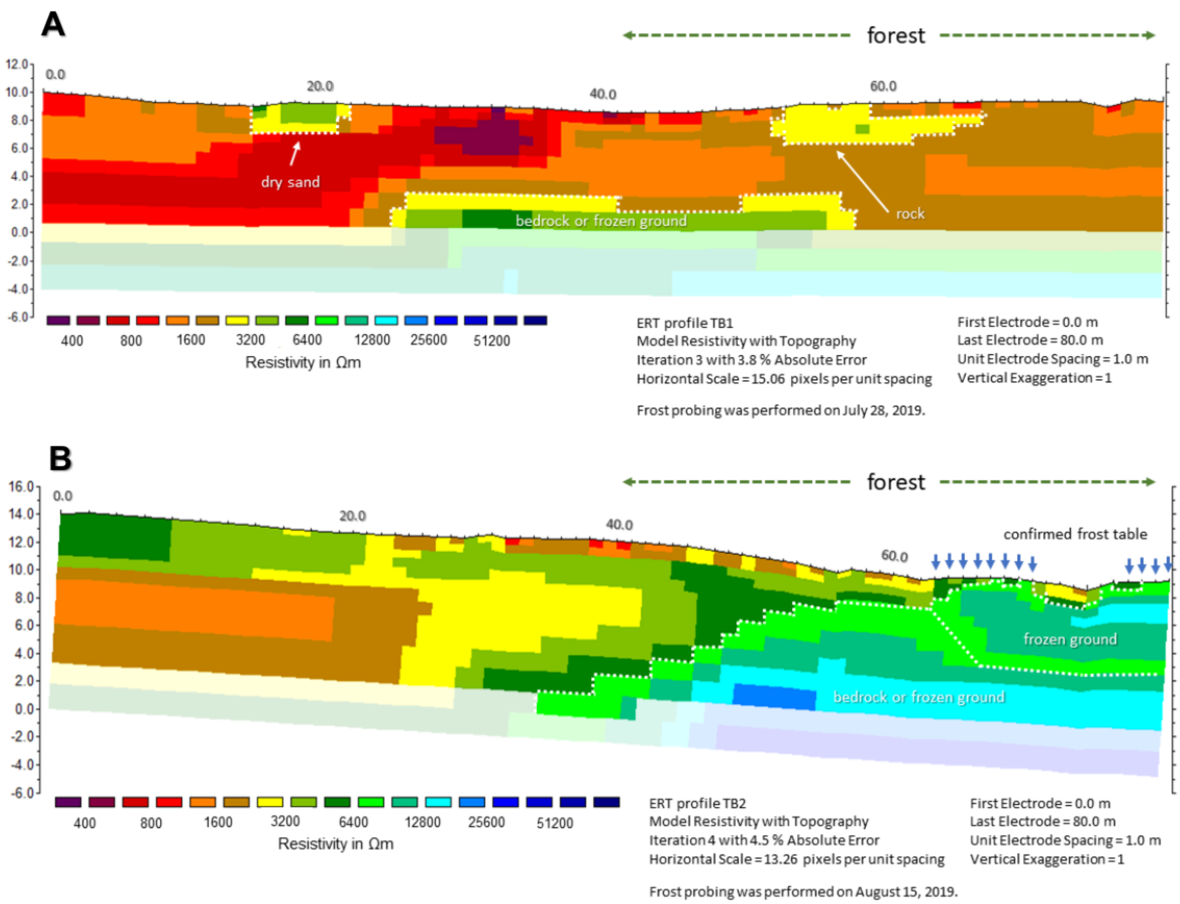

Figure 4-5. Modelled Resistivities of ERT Profiles (A) TB1 and (B) TB2. Confirmed frost tables within the upper 120 cm of the ground surface are identified by blue arrows, and tomograms are faded in areas where sensitivity values are less than 0.1, as in Way et al. (2018). Interpretations of frozen ground and other notable ground properties are identified.

The tomograms for WB1 and WB2 show three- or four-layered systems, which broadly alternate from lower to higher values from the surface to the depth of investigation (Figure 4-6). Lateral variation occurs within the layers, resulting in positive anomalies within both the burned and unburned portions of the profiles. Modelled resistivities range from minima of 800 Ωm, usually within the upper 2 m of the profile, to maxima of 16000 to 25600 Ωm in high resistivity zones in the burned portions of the transect. Probing and other site observations showed that these high resistivity zones, centred between 0 and 15 m along WB1 and 15 and 32 m along WB2, corresponded to areas with dry sand and not to frozen ground. Frost probing and temperature measurements within the forest at WB1, however, confirmed the presence of frozen ground, particularly beneath dense tree stands located in the forest from 51 to 52 m and 69 to 72 m, and this was associated with modelled resistivities exceeding 3200 Ωm. Based on the tomogram, these bodies of frozen ground extended to maximum depths of 5 m. At WB2, frozen ground was detected by probing in late-July 2019 in the unburned forest, between 61 and 62 m and 71 and 75 m. These areas of the tomogram show values exceeding 3200 Ωm as at WB1, but these extend only to depths of about 4 m. The layered patterns in the forest at both WB1 and WB2, therefore, are interpreted as the active layer overlying thin permafrost, which in turn overlies unfrozen sediments and bedrock that extend across the base of the profile.

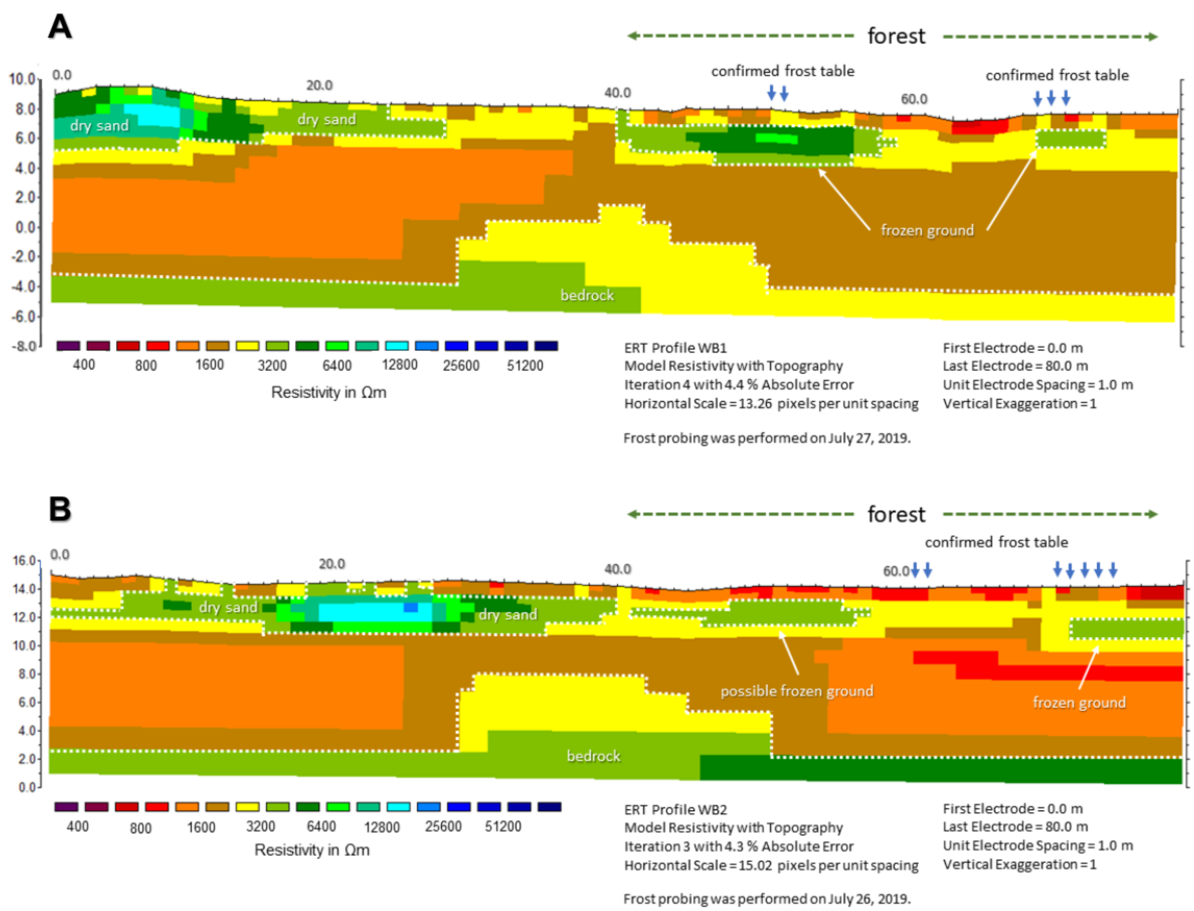

Figure 4-6. Modelled Resistivities of ERT Profiles (A) WB1 and (B) WB2. Confirmed frost tables within the upper 120 cm of the ground surface are identified by blue arrows, and tomograms are faded in areas where sensitivity values are less than 0.1, as in Way et al. (2018). Interpretations of frozen ground and other notable ground properties are identified.

The two tomograms at BR show a two-layered system, with a slightly higher near-surface resistivity layer of typically 200 to 600 Ωm overlying a low resistivity layer below 100 Ωm that extends to the base of the profile (Figure 4-7). Higher resistivity anomalies are present at the end of BR1 and the start and end of BR2. No frozen ground was detected along BR1, and only one location at the end of BR2 gave an indication of frozen materials. The very low values comprising most of the profiles indicate saturated, unfrozen soils. The near-surface layer is drier, which results in slightly higher resistivities. An undulating bedrock surface likely results in the higher resistivity anomalies, with the one at the end of BR2 being due to seasonally frozen ground. Permafrost is therefore absent beneath both the forest and the burned areas.

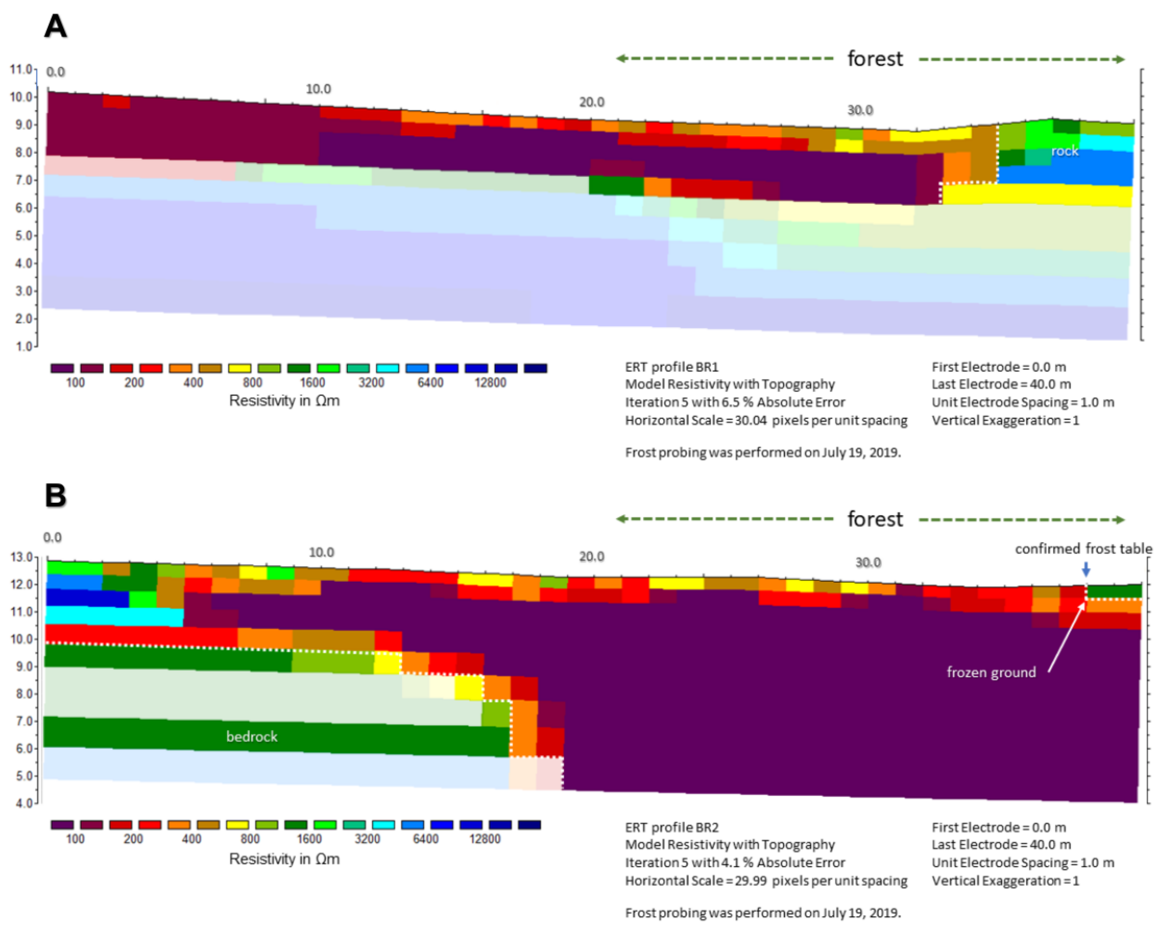

Figure 4-7. Modelled Resistivities of ERT Profiles (A) BR1 and (B) BR2. Confirmed frost tables within the upper 120 cm of the ground surface are identified by blue arrows, and tomograms are faded in areas where sensitivity values are less than 0.1, as in Way et al. (2018). Interpretations of

frozen ground and other notable ground properties are outlined and identified. Note the much lower resistivity scale used compared to Figures 4-5 and 4-6.

The overlap between resistivities in the six tomograms that are inferred to represent (i) dry, unfrozen coarse-grained sediments, (ii) frozen soils of varying grain-sizes with low ice contents, and (iii) bedrock, results in no clear pattern in the summary of near-surface (0.5 to 1.05 m depth) resistivities in burned and unburned areas (Figure 4-4-B). The median value is higher beneath the forest than in the burned area at TB, but the reverse is true at WB. The most obvious difference is between the higher median values at the two sites near Nain and the lower ones at BR, and this is due to wetter conditions and finer-grained soils at the latter.

Organic layer thicknesses in the burned regions at all three sites were less than in the undisturbed forest due to loss by combustion. Average values, 14 to 22 years after the fires took place, differed by 7 cm at TB, 6 cm at WB, and 10 cm at BR, while maximum values differed by 11 to 12 cm (Appendix A). Substantial overlaps in the distributions (Figure 4-4-C) reflect the low intensity nature of the initial fire disturbances, with combustion causing relatively little loss of organic material (Brehaut and Brown, 2020). In the burned area, the thickest organic mat was observed at BR, the oldest fire site, while the thinnest was observed at WB, the youngest fire site.

Average soil temperatures measured along the transects at all three sites were 0.3 to 2.6°C higher in the fire-affected area than in the unburned forest (Figure 4-4-D). Differences were larger at TB and WB, where near-surface frozen ground was present in the forest, and minimal at BR, where frozen ground was almost entirely absent. However, the high standard deviations (Appendix A), relative to the magnitude of the intra-site differences, suggest that differences in instantaneous soil surface temperatures between burned and unburned regions may not be significant.

Average soil moistures measured at the three sites were higher in the fire-affected area than in the unburned forest (Figure 4-4-E), possibly reflecting lower rates of evapotranspiration following fire (Holloway et al., 2020). Due to the high standard deviations in soil moisture values, the minor burned versus unburned differences of 0.02 and 0.04 cm^3/cm^3 at TB and WB, respectively, were likely negligible (Appendix A). At BR, average volumetric soil moisture differed by 0.11 cm^3/cm^3 between the burned and unburned areas, but standard deviations remained high.

4.5.3 Vegetation Conditions

Average canopy cover in the unburned areas at the three sites varied from 60 to 68% (Figure 4-4-F). The value was lowest at WB, indicating that the forest was most open at this site. Burned regions exhibited lower average total coverage, ranging from 44 to 57%, and higher variance (Appendix A). The understory canopy coverage, provided by vegetation measuring less than 1.3 m in height, was higher in the burned region than the unburned region at all sites (Figure 4-4-G). This difference was most pronounced at the TB and WB sites, where the average understory canopy coverage in the burned regions of 21 to 22% was approximately double the average coverage of 10 to 11% in the unburned regions. At BR, the average understory canopy coverage in the burned area was 13 %, while the coverage in the unburned forest was 10%. Unburned regions exhibited lower variance in understory canopy coverage than burned regions (Appendix A).

At TB, maximum shrub heights of 215 cm were documented in both burned and unburned areas, with similar mean maximum shrub heights of just under 1 m. WB had the shortest shrubs of the three sites, with maximum heights of 147 cm in the unburned forest and only 110 cm in the burned area (Appendix A). Few willows and alders were observed at WB, especially in the burned area, and shrub cover along the transects were dominated by Labrador tea, which typically grow to a maximum height of 1.5 m. Shrubs were tallest at BR and exceeded 4 m in both burned and unburned areas, due to tall patches of willows and alders. However, high standard deviations show that the burned versus unburned differences in maximum shrub height were not significant, especially at TB and WB (Appendix A).

Intra-site differences in shrub densities were more pronounced than those for maximum shrub heights. Shrub densities were consistently higher in the burned areas (Figure 4-4-I), but they still ranged from 0 stems/m^2 to over 300 stems/m^2 at the TB and BR sites, where layering of willow and alder branches was observed. At TB, shrub densities were two to three times greater in the burned region, when compared with the unburned forest. At WB, average shrub densities were 50% higher in the burned region than in the unburned forest, but WB had fewer shrubs than the TB and BR sites, particularly in the burned area (Appendix A). At BR, shrub stems were measured to be at least twice as dense in the burned area, relative to the unburned forest. High shrub density measurements in the burned regions at all three sites are consistent with patterns of greater understory coverage in the fire-affected area, compared to the undisturbed forest (Figure 4-4-G).

4.5.5 Intra-Site Variable Interactions

The PCA provides an overview of relationships among the field variables at the three sites. The first three PCs accounted for very similar percentages of the total variance at each site: 64.0% at TB, 66.9% at WB, and 62.3% at BR. The highest variance accounted for by the first PC was 31.6% at TB, and the lowest was 27.4% at BR. No consistent relationships or associations between the variables were identified through the various biplot combinations (Figure 4-8). Overall similar loadings, and relatively few loadings greater than 0.4 or less than -0.4, demonstrate that all variables are similarly loaded on the various PCs (Table 4-3).

Table 4-3. Summary of Loadings, Accounted Variance, and the Eigenvalue of Retained Principal Components for the BR, TB, and WB Sites. The number of observations (n) for each site are identified in brackets. Loadings >0.4 or <-0.4 are shown in green or red, respectively.

	TB (n=69)			WB (n=78)			BR (n=76)		
	PC1	PC2	PC3	PC1	PC2	PC3	PC1	PC2	PC3
Eigenvalue	2.5	1.6	1.0	2.3	1.7	1.3	2.2	1.7	1.1
Variance (%)	31.6	19.5	12.9	28.9	21.5	16.5	27.4	21.0	13.9
Snow Depth	0.20	0.48	0.27	0.10	0.41	0.50	0.41	0.07	0.32
Organic Layer Thickness	0.22	-0.30	0.67	0.46	0.16	-0.01	-0.22	0.00	0.81
Near-Surface Resistivity	-0.53	0.08	-0.01	-0.40	-0.32	-0.18	-0.47	-0.28	-0.19
Soil Temperature	0.30	0.46	0.19	0.32	-0.24	-0.56	0.02	-0.60	0.26
Soil Moisture	0.30	-0.32	-0.55	-0.54	0.03	0.28	0.45	0.14	0.11
Total Canopy Cover	-0.11	-0.52	0.37	0.18	0.53	-0.16	-0.43	-0.18	0.19
Maximum Shrub Height	0.41	-0.30	-0.03	0.35	-0.34	0.39	0.23	-0.54	-0.29
Shrub Density	0.53	0.07	-0.09	0.27	-0.50	0.38	0.35	-0.47	0.12

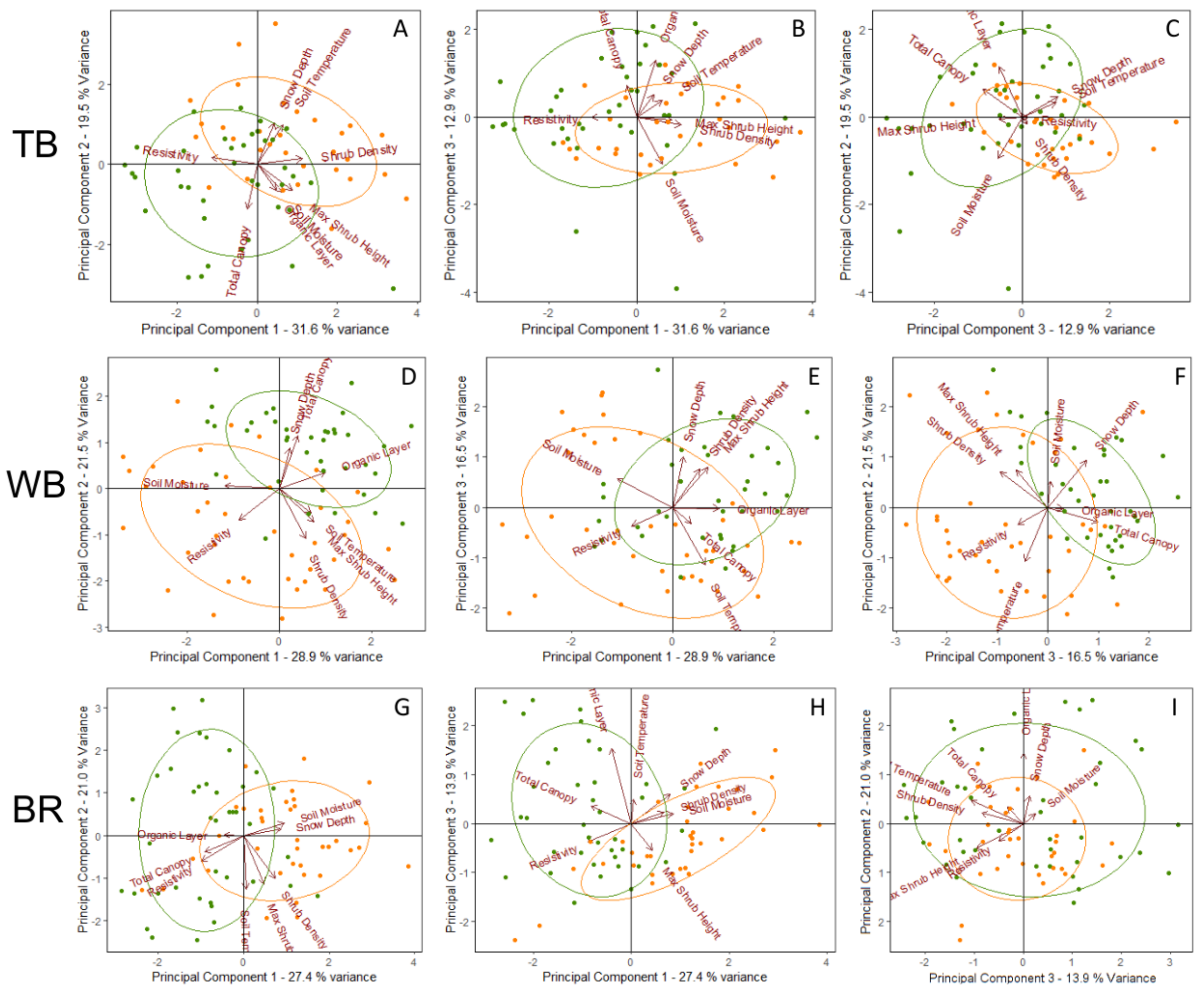

Figure 4-8. Biplots of Burned and Unburned Observations on (A-D-G) Principal Components 1 and 2, (B-E-H) Principal Components 1 and 3, and (C-F-I) Principal Components 2 and 3 at the TB, WB, and BR sites. Observations collected in the burned and unburned regions and their normal data ellipses (68% confidence intervals) are shown in orange and green, respectively.

At TB, observations in the unburned forest vary more than those collected in the burned area, and considerable overlap of burned and unburned scores occurs in all biplot combinations (Figure 4-8-ABC). The overlap of disturbed and undisturbed scores suggests that the change from burned to unburned conditions at TB is gradational and less distinct than that of the two other sites, despite the recency of the TB fire, especially relative to BR. Organic layer thickness and soil moisture demonstrate similar loadings on the first two PCs, but they have strongly opposing loadings on PC3 (Table 4-6). At TB, soil temperature is most strongly loaded on PC2 (Table 4-6), and it remains well-associated with snow depth in all biplot combinations (Figure 4-8-ABC), suggesting that locations with greater snow depths tend to have higher soil temperatures. While these temperature measurements are instantaneous and do not represent mean seasonal or annual values, this relationship between snow depth and soil temperature agrees with post-fire increases in soil temperature and active layer thaw depths reported in the western boreal forest (Bonnaventure and Lamoureux, 2013; Smith et al., 2015).

At WB, the observations collected in the burned section demonstrate greater variance when compared to those from the unburned region (Figure 4-8-DEF), suggesting greater homogeneity in the forest. The biplot of PC 3 versus PC 1 shows the greatest overlap in the distribution of burned versus unburned scores (Figure 4-8-F). Therefore, PC2, which is positively correlated with snow depth and total canopy cover and negatively correlated with shrub density (Table 4-6), is responsible for distinct differences between the burned and unburned areas of the WB site (Figure 4-8-DF). This supports intra-site observations of greater snow depth and greater canopy coverage in the unburned forest at WB, and thicker and taller shrubs in the burned area (Figure 4-4).

The BR site demonstrates greater variance amongst the observations collected in the unburned region, particularly along PC2 (Figure 4-8-GI), which is inversely related to soil temperature, maximum shrub height, and shrub density (Table 4-6). Plotting of PCs 2 and 3 shows almost complete overlap in the scores for burned and unburned areas (Figure 4-8-I), demonstrating that PC1 is responsible for distinct differences between the disturbed and undisturbed regions at this site (Figure 4-8-GH). This supports intra-site observations of greater canopy coverage in the unburned forest at BR, and greater snow depths and wetter soil conditions in the burned area (Figure 4-4).

4.6 Discussion

4.6.1 Post-Fire Vegetation Conditions

Post-fire vegetation regeneration in Labrador is dominated by ericaceous shrubs, including Labrador tea and various blueberry species (Foster, 1985; Elson et al., 2007; Oberndorfer, 2020), and deciduous shrubs, like willows and alders (Foster, 1983). The high variability in total canopy coverage in the burned areas reflects the patchy nature of shrub growth and distribution. Overall shrub densities were greater in the fire-affected areas where vegetation growth was facilitated by warmer soil temperatures and a lack of competing vegetation (Foster, 1985; Brehaut and Brown, 2020). Ground temperatures tend to be higher on south-facing slopes due to enhanced insolation (French, 2017), and this is reflected in inter-site differences in shrub height and abundance. The south-facing TB and BR sites had patches of willows and alders exceeding 2 m and 4 m in height, respectively. In contrast, shrubs at the north-facing WB site did not exceed 1.5 m in height and were mostly Labrador tea. WB also exhibited the smallest thawing index and the largest freezing index, resulting in the lowest mean annual air temperature of the three sites, the longest snow-on-ground season, and the shortest growing season. These differences are associated with its north-facing aspect and proximity to the open ocean, compared to TB, and its higher latitude, compared to BR. Conversely, the enhanced vegetation cover at BR relates to its warmer mean annual air temperature, shorter snow-on-ground period, and longer growing season.

Shrubs play a complex role in the post-fire environment. At our sites, it is unclear whether shrubs have facilitated tree seedling establishment and development through nursing and protection from environmental harshness and seed predation (Cranston, 2009), or whether they have competed with seedlings for space and resources (Brehaut and Brown, 2020). It is suggested that current shrub dominance may correspond to an early successional response, and that a slow increase in black spruce establishment could occur at our sites in the coming decades (Brehaut and Brown, 2020). The rapid post-fire shrub establishment and slow post-fire tree establishment processes that are believed to be occurring could exacerbate the thaw of any underlying permafrost which is also being affected by unfavourable post-fire climatic conditions (Chapter 5).

4.6.2 Snow Distribution and Vegetation Dynamics

As we hypothesized, average snow depths along the survey lines were higher in the burned region than the unburned region at the TB and BR sites, even though the iButton stakes indicated the opposite at the time of the winter site visits. At WB, the iButton stakes showed virtually the same snow depths in the burned and unburned areas at the time of the winter site visits, while the snow survey indicated a thicker snowpack in the forest. Greater snow in burned regions is consistent with investigations of post-fire snow dynamics in both Alberta (Burles and Boon 2011) and Oregon (Gleason et al. 2013). The deeper average snowpack in the unburned forest at the time of measurement at WB is attributed to its low tree density (0.86 stems/m^2; Brehaut and Brown, 2020) resulting in an open canopy that offers less protection against wind redistribution events (Revuelto et al., 2015). Both TB and BR had noticeably higher tree densities (2.38 and 2.48 stems/m^2, respectively; Brehaut and Brown, 2020), and their canopies were more closed, aiding interception. Tree density may also be related to forest age (Bingham and Sawyer Jr., 1991); in a sample of 5 to 12 trees at each site, WB had the oldest trees (100 to 286 years old), trees at BR were slightly younger (117 to 266 years), and TB trees were the youngest (51 to 142 years; Brehaut and Brown, 2020).

Shrubs in burned areas were expected to impact frozen ground through the ground warming effect of snow-trapping (Sturm et al., 2000; Liston et al., 2002; Myers-Smith and Hik, 2013; Busseau et al., 2017). However, clear relationships between snow depth and maximum shrub height or density were not evident at our sites, even though they were close to open water in summer or ice cover in winter (TB and WB) or in a relatively flat area (BR), where wind-driven redistribution of snow could be expected. Instead, snow depths may have been more affected by topography (Pomeroy et al., 2006), regardless of shrub presence or absence (Wilcox et al. 2019). The limited impact of shrubs on snow distribution may also be attributed to the complexity of the post-fire landscape. Previous studies of snow-shrub interactions have been primarily conducted in tundra environments where topography and shrubs were the only drivers of snow distribution (e.g., Sturm et al., 2000; Liston et al., 2002; Myers-Smith and Hik, 2013; Wilcox et al., 2019). However, in a post-fire environment, the presence of other erect vegetation, including standing dead and regenerating trees, may intercept and reduce the snow-trapping abilities of shrubs. Overall, at our sites, it appears that snow distribution is primarily influenced by local topography and tree canopy closure, as described above.

Shrubs can also influence snow dynamics by advancing snowmelt, especially where they protrude through the snowpack (Wilcox et al., 2019), as tall willows and alders do at TB and BR. Snowmelt is enhanced by canopy loss, resulting in lower snow interception, higher incoming solar radiation, lower overall land surface roughness, and greater wind activity and turbulent heat transfers (Burles and Boon, 2011), as well as the emission of longwave radiation from shrubs (Wilcox et al., 2019) and standing dead (Pomeroy et al., 2009; Burles and Boon, 2011). Snow always ablated earlier at the burned parts of our sites, allowing the ground to start thawing earlier in the spring. We contend that the deep snowpacks at our sites in both burned and unburned areas limit the differential winter impact of shrubs on the ground thermal regime, but shrub cover may affect it in the early part of the spring and summer due to earlier ground thaw.

4.6.3 Frozen Ground Conditions

Interpretation of modelled resistivities in the tomograms is challenging as there is no universal threshold to differentiate between frozen and unfrozen materials. Values used in Canada range from 300 to 400 Ωm (Lewkowicz et al., 2011) to 800 to 1000 Ωm (McClymont et al., 2013; Way and Lewkowicz 2015). Validation of the tomograms at our sites was done using frost probing and instantaneous temperature measurements, but ambiguity remains for several reasons. First, clasts were present at many spots so that refusal of the probe had to be interpreted by the operator as due to frost or a stone. Second, probing was primarily carried out in late-July, which means that an encountered frost table could be a remnant of seasonal frost. Third, the unknown stratigraphy at depth and the potential for overlap in resistivities between dry, unfrozen coarse soils and frozen fine-grained soils, as well as bedrock, made interpretation difficult.

Despite these challenges, the low resistivity values at BR clearly indicate that there is no permafrost along the transects at this southern site. The modelled resistivities likely reflect the higher proportion of clay in the sediments at BR, resulting in higher porosities and cation exchange capacities (Sharma, 1997), compared to the sandier substrates found at the TB and WB sites. In contrast, thin permafrost is interpreted to be present in the undisturbed forest at both sites near Nain. A conservative threshold of 3200 Ωm to represent frozen beach deposits leads to patches of frozen ground on profiles WB1 and WB2 beneath dense groupings of trees that provide shade in the summer and intercept falling snow in the winter. At TB, bodies of frozen ground with modelled resistivities exceeding 6400 Ωm are present on profile TB2 beneath the forest. Given that the fires took place 14 to 22 years before the ERT surveys and that the climate has warmed in the meantime, a loss of permafrost due to increasing ground temperatures in the burned areas at TB and WB is conceivable (e.g., Burn, 1998; Nossov et al., 2013; Smith et al., 2015; Holloway et al., 2020). However, it is also possible that higher resistivities at depth beneath parts of the burned areas could be degrading permafrost and not bedrock, especially as modelling suggests that permafrost may be able to persist for decades, even in sites where ground temperatures are close to 0°C (Chapter 5). If permafrost has degraded as we infer, this is due to a combination of a thinner organic mat, an earlier snowmelt, and loss of shading, but not apparently because of shrubs causing a deeper snowpack as suggested in western Canada (Sturm et al., 2000; Liston et al., 2002; Myers-Smith and Hik, 2013). Despite the ambiguity of ground thermal conditions at depth, these observations of perennially frozen ground at TB and WB constitute some of the first present-day findings of permafrost in forested lowland locations in coastal Labrador, where permafrost was previously believed to be absent due to thick snow cover (Way and Lewkowicz, 2018).

4.7 Conclusions

The post-fire response recorded at our study sites broadly agrees with previous studies performed in the western North American boreal forest. Thin permafrost, less than 5 m in thickness, was interpreted as present in the unburned forest at our two sites near Nain, and its persistence was attributed to the cooling effects of the undisturbed forest canopy and to a notable proportion of fine-grained materials at TB (Chapter 5). Slow post-fire tree regeneration, a thin post-fire organic mat, and short snow-on-ground seasons in the burned areas were deemed to be responsible for the lack of frozen ground in fire-affected areas. We contend that snow accumulation is primarily driven by the presence or absence of an intact forest canopy, and that the deep snowpack and the presence of other erect vegetation limit the thermal role of shrubs in overall post-fire snow and ground dynamics.

Burned and unburned regions differ primarily in terms of snow depth, near-surface resistivity, soil moisture, total canopy cover, and shrub density, particularly at the WB and BR sites. Inter-site differences, including sediment material properties, site aspect, and climate, and conditions of the disturbance itself, including age, size, and severity, complicate our understanding of large-scale differences between our study sites. Despite these limitations, this study is a step forward in our understanding of both summer and winter post-fire environmental response in the coastal boreal forests of the eastern Canadian subarctic.

4.8 Acknowledgements

We are grateful to the Nunatsiavut Government for permission to conduct research on the traditional lands of the Labrador Inuit (Permit #9222380). Funding for this research was provided by Polar Knowledge Canada (PI: Carissa Brown) and the Northern Scientific Training Program. Y. Wang acknowledges financial support from the W. Garfield Weston Foundation and the Natural Sciences and Engineering Research Council of Canada. We would like to thank the Nunatsiavut Research Centre and the Labrador Institute of Memorial University for logistical and in-kind support, and we gratefully acknowledge Frédéric Dwyer-Samuel, Alain Cuerrier, Caitlin Lapalme, Harold Goudie, Shirley Goudie, Jim Goudie, Gillian Gear, Ches Webb, Joe Webb, William Ikkusek, Edward Sillett, Carla Pamak, Liz Pijogge, Paul McCarney, and Rodd Laing for their collaboration and support of our field investigations.

4.9 References

Balshi, M.S., McGuire, D., Duffy, P., Flannigan, M., Walsh, J., Melillo, J. (2009). Assessing the Response of Area Burned to Changing Climate in Western Boreal North America Using a Multivariate Adaptive Regression Splines (MARS) Approach. *Global Change Biology*, 15: 578-600.

Banfield, C.E. and Jacobs, J.D. (1998). Regional Patterns of Temperature and Precipitation for Newfoundland and Labrador During the Past Century. *The Canadian Geographer/Le Géographe canadien*, 42(4): 354-364.

Bell, T., Putt, M., Sheldon, T. (2011). Landscape Hazard Assessment in Nain: Phase I: Inventory of Surficial Sediment Types and Infrastructure Damage, Final Report to Nunatsiavut Government and Nain Inuit Community Government.

Bingham, B.B. and Sawyer Jr., J.O. (1991). Canopy Structure and Tree Condition of Young, Mature, and Old-Growth Douglas-Fir/Hardwood Forests. In Proceedings of the 1991 Symposium on Biodiversity of Northwestern California 1991.

Bonnaventure, P.P. and Lamoureux, S.F. (2013). The Active Layer: A Conceptual Review of Monitoring, Modelling Techniques and Changes in a Warming Climate. *Progress in Physical Geography*, 37: 352-376.

Brandt, J.P. (2009). The Extent of the North American Boreal Zone. *Environmental Reviews*, 17: 101-161.

Brehaut, L.D. and Brown, C.D. (2020). Boreal Tree Regeneration After Fire and Fuelwood Harvesting in Coastal Nunatsiavut. *Arctic Science*, DOI: 10.1139/as-2019-0016.

Brown, D.R.N., Jorgenson, M.T., Douglas, T.A., Romanovsky, V.E., Kielland, K., Hiemstra, C., Euskirchen, E.S., Ruess, R.W. (2015). Interactive Effects of Wildfire and Climate on Permafrost Degradation in Alaskan Lowland Forests. *Journal of Geophysical Research: Biogeosciences*, 120: 1619-1637.

Brown, J., Ferrians, O., Heginbottom, J.A., Melnikov, E. (2002). Circum-Arctic Map of Permafrost and Ground-Ice Conditions, Version 2. *NSIDC: National Snow and Ice Data Center*.

Burles, K. and Boon, S. (2011). Snowmelt Energy Balance in a Burned Forest Plot, Crowsnest Pass, Alberta, Canada. *Hydrological Processes*, 25: 3012-3029.

Busseau, B.-C., Royer, A., Roy, A., Langlois, A., Domine, F. (2017). Analysis of Snow-Vegetation Interactions in the Low Arctic-Subarctic Transition Zone (Northeastern Canada). *Physical Geography*, 38(2): 159-175.

Burn, C.R. (1998). The Response (1958-1997) of Permafrost and Near-Surface Ground Temperatures to Forest Fire, Takhini River Valley, Southern Yukon Territory. *Canadian Journal of Earth Sciences*, 35: 184-199.

Coops, N.C., Hermosilla, T., Wulder, M.A., White, J.C., Bolton, D.K. (2018). A Thirty Year, Fine-Scale, Characterization of Area Burned in Canadian Forests Shows Evidence of Regionally Increasing Trends in the Last Decade. *PLoS ONE*, 13(5): e0197218.

Cranston, B. (2009). The Stress Gradient Hypothesis: Plant Facilitation at the Forest-Tundra Transition (Mealy Mountains, Labrador, Canada). M.Sc. Thesis, Department of Biology, Memorial University of Newfoundland, St. John's, NL, 81pp.

Crown-Indigenous Relations and Northern Affairs Canada. (2007). Inuit Regions (Inuit Nunangat). Retrieved from https://open.canada.ca/data/en/dataset/f242b881-75e3-40bb-a148-63410b4ce2af.

Danby, R.K. and Hik, D.S. (2007). Responses of White Spruce (*Picea glauca*) to Experimental Warming at Subarctic Alpine Treeline. *Global Change Biology*, 13: 437-451.

Elson, L.T., Simon, N.P.P., Kneeshaw, D. (2007). Regeneration Differences Between Fire and Clearcut Logging in Southeastern Labrador: A Multiple Spatial Scale Analysis. *Canadian Journal of Forest Research*, 37: 473-480.

Environment and Climate Change Canada. (2020). Canadian climate normal, 1981-2010. Retrieved from www.climate.weather.gc.ca.
Fisher, J.P., Estop-Aragones, C., Thierry, A., Charman, D.J., Wolfe, S.A., Hartley, I.P., Murton, J.B., Williams, M., Phoenix, G.K. (2016). The Influence of Vegetation and Soil Characteristics on Active-Layer Thickness of Permafrost Soils in Boreal Forest. *Global Change Biology*, 22: 3127-3140.
Flannigan, M.D., Logan, K.A., Amiro, B.D., Skinner, W.R., Stocks, B.J. (2005). Future Area Burned in Canada. *Climatic Change*, 72: 1-16.
Fortier, R., LeBlanc, A.-M., Allard, M., Buteau, S., Calmels, F. (2008). Internal Structure and Conditions of Permafrost Mounts at Umiujaq in Nunavik, Canada, Inferred from Field Investigation and Electrical Resistivity Tomography. *Canadian Journal of Earth Sciences*, 45: 367-387.
Foster, D.R. (1983). The History and Pattern of Fire in the Boreal Forest of Southeastern Labrador. *Canadian Journal of Botany*, 61(9): 2459-2471.
Foster, D.R. (1985). Vegetation Development Following Fire in Picea Mariana (Black Spruce)-Pleuzorium Forests of South-Eastern Labrador, Canada. *Journal of Ecology*, 73(2): 517-534.
French, H.M. (2017). The Periglacial Environment, Fourth Edition. John Wiley and Sons.
Gleason, K.E., Nolin, A.W., Roth, T.R. (2013). Charred Forests Increase Snowmelt: Effects of Woody Debris and Incoming Solar Radiation on Snow Ablation. *Geophysical Research Letters*, 40: 4654-4661.
Hanes, C.C., Wang, X., Jain, P., Parisien, M.A., Little, J.M., Flannigan, M.D. (2018). Fire-Regime Changes in Canada Over the Last Half Century. *Canadian Journal of Forest Research*, 49: 256-269.
Hare, F.K. (1950). Climate and Zonal Divisions of the Boreal Forest Formation in Eastern Canada. *The Geographical Review*, 40(4): 615-635.
Hauck, C., Isaksen, K., Vonder Mühll, D., Sollid, J.L. (2004). Geophysical Surveys Designed to Delineate the Altitudinal Limit of Mountain Permafrost: An Example from Jotunheimen, Norway. *Permafrost and Periglacial Processes*, 15: 191-205.
Heginbottom, J.A., Dubreuil, M.A., Harker, P.A. (1995). Canada Permafrost, in National Atlas of Canada, 5th edition, Natural Resources Canada.
Hilbich, C., Marescot, L., Hauck, C., Loke, M.H., Mäusbacher, R. (2009). Applicability of Electrical Resistivity Tomography Monitoring to Coarse Blocky and Ice-Rich Permafrost Landforms. *Permafrost and Periglacial Processes*, 20: 269-284.
Holloway, J.E., Lewkowicz, A.G., Douglas, T.A., Li, X., Turetsky, M.R., Baltzer, J.L., Jin, H. (2020). Impact of Wildfire on Permafrost Landscapes: A Review of Recent Advances and Future Prospects. *Permafrost and Periglacial Processes*, DOI: 10.1002/ppp.2048.
Isaksen, K., Hauck, C., Gudevang, E., Odegard, R.S., Sollid, J.L. (2002). Mountain Permafrost Distribution in Dovrefjell and Jotunheimen, Southern Norway, Based on BTS and DC Resistivity Tomography Data. *Norwegian Journal of Geography*, 56: 122-136.
Johnson, J.P. (1969). Deglaciation of the Central Nain-Okak Bay Section of Labrador. *Arctic*, 22(4): 373-394.
Jorgenson, M.T., Romanovsky, V., Harden, J., Shur, Y., O'Donnell, J., Schuur, E.A.G., Kanevskiy, M., Marchenko, S. (2010). Resilience and Vulnerability of Permafrost to Climate Change. *Canadian Journal of Forest Research*, 40: 1219-1236.

Kneisel, C., Hauck, C., Fortier, R., Moorman, B. (2008). Advances in Geophysical Methods for Permafrost Investigations. *Permafrost and Periglacial Processes*, 19: 157-178.

Lémus-Lauzon, I., Bhiry, N., Woollett, J. (2012). Napâttuit: Wood Use by Labrador Inuit and its Impact on the Forest Landscape. Inuit Studies, 36: 113-137.

Lévesque, E., Hermanutz, L., Gérin-Lajoie, J. (2012). Trends in Vegetation Dynamics and Impacts on Berry Productivity. In Nunavik and Nunatsiavut: From Science to Policy. An Integrated Reginal Impact Study (IRIS) of Climate Change and Modernization. ArcticNet Inc.

Lewkowicz, A.G. (2008). Evaluation of Miniature Temperature-Loggers to Monitor Snowpack Evolution at Mountain Permafrost Sites, Northwestern Canada. *Permafrost and Periglacial Processes*, 19: 323-331.

Lewkowicz, A.G., Etzelmüller, B., Smith, S. (2011). Characteristics of Discontinuous Permafrost based on Ground Temperature Measurements and Electrical Resistivity Tomography, Southern Yukon, Canada. *Permafrost and Periglacial Processes*, 22: 320-342.

Liston, G.E., McFadden, J.P., Sturm, M., Pielke Sr., R.A. (2002). Modelled Changes in Arctic Tundra Snow, Energy and Moisture Fluxes Due to Increased Shrubs. *Global Change Biology*, 8: 17-32.

Loke, M.H., Acworth, I., Dahlin, T. (2003). A Comparison of Smooth and Blocky Inversion Methods in 2D Electrical Imaging Surveys. *Exploration Geophysics*, 34: 182-187.

McClymont, A.F., Hayashi, M., Bentley, L.R., Christensen, B.S. (2013). Geophysical Imaging and Thermal Modeling of Subsurface Morphology and Thaw Evolution of Discontinuous Permafrost. *Journal of Geophysical Research: Each Surface*, 118: 1826-1837.

Myers-Smith, I.H. and Hik, D.S. (2013). Shrub Canopies Influence Soil Temperatures but Not Nutrient Dynamics: An Experimental Test of Tundra Snow-Shrub Interactions. *Ecology and Evolution*, 3(11): 3683-3700.

Nossov, D.R., Jorgenson, M.T., Kielland, K., Kanevskiy, M.Z. (2013). Edaphic and Microclimatic Controls Over Permafrost Response to Fire in Interior Alaska. *Environmental Research Letters*, 8: 035013.

Oberndorfer, E. (2020). What the Blazes!? A People's History of Fire in Labrador. *Journal of the North Atlantic*, 40: 1-16.

Payette, S., Fortin, M.J., Gamache, I. (2001). The Subarctic Forest-Tundra: The Structure of a Biome in a Changing Climate. *Bioscience*, 51(9): 709-718.

Pomeroy, J.W., Bewley, D.S., Essery, R.L.H., Hedstrom, N.R., Link, T., Granger R.J., Sicart, J.E., Ellis, C.R., Janowicz, J.R. (2006). Shrub Tundra Snowmelt. *Hydrological Processes*, 20: 923-941.

Pomeroy, J.W., Marks, D., Link, T., Ellis, C., Hardy, J., Rowlands, A., Granger, R. (2009). The Impact of Coniferous Forest Temperature on Incoming Longwave Radiation to Melting Snow. *Hydrological Processes*, 23: 2513-2525.

Revuelto, J., López-Moreno, J.I., Azorin-Molina, C., Vicente-Serrano, S.M. (2015). Canopy Influence on Snow Depth Distribution in a Pine Stand Determined from Terrestrial Laser Data. *Water Resources Research*, 51: 3476-3489.

Roberts, B.A., Simon, N.P.P., Deering, K.W. (2006). The Forests and Woodlands of Labrador, Canada: Ecology, Distribution and Future Management. *Ecological Research*, 21: 868-880.

Sharma, P.V. (1997). Environmental and Engineering Geophysics. Cambridge University Press.

Shur, Y.L. and Jorgenson, M.T. (2007). Patterns of Permafrost Formation and Degradation in Relation to Climate and Ecosystems. *Permafrost and Periglacial Processes*, 18: 7-19.

Sirois, L. and Payette, S. (1991). Reduced Postfire Tree Regeneration Along A Boreal Forest-Forest-Tundra Transect in Northern Quebec. *Ecology*, 2: 619-627.

Smith, S.L., Riseborough, D.W., Bonnaventure, P.P. (2015). Eighteen Year Record of Forest Fire Effects on Ground Thermal Regimes and Permafrost in the Central Mackenzie Valley, NWT, Canada. *Permafrost and Periglacial Processes*, 26: 289-303.

Sturm, M., McFadden, J.P., Liston, G.E., Chapin III, F.S., Racine, C.H., Holmgren, J. (2000). Snow-Shrub Interactions in Arctic Tundra: A Hypothesis with Climatic Implications. *Journal of Climate*, 14: 336-344).

Vu, V.Q. (2011). ggbiplot: A ggplot2 Based Biplot. R package version 0.55. https://github.com/vqv/ggbiplot.

Way, R.G. and Lewkowicz, A.G. (2015). Investigations of Discontinuous Permafrost in Coastal Labrador with DC Electrical Resistivity Tomography. In Proceedings of GeoQuébec 2015.

Way, R.G. and Lewkowicz, A.G. (2016). Modelling the Spatial Distribution of Permafrost in Labrador-Ungava Using the Temperature at the Top of Permafrost. *Canadian Journal of Earth Sciences*, 53: 1010-1028.

Way, R.G., Lewkowicz, A.G., Zhang, Y. (2018). Characteristics and Fate of Isolated Permafrost Patches in Coastal Labrador, Canada. *The Cryosphere*, 12: 2667-2688.

Wickham, H. (2016). ggplot2: Elegant Graphics for Data Analysis. Springer-Verlag New York. https://ggplot2.tidyverse.org.

Wilcox, E.J., Keim, D., de Jong, T., Walker, B., Sonnentag, O., Sniderhan, A.E., Mann, P., Marsh, P. (2019). Tundra Shrub Expansion May Amplify Permafrost Thaw by Advancing Snowmelt Timing. *Arctic Science*, 5: 202-217.

Wilke, C.O. (2019). cowplot: Streamlined Plot Theme and Plot annotations for ‘ggplot2’. R package version 1.0.0. https://cran.r-project.org/web/packages/cowplot/index.html.

Wotton, B.M., Nock, C.A., Flannigan, M.D. (2010). Forest Fire Occurrence and Climate Change in Canada. *International Journal of Wildland Fire*, 19: 253-271.

Zhang, Y., Wolfe, S.A., Morse, P.D., Olthof, I., Fraser, R.H. (2015). Spatiotemporal Impacts of Wildfire and Climate Warming on Permafrost Across a Subarctic Region, Canada. *Journal of Geophysical Research: Earth Surface*, 120: 2338-2356.

CHAPTER 5 : THERMAL MODELLING OF POST-FIRE PERMAFROST UNDER A WARMING COASTAL SUBARCTIC CLIMATE, EASTERN CANADA

Authors: Wang, Y.[1], Lewkowicz, A.G.[1], Holloway, J.E.[1], Way, R.G.[2]

Affiliations:

[1]Department of Geography, Environment and Geomatics, University of Ottawa

[2]Department of Geography and Planning, Queen's University

Authorship Attestation:

I am the primary author of this manuscript. The plan for field data collection was established by my supervisor, Dr. Antoni Lewkowicz, and myself. I collected the relevant field data during the summer 2018 and 2019 field seasons, with the assistance of and in collaboration with other members of the Food, Fire, and Ice research team. I collected soil samples in summer 2018 and 2019, and laboratory-based analyses were completed during the following fall semester. The modelling methodology was established through consultation with Dr. Antoni Lewkowicz, Jean Holloway, and Dr. Robert Way. I wrote the R code for the processing and visualization of the simulation outputs (Appendix B). This contribution was generated with guidance from Dr. Antoni Lewkowicz, Jean Holloway, and Dr. Robert Way.

5.1 Abstract

Forest fires have lasting thermal impacts on the underlying frozen ground in permafrost environments. These impacts are expected to continue to grow as the frequency and intensity of fire disturbance increases with climate change. This study implemented transient one-dimensional thermal modelling using the TEMP/W program to examine changes in the ground thermal regime at two coastal forest fire sites, located in the sporadic discontinuous permafrost zone near Nain (56.5°N) in Nunatsiavut, northern Labrador, Canada. To our knowledge, no previous studies of post-fire permafrost response and resilience have been conducted in the region. Simulations were undertaken for unburned forest and adjacent fire-disturbed sites, which were modelled to have permafrost thicknesses of 15.6-17.5 m in 1965. The simulations incorporated projected climate change modelled under Representative Concentration Pathways (RCPs) 4.5 and 8.5, as well as variation in the regeneration of the surface organic mat. In most scenarios, particularly those with post-fire organic mat regeneration, a supra-permafrost talik developed immediately following disturbance, but frozen ground re-aggraded after several decades before subsequently thinning. Results varied from permafrost thinning by 50% but persisting to 2099 at unburned sites under RCP4.5, to thawing entirely by 2060 when subjected to RCP8.5 and a high severity burn with no post-fire organic mat regeneration. Our findings are broadly consistent with those from climatically dissimilar sites in the western North American boreal forest and demonstrate that fire accelerates permafrost thaw due to climate warming. The results also confirm the importance of considering organic material accumulation in long-term modelling of permafrost change.

Key Words: Permafrost Degradation, Forest Fire, Talik, Organic Material Accumulation

5.2 Introduction

Forest fires are a widespread natural disturbance in many permafrost regions (Holloway et al., 2020). The loss of organic layer and canopy cover and the related changes in snow distribution and accumulation following fire have prolonged effects on the underlying frozen ground (Jorgenson et al., 2010). Long-term responses following fire are further complicated in the context of a changing climate (e.g., Zhang et al., 2015), especially given the amplified warming that is occurring in and projected for high latitude regions (Serreze and Barry, 2011; Meredith et al., 2019). The post-fire response of frozen ground is linked to changes in local hydrology and biogeochemistry, including the potential release of stored carbon from thawing soils (O'Donnell et al., 2011; Holloway et al., 2020). Organic material regeneration and permafrost re-aggradation following fire can minimize long-term post-fire carbon release (O'Donnell et al., 2011), but these processes are less likely to occur under a warming climate.

Thermal modelling is a well-established approach for predicting short- and long-term responses of frozen ground to surface disturbance. One-dimensional thermal modelling has been used in a number of studies of post-fire permafrost response within the North American boreal forest, but almost exclusively for subarctic sites in Alaska and the Northwest Territories (e.g., Jafarov et al., 2013; Nossov et al., 2013; Treat et al., 2013; Brown et al., 2015; Zhang et al., 2015). Here we employ thermal modelling to examine the impacts of forest fire on frozen ground at two sites near Nain, Nunatsiavut, in northern coastal Labrador (Figure 5-1). Field observations of climate and current frozen ground conditions at the sites (Chapter 4) are used to calibrate a model that explores frozen ground trajectories in a region with a wetter climate compared to northwest North America, resulting in longer forest fire intervals (Foster, 1983; Coops et al., 2018), a faster growth of a surface organic layer (Williams and Flanagan, 1998), and greater snow accumulation (Mudryk et al., 2015). The modelling also allows the sites to be classified according to Shur and Jorgenson's

(2007) conceptual classification of climate-ecosystem-permafrost interactions. We infer that the permafrost in the boreal forests of coastal Labrador was climate-driven when it formed, aided by the influence of the cold Labrador Current. Today, permafrost in most lowland locations of Nunatsiavut is thought to be ecosystem-protected, with persistence relating to the ecological protection offered by the current boreal forest cover. Classification of the frozen ground at our sites improves our understanding of the stability and resilience of permafrost in lowland forested locations in coastal Labrador.

5.3 Study Area and Sites

Labrador comprises the easternmost part of the Canadian Shield. The regional landscape is largely characterized by igneous and metamorphic bedrock, covered by a thin layer of frost-susceptible, fine-grained materials that were deposited during the retreat of the Laurentide Ice Sheet, from 12 to 6 k years BP (Dyke, 2004; Roberts et al., 2006; Bell et al., 2011).

The regional climate is strongly influenced by the Labrador Current that carries cold arctic waters southward along the Atlantic coast of Canada (Foster 1983; Banfield and Jacobs, 1998; Roberts et al., 2006). The resultant subarctic climate is characterized by long, cold winters and short, cool summers (Hare, 1950; Banfield and Jacobs, 1998). The mean annual air temperature (MAAT) at Nain is -2.5°C, mean annual total rainfall is 450 mm, and mean annual total snowfall is 475 cm (1981-2010 climate normal; Environment Canada, 2020). The community is located within the sporadic discontinuous permafrost zone according to the Permafrost Map of Canada (Heginbottom et al., 1995), a classification that is supported by more recent spatial modelling (Way and Lewkowicz, 2016).

In the central part of Nunatsiavut, the forest is composed of a mix of black spruce (*Picea mariana* [Mill.] B.S.P.), white spruce (*Picea glauca* [Moench] Voss), balsam fir (*Abies balsamea* [L.]

Mill.), and eastern larch (*Larix laricina* [Du Roi] K. Koch) (Roberts et al., 2006). The estimated fire interval of 1501 to 5000 years for this region (Coops et al., 2018) is much longer than the fire intervals of 75 to 200 years that are estimated for the western North American boreal forest (Foster, 1983). The greater fire rotation in this region permits the development of older, more structurally complex stands (Coops et al., 2018).

Our simulations investigate ground conditions at two sites near Nain, on a north-facing slope on the edge of Webb Bay (WB) and on a south-facing slope on the edge of Tikkoatokak Bay (TB) (Figure 5-1; Table 5-1).

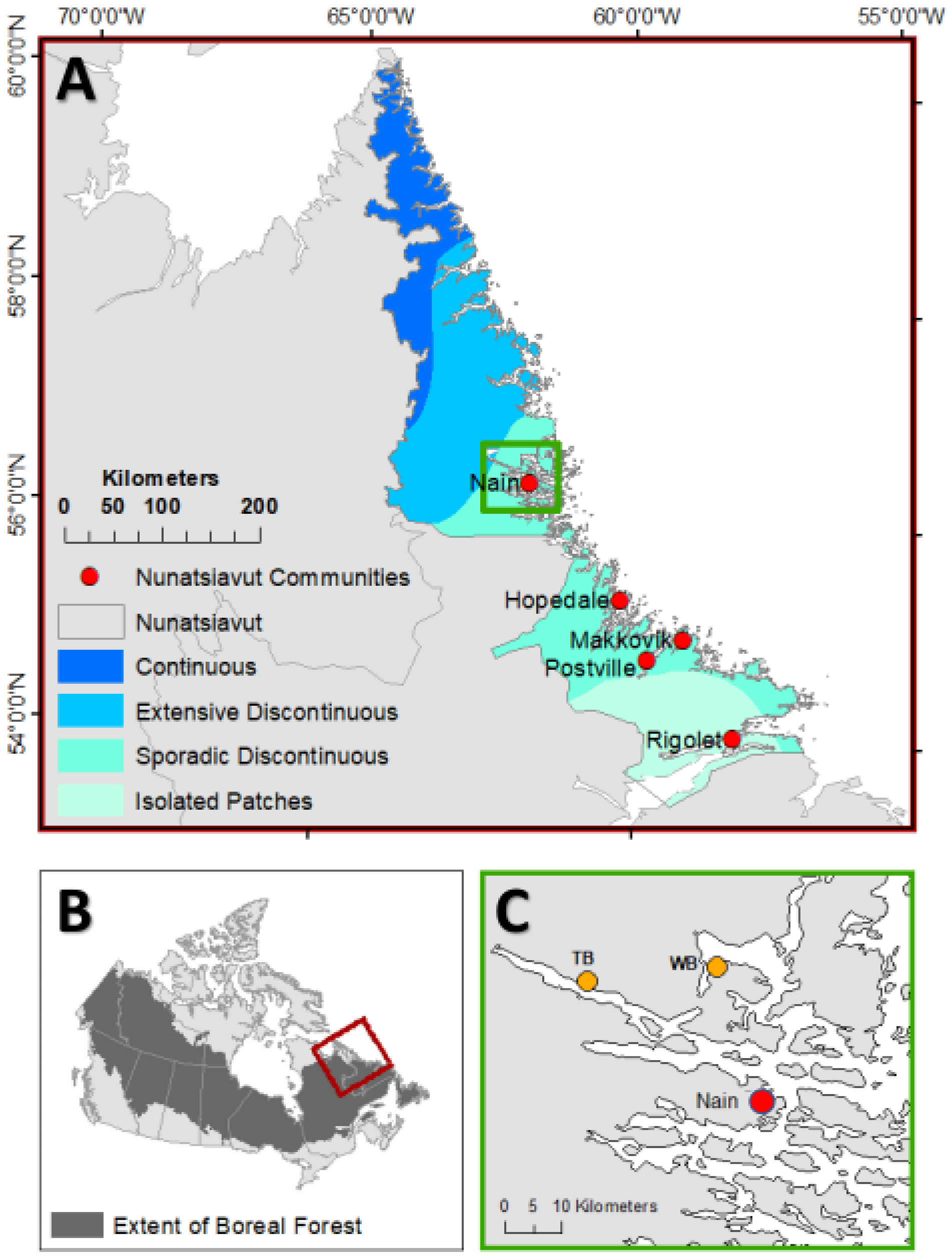

Figure 5-1. Location of Study Sites near Nain, Nunatsiavut (Crown-Indigenous Relations and Northern Affairs Canada, 2007). (A) Nunatsiavut communities and permafrost zones (Brown et al., 2002) (B) Coastal Labrador location in relation to the Canadian boreal forest (Brandt, 2009); (C) Webb Bay (WB) and Tikkoatokak Bay (TB) fire sites near Nain.

Table 5-1. Key Characteristics of the Study Sites. Climate variables are averaged for 2017-2019.

Variable	Webb Bay (WB)	Tikkoatokak Bay (TB)
Year of Burn	2004	2001
Approximate Size of Burn (km^2)	1	3
Latitude (°N)	56.706	56.755
Longitude (°W)	62.209	61.869
Elevation (m a.s.l.)	16	18
Aspect	North-facing	South-facing
Slope (°)	6	7
Forest Species Composition	Mixed black spruce, white spruce, tamarack, balsam fir	
Average Age of Forest (years)[a]	227	112
Mean Annual Air Temperature (°C)	-2.8	-2.7
Mean January Air Temperature (°C)	-19.9	-18.1
Mean July Air Temperature (°C)	9.5	11.2
Thawing Index (degree days)	1125	1177
Freezing Index (degree days)	2174	2163
Average Snow Depth Days (metre days)	166	154
Average Snow-on-Ground Season (days)	231	212

[a] as of 2018, from Brehaut and Brown (2020).

5.4 Modelling Parameters

Thermal modelling was undertaken with the TEMP/W (Geoslope) finite element, geothermal modelling software. TEMP/W has been applied in various infrastructure-related studies, including modelling of thermal change in roads (Darrow, 2011; Batenipour et al., 2013), around pipelines (Smith and Riseborough, 2010), and under buildings (Instanes, 2016; Perreault and Shur, 2016). This study is the first to use TEMP/W to investigate the effects of fire disturbance on frozen ground.

5.4.1. Profile and Material Properties

Site-specific one-dimensional idealised material profiles were developed, comprised of an upper organic layer, a layer of organo-mineral material, and a silty-sand layer over bedrock. The material stratigraphy and boundaries were estimated from field measurements of organic layer thickness, samples of near-surface soils, interpretations of sub-surface geophysical investigations (Chapter 4), and our understanding of the physical landscape of the region (Bell et al., 2011; Natural Resources Canada, 1957). Variability in the surficial materials and the stratigraphy at the sites was neglected to permit comparisons between other characteristics of the two sites and to obtain a general understanding of the impacts of climate warming, fire, and organic matter accumulation on the state of permafrost in the region.

The base of the model was set at a depth of 100 m, consistent with the model domain base used in other post-fire permafrost modelling simulations (Treat et al., 2013; Brown et al., 2015). Model mesh elements increased from 0.01 m in thickness in the organic layer to 1.5 m in the bedrock layer.

Materials were assumed to be saturated, as in McClymont et al. (2013) and Instanes (2016). The frozen and unfrozen thermal conductivities of each layer (Tables 5-2 and 5-3) were calculated using a geometric mean, based on the volumetric fractions and thermal conductivities of the material's constituents (Williams and Smith, 1989). Frozen and unfrozen heat capacities (Tables 5-2 and 5-3) were calculated using a weighted average, based on the volumetric fractions and heat capacities of the material's constituents (Johnston, 1981).

Table 5-2. Stratigraphy and Material Properties for the WB Site.

Material Layer	Depth (m)	Mineral Constituents	Dry Bulk Density (g/cm^3)	Porosity (%)	Volumetric Content (%)			Thermal Conductivity (W/m/K)		Heat Capacity ($MJ/m^3/K$)	
					Moisture	Organic	Mineral	Frozen	Unfrozen	Frozen	Unfrozen
Organic	0-0.2	-	0.170	0.839	0.839	0.161	-	1.568	0.525	1.983	3.919
Organo-Mineral	0.2-0.6	15% silt 85% sand	1.071	0.546	0.546	0.042	0.412	2.274	1.115	1.905	3.164
Upper Mineral	0.6-3	15% silt 85% sand	1.578	0.389	0.389	0.018	0.593	2.513	1.513	1.889	2.786
Lower Mineral	3-10	15% silt 85% sand	1.578	0.389	0.389	-	0.611	2.629	1.583	1.877	2.774
Bedrock	10-100	gabbro[a]	2.980	0.060	0.060	-	0.940	2.483	2.297	2.858	2.996

[a] bedrock was assumed to be gabbro, based on Atlas of Canada, 3rd Edition (1957).

Table 5-3. Stratigraphy and Material Properties for the TB Site.

Material Layer	Depth (m)	Mineral Constituents	Dry Bulk Density (g/cm^3)	Porosity (%)	Volumetric Content (%)			Thermal Conductivity (W/m/K)		Heat Capacity ($MJ/m^3/K$)	
					Moisture	Organic	Mineral	Frozen	Unfrozen	Frozen	Unfrozen
Organic	0-0.25	-	0.080	0.924	0.924	0.076	-	1.889	0.566	1.929	4.061
Organo-Mineral	0.25-0.6	35% silt 65% sand	1.068	0.823	0.823	0.024	0.153	2.205	0.754	1.895	3.793
Upper Mineral	0.6-3	35% silt 65% sand	1.548	0.401	0.401	0.018	0.581	2.508	1.486	1.889	2.814
Lower Mineral	3-10	35% silt 65% sand	1.548	0.401	0.401	-	0.599	2.621	1.553	1.877	2.802
Bedrock	10-100	gabbro[a]	2.980	0.060	0.060	-	0.940	2.483	2.297	2.858	2.996

[a] bedrock was assumed to be gabbro, based on Atlas of Canada, 3rd Edition (1957).

5.4.2 Boundary Conditions

Air temperature inputs were compiled from site-adjusted historical and projected daily air temperatures. The historical product was derived from the gridded Berkeley Earth Surface Temperature (BEST) analysis product, available through the KNMI Climate Explorer Database (climexp.knmi.nl/). The BEST record was selected because it is homogenized across an extensive meteorological data network, and it has a long record, extending back to 1880 (Rohde et al., 2013; Way and Viau, 2015). The site-specific historical record was developed using a linear model based on the temporal overlap between mean daily air temperatures from the BEST product and mean daily air temperatures at the sites, from summer 2017 to May 31, 2018. Mean daily air temperatures at WB and TB were calculated from measurements at two-hour intervals in the unburned forest by shielded Hobo Pro v2 Temperature/Relative Humidity U23-001 Data Loggers (Onset). There was a strong relationship between the BEST product and measured temperatures at the sites (WB: residual standard error=1.828 on 313 degrees of freedom, adjusted R^2=0.97, n=315; TB: residual standard error=1.889 on 292 degrees of freedom, adjusted R^2=0.97, n=294).

The projected daily air temperature estimates were averaged from a suite of four statistically downscaled climate scenarios (CanESM2, CESM1-CAM5, HadGEM2-ES, and MIROC-ESM) previously used in a study of Canadian wildfire activity throughout the 21st century (Hope et al., 2016). Model projections were compiled for a moderate representative concentration pathway (RCP4.5) and a more aggressive representative concentration pathway (RCP8.5; Moss et al., 2010). The composite projected daily temperature records under RCP4.5 and RCP8.5 were adjusted to the sites by applying daily anomalies to each day of the mean future daily air temperature record, from January 1, 2018 to December 31, 2099. Anomalies were applied based on an overlap period of 7 years between the climate scenarios and the site-specific BEST historical temperature record. These steps were performed to preserve the continuity of the air temperature record throughout the study period.

The ground-surface boundary temperatures in the model were generated by applying freezing (n_f) and thawing (n_t) n-factors to the air temperature record. N-factors are transfer functions that incorporate the effects of seasonal factors such as snow depth, snow density, and shading into air-ground temperature relations (Karunaratne and Burn, 2004; McClymont et al., 2013). An average of the n-factors measured at WB from 2017-2019 (Table 5-4) were used for 2018 in the modelling process at both sites. Measured n-factors for TB could not be averaged for 2017-2019 due to failure of ground surface temperature loggers in both burned and unburned locations for 2018-2019. Furthermore, the 2017-2018 ground surface temperature logger in the burned area was located 300 m away from the edge of the unburned forest and the other site observations (Chapter 4), so the resulting n-factors for the burned region for 2017-2018 did not correspond to the same location as the other site observations.

Table 5-4. N-Factors for the Burned and Unburned Sections of WB for 2017-2019. Model input n-factors for 2018 were averaged from measured n-factors for 2017-2018 and 2018-2019.

Region	Freezing n-Factor (n_f)			Thawing n-Factor (n_t)		
	Measured 2017-2018	Measured 2018-2019	Model Input	Measured 2017-2018	Measured 2018-2019	Model Input
Burned	0.12	missing[a]	0.12	0.84	missing[a]	0.84
Unburned	0.36	0.36	0.36	0.69	0.76	0.73

[a] freezing and thawing n-factors could not be calculated due to failure of ground surface temperature loggers during 2018-2019 season.

An extremely low geothermal heat flux (22 mW/m^2) was measured at the Voisey's Bay nickel mine about 50 km south of the study sites (Mareschal et al., 2000; Majorowicz and Minea, 2012). Such a low flux results in a correspondingly low geothermal gradient of about 1°C/80 m. This geothermal gradient could facilitate the development of thick permafrost, even if ground temperatures at the depth of zero annual amplitude are only just below 0°C. In the model, the geothermal heat flux value was increased to 220 mW/m^2 to avoid developing potentially unrealistically thick and cold permafrost. This value is still well below those employed in previous models of permafrost mounds in northern Québec (Buteau et al., 2004) and southern Labrador (Way et al., 2018).

5.4.3 Thermal Modelling Process

The TEMP/W model was run on half-hour time steps to reflect the diurnal nature of the daily air temperature data and to allow proper convergence at each step (GEO-SLOPE, 2004). During each of the 48 daily steps, the model was permitted to iterate up to 900 times, until convergence was achieved within 0.005 K. Some convergence issues arose at certain nodes, producing rapid changes in the position of the top of permafrost. The simulations in question were repeated several times, and the same spikes developed, suggesting that the instabilities are associated with the model solution itself. Convergence issues are quite common in permafrost modelling, but the overall resilient nature of frozen ground typically minimizes the effects of these instabilities in the final model output (Bao et al., 2016).

The thermal model was initialized with a spin-up period, in which ground conditions attained equilibrium with air temperatures from the 1950-1979 climate normal. A synthetic year of air temperatures, averaged across the 1950-1979 climate normal, was generated and repeatedly applied until equilibrium was achieved, defined as ground temperatures at every node varying by less than 0.01 K over 100 years. The model was then run forward in time using the site-specific BEST historical air temperature record, starting in 1965, marking the middle of the 1950-1979 climate normal period, through to the year of the fire and to the end of 2017. From 2018 onwards, site-specific air temperature projections under RCP4.5 or RCP8.5 were applied through to the end of 2099 (Figure 5-2).

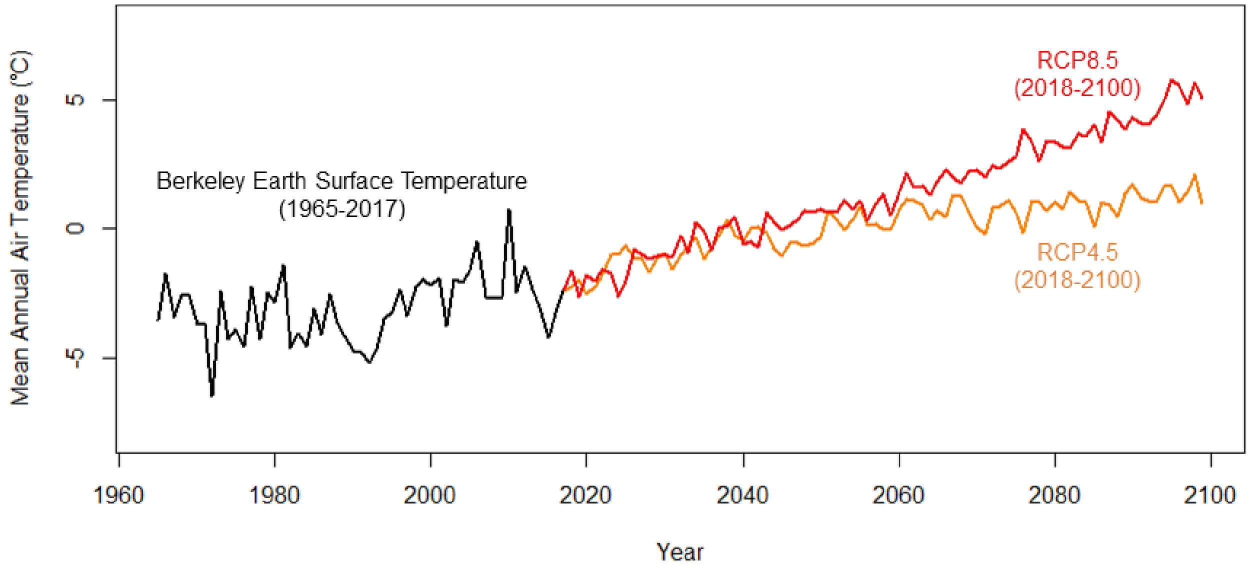

Figure 5-2. Mean Annual Values of Air Temperature Inputs for WB. Daily historical air temperatures (1965-2017) were assembled from a regional Berkeley Earth Surface Temperature record. Daily projected air temperatures (2018-2100) were averaged from statistically downscaled climate scenarios CanESM2, CESM1-CAM5, HadGEM2-ES, and MIROC-ESM under RCP4.5 and RCP8.5. The TB air temperature record is very similar and was assembled using the same method and temperature records.

Fire disturbance was represented in the model by an increase in n_t and a decrease in both n_f and organic layer thickness. These adjustments were applied as of August 1 in the year in which fire developed at each site because this is mid-way through the typical fire season in Labrador and the exact disturbance dates are not known. In 2001, the Labrador fire season lasted from May 18 to October 7, with the TB fire being just one of 23 reported fires in Labrador that year (Government of Newfoundland and Labrador, 2001a; Government of Newfoundland and Labrador, 2001b).

The reduction in organic layer thickness at the time of fire was 5 cm, corresponding to the low burn severity of the 2001 and 2004 events (Brehaut and Brown, 2020). Organic material was assumed to accumulate equally and linearly in both the burned and unburned parts of the sites. An organic material accumulation rate of 3.6 mm/year and 2.9 mm/year was applied to the WB and TB sites, respectively, based on estimations from current thicknesses measured in the field. These values are higher than the linear regeneration rate of approximately 2 mm/year calculated from a study of post-fire soil conditions in interior Alaska (Yi et al., 2010). The higher rates reflect the wetter climate of the coastal Labrador region, which promotes the productivity and growth of mosses that make up the upper portion of the organic layer (Williams and Flanagan, 1998).

Post-fire adjustments to n_f and n_t were applied with a two-segment linear model (Zhang et al., 2015). Vegetation regeneration to two-thirds of the pre-fire condition was assumed to take place in the first 25 years, followed by a second 25-year-period that ended at 100% of the pre-fire condition. Pre-fire n_f and n_t values of 0.36 and 0.73, respectively, were determined based on the measured values in the unburned region at the WB site over the 2017-2019 season (Table 5-4). These were applied to unburned scenarios for the entire modelling period. The n-factor values used through time for burned scenarios at WB are shown in Figure 5-3. The same pattern in post-fire n-factor change was applied to the TB site, except that the date of the fire was shifted to 2001, which permitted inter-site comparisons of the impacts of differences in climate, material properties, and stratigraphy. In order to achieve the measured n_f and n_t values in 2018 (Table 5-4) which represented partial recovery, the values immediately post-fire had to be set to the more extreme values shown in Figure 5-3.

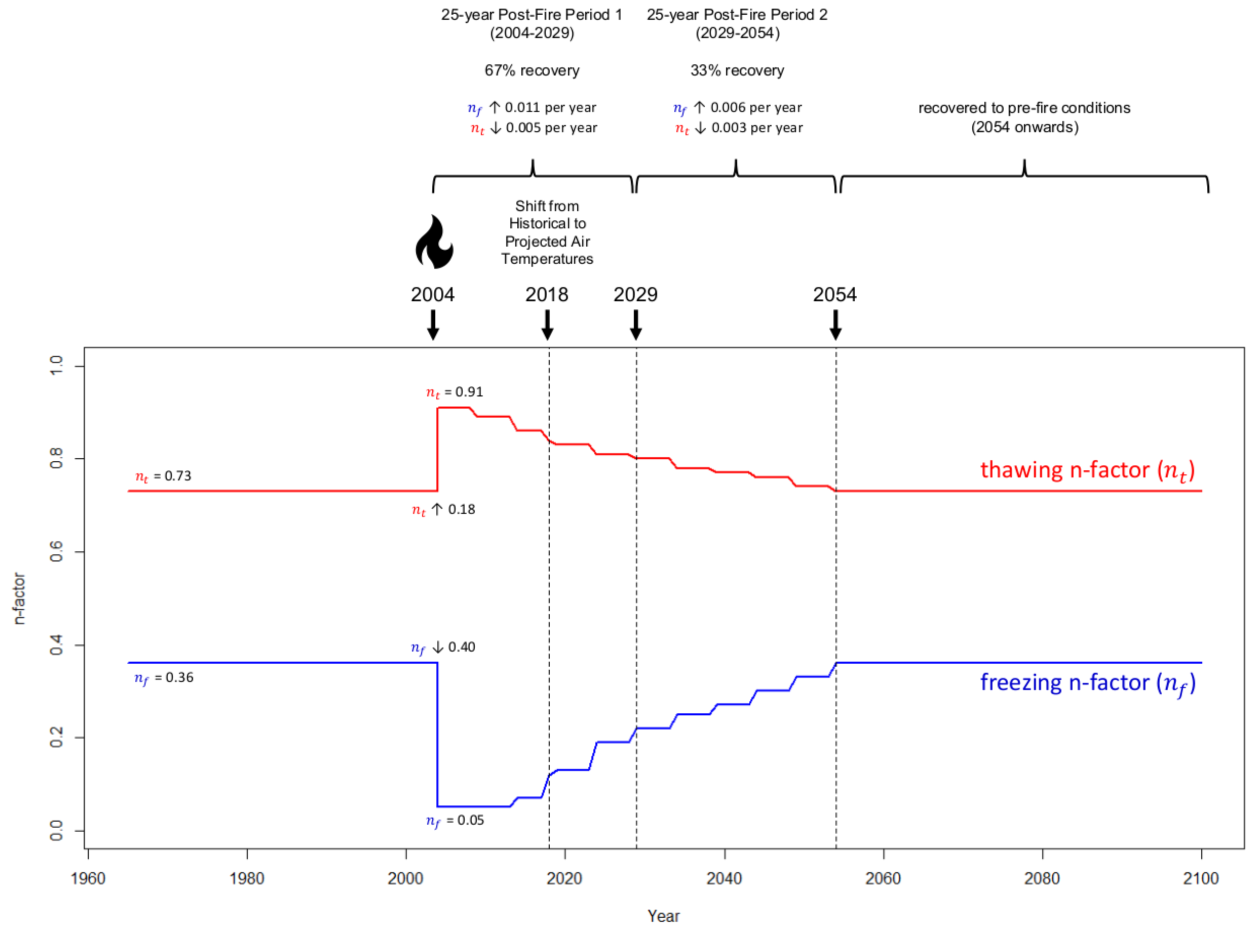

Figure 5-3. N-Factor Inputs for Burned Scenarios at the WB Site. Post-fire n-factor change was assumed to occur along a two-segment linear model (Zhang et al., 2015), from 2004 to 2054. N-factor inputs were applied in five-year model increments, except for the four-year run from 2014 to 2018 and the one-year run from 2018 to 2019, due to a shift from historical to projected air temperature inputs. The minimum freezing n-factor was set to 0.05.

5.4.4 Modelling Simulations

Four basic simulations were run for each site: 1) no disturbance under RCP4.5; 2) fire disturbance under RCP4.5; 3) no disturbance under RCP8.5; and 4) fire disturbance under RCP8.5. Eight additional simulations were produced for the WB site, in which sensitivity to the burn severity and the growth of the organic layer were evaluated (Table 5-5).

Table 5-5. Organic Layer Sensitivity Analyses.

Scenario Name	Climate Scenario	Burned/Unburned Scenario	Organic Layer Thickness (cm)		
			1965-2004	2004	2004-2099
WB_4.5_UNBURN_A	RCP4.5	UNBURNED	15	15	15
WB_4.5_BURN_A	RCP4.5	BURNED	15	10	10
WB_4.5_BURN_B	RCP4.5	BURNED	15	0	0
WB_4.5_BURN_C	RCP4.5	BURNED	15	0	accumulation of 3.6 mm/year
WB_8.5_UNBURN_A	RCP8.5	UNBURNED	15	15	15
WB_8.5_BURN_A	RCP8.5	BURNED	15	10	10
WB_8.5_BURN_B	RCP8.5	BURNED	15	0	0
WB_8.5_BURN_C	RCP8.5	BURNED	15	0	accumulation of 3.6 mm/year

5.4.5 Processing of Model Outputs

The TEMP/W modelling outputs were processed in R (Appendix B). The annual depth of zero annual amplitude, base of the active layer, top of the permafrost, and base of the permafrost were extracted from annual minimum, maximum, and mean temperature curves. From these parameters, it was possible to calculate the thickness of the active layer, the thickness of the permafrost, and the thickness of a talik, if present, for each year within the modelling period. However, the pattern of these values through time showed significant discontinuities in some model runs when a temperature of 0°C was used as a threshold because temperature gradients were very small. Consequently, results are presented using a temperature scale focussed on the temperatures around 0°C and linked to the unfrozen moisture content defined within the model. The ground is portrayed as frozen (dark blue; <-0.005°C: <32% unfrozen moisture content), partially frozen (light blue; between -0.005°C and 0°C: 32.01-99.99% unfrozen moisture content), or unfrozen (light and dark red; >0°C: 100% unfrozen moisture content).

5.5 Results

5.5.1 Model Output Validation

Validation of the model was undertaken using surface temperatures, as boreholes were not established at the study sites. The modelled annual average surface temperature was 0.41°C higher in the unburned region (root mean square error of 2.53°C) and 0.13°C higher in the burned region (root mean square error of 2.20°C) when compared to field measurements from July 2017 to 2018 (Figure 5-4). The greatest difference between modelled and measured ground surface temperatures was in late-winter and spring, when field values are affected by the thick snowpack that dampens diurnal variations and creates a long period at 0°C during snowmelt, which is not reproduced in the model. The difference between modelled and measured results in spring 2018 may also relate to the shift from historical to projected air temperature inputs on January 1, 2018. The projected air temperature record is presented under a moderate warming scenario, RCP4.5, and may produce slightly warmer ground surface temperatures during this period.

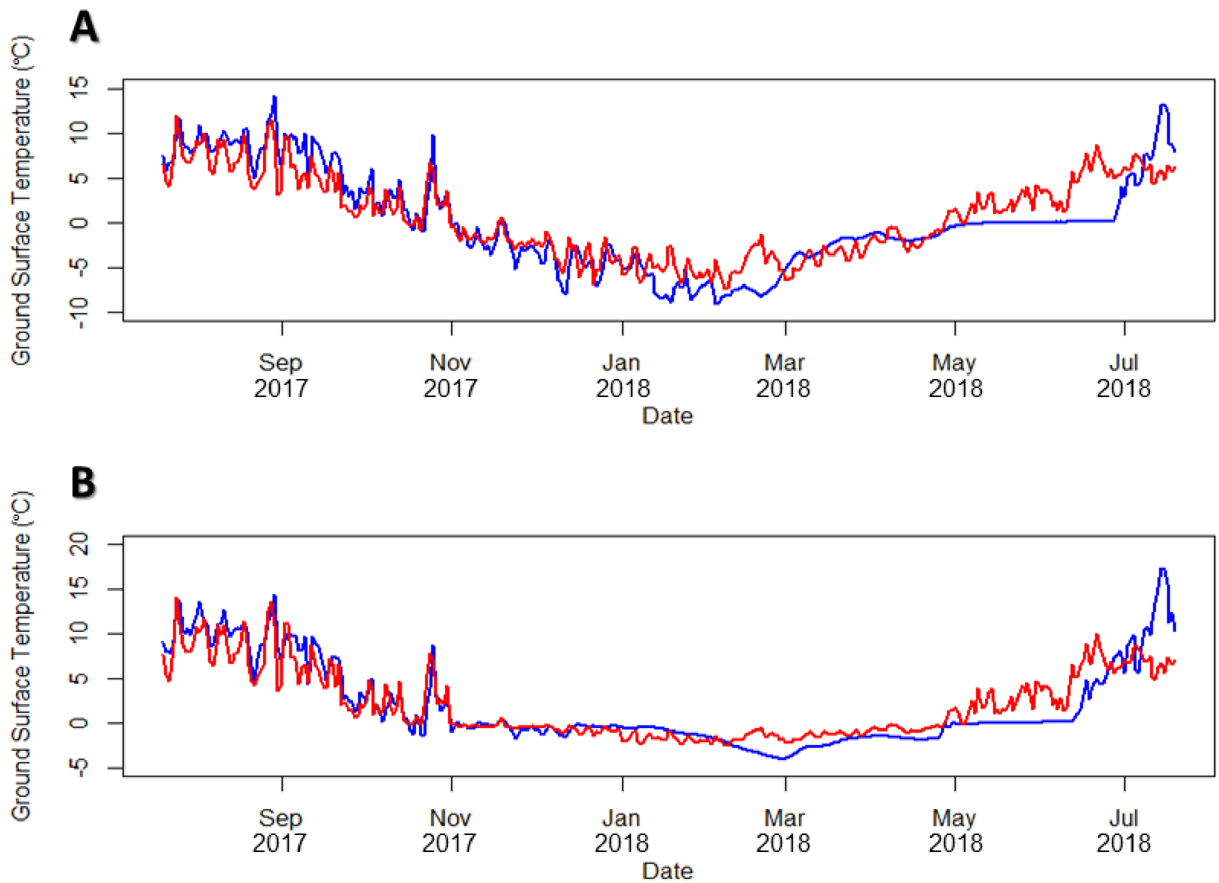

Figure 5-4. Comparison of Modelled (red) and Measured (blue) Ground Surface Temperatures in the A) Unburned Region and B) Burned Region at the WB Site from July 20, 2017 to July 19, 2018.

5.5.2 Pre-Fire Permafrost Conditions

All the models ran with the same boundary conditions from 1965 to the time of fire (if applicable) or the start of the applied climate warming scenario (2018). The models predict a 15.6 m-thick body of permafrost at the WB site in 1965 and a 17.5 m-thick body of permafrost at the TB site for the same year. Over the next 35 to 40 years, permafrost temperatures at both sites remain warm, with average values at the depth of zero annual amplitude of -0.50°C (WB) and -0.62°C (TB) and standard deviations for the entire period of approximately 0.10°C. A local maximum in permafrost thickness and a corresponding local minimum in the temperature of permafrost occurs in 1995 (Figure 5-5), corresponding to the end of a period of regional climatic cooling (Way and Viau, 2015; Figure 5-2).

5.5.3 Impact of Climate Warming

Under RCP4.5, frozen ground persists to the end of this century in the unburned regions of both sites. In 2099, the thickness of the permafrost at the WB site is predicted to be 8.2 m, or 52% of its thickness in 1965 (Figures 5-5 and 5-7; Table 5-6), while at the TB site, it is 8.8 m, or 50% of its initial thickness. No taliks are initiated, and the active layer does not notably change in thickness as organic mat accumulation offsets the impact of the warming climate. From the start of the RCP4.5 scenario in 2018 to the end of the study period, the temperature of permafrost increases linearly at rates of approximately 0.004°C per year and 0.003°C per year at WB and TB, respectively. Under RCP8.5, however, a climate-initiated talik develops in the 2060s at WB (Figures 5-6 and 5-7) and in the 2070s at TB. This is also reflected in the temperature at the depth of zero annual amplitude, which rapidly approaches and eventually exceeds 0°C in the latter half of the century. The active layer, now defined by the depth of seasonal freezing, becomes thinner through time. The talik deepens through the remainder of the century, but a thin layer of permafrost persists beyond 2100 in the unburned regions of both sites (Table 5-6).

Table 5-6. Description and Results of Modelling Simulations Performed in TEMP/W.

Site	Simulation Name	Climate Scenario	Unburned or Burned (Low or High Severity) Scenario	Organic Layer Accumulation	Fire-Initiated Talik			Climate-Initiated Talik	Year of Loss of Permafrost	Permafrost Thickness Remaining in 2099 (m)
					Year of Initiation	Year of Recovery	Duration (Years)	Year of Initiation		
Unburned Region, Moderate Warming Scenario										
WB	WB_4.5_UNBURN	RCP4.5	UNBURNED	YES	-	-	-	-	2100+	8.1
WB	WB_4.5_UNBURN_A	RCP4.5	UNBURNED	NO	-	-	-	2082	2100+	4.9
TB	TB_4.5_UNBURN	RCP4.5	UNBURNED	YES	-	-	-	-	2100+	8.8
Unburned Region, Aggressive Warming Scenario										
WB	WB_8.5_UNBURN	RCP8.5	UNBURNED	YES	-	-	-	2063	2100+	0.6
WB	WB_8.5_UNBURN_A	RCP8.5	UNBURNED	NO	-	-	-	2059	2095	-
TB	TB_8.5_UNBURN	RCP8.5	UNBURNED	YES	-	-	-	2076	2100+	2.3
Burned Region, Moderate Warming Scenario										
WB	WB_4.5_BURN	RCP4.5	BURNED (LOW)	YES	2004	2034	30	-	2100+	3.6
TB	TB_4.5_BURN	RCP4.5	BURNED (LOW)	YES	2001	2032	31	-	2100+	5.4
WB	WB_4.5_BURN_A	RCP4.5	BURNED (LOW)	NO	2004	2046	42	2062	2082	-
WB	WB_4.5_BURN_C	RCP4.5	BURNED (HIGH)	YES	2004	2044	40	2094	2100+	2.2
WB	WB_4.5_BURN_B	RCP4.5	BURNED (HIGH)	NO	2004	2047	43	2051	2066	-
Burned Region, Aggressive Warming Scenario										
WB	WB_8.5_BURN	RCP8.5	BURNED (LOW)	YES	2004	2044	40	2062	2080	-
TB	TB_8.5_BURN	RCP8.5	BURNED (LOW)	YES	2001	2034	33	2073	2085	-
WB	WB_8.5_BURN_A	RCP8.5	BURNED (LOW)	NO	2004	-	65	-	2069	-
WB	WB_8.5_BURN_C	RCP8.5	BURNED (HIGH)	YES	2004	-	65	-	2069	-
WB	WB_8.5_BURN_B	RCP8.5	BURNED (HIGH)	NO	2004	-	56	-	2060	-

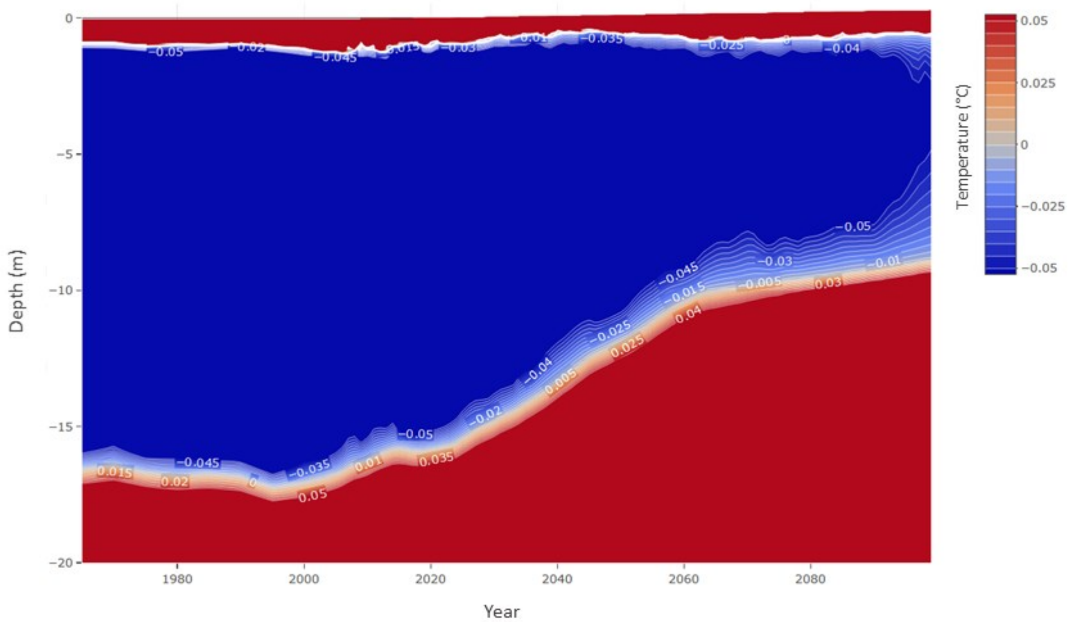

Figure 5-5. Modelled Ground Temperatures (1965-2099) at the Unburned WB Site Under RCP4.5. Organic material accumulated at 3.6 mm/year from 2004 to 2099. The base of the active layer, approximated by a temperature threshold of -0.025°C or an unfrozen moisture content of 0.11, is shown as a white line.

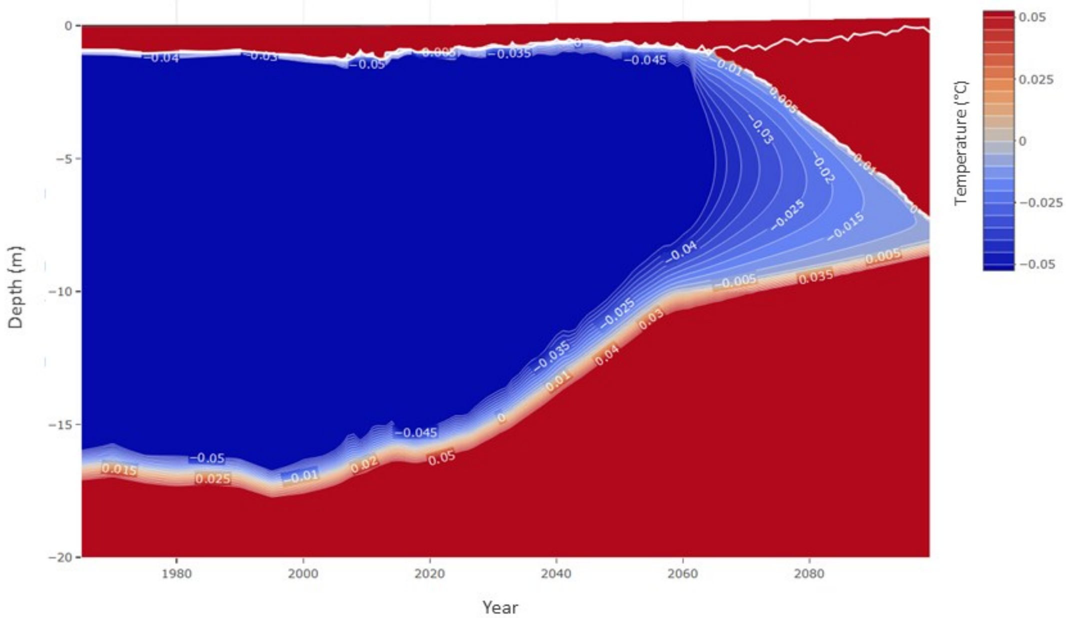

Figure 5-6. Modelled Ground Temperatures (1965-2099) at the Unburned WB Site Under RCP8.5. Organic material accumulated at 3.6 mm/year from 2004 to 2099. The base of the active layer, approximated by a temperature threshold of -0.025°C or an unfrozen moisture content of 0.11, is shown as a white line.

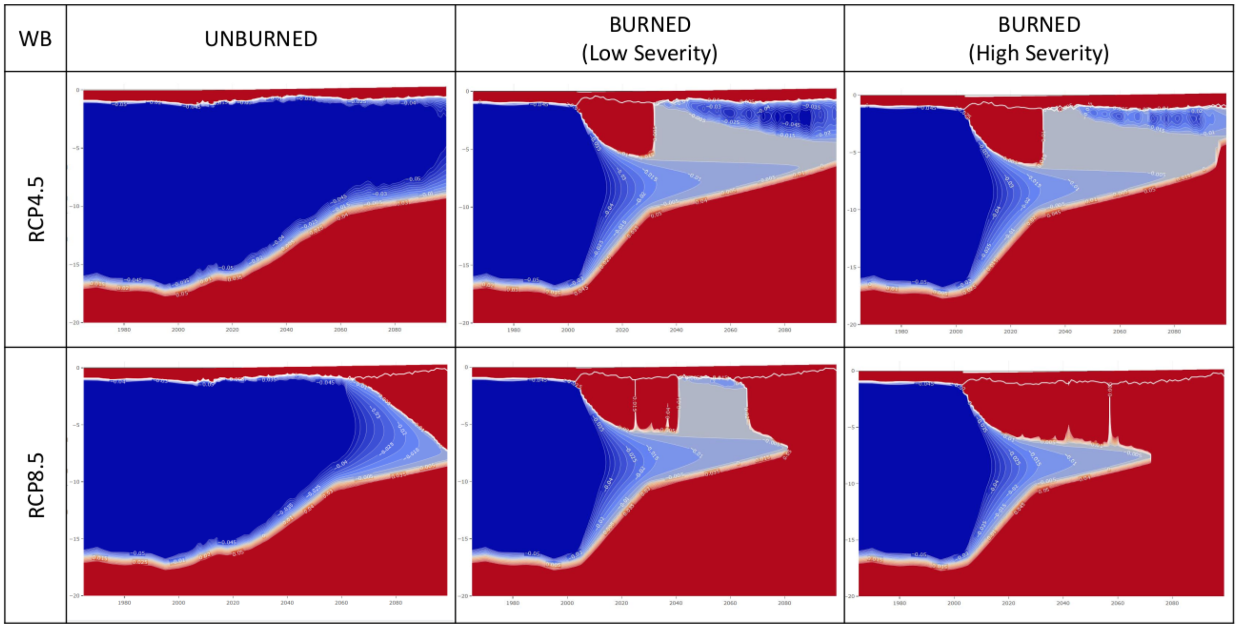

Figure 5-7. Summary of Results of Selected Modelling Simulations in TEMP/W. Simulations with organic material accumulation at WB are presented to facilitate comparisons between simulations.

5.5.4 Impact of Fire

Fire disturbance triggers talik development in all burned scenarios (Figures 5-7, 5-8, 5-9, and 5-10). The base of the perennially unfrozen ground advances rapidly into the underlying permafrost at first, but gradually slows until the talik reaches a maximum thickness of 5 to 6 m. The active layer thickness, defined by the depth of seasonal freezing, initially thins, but this trend subsequently reverses once the talik refreezes. After several decades, the permafrost aggrades, causing the talik to close and the temperature at the depth of zero annual amplitude to decrease. During this re-aggradation process, particularly for the TB site, the ground temperatures approach or reach similar values to those measured during the pre-fire period. Under RCP4.5, as of the mid-2090s, the temperature at the depth of zero annual amplitude is the same for both burned and unburned scenarios. By the end of the century, under RCP4.5 and with low burn severity, a 4 to 5 m-thick layer of permafrost is predicted to remain under the burned regions at both sites (Table 5-6).

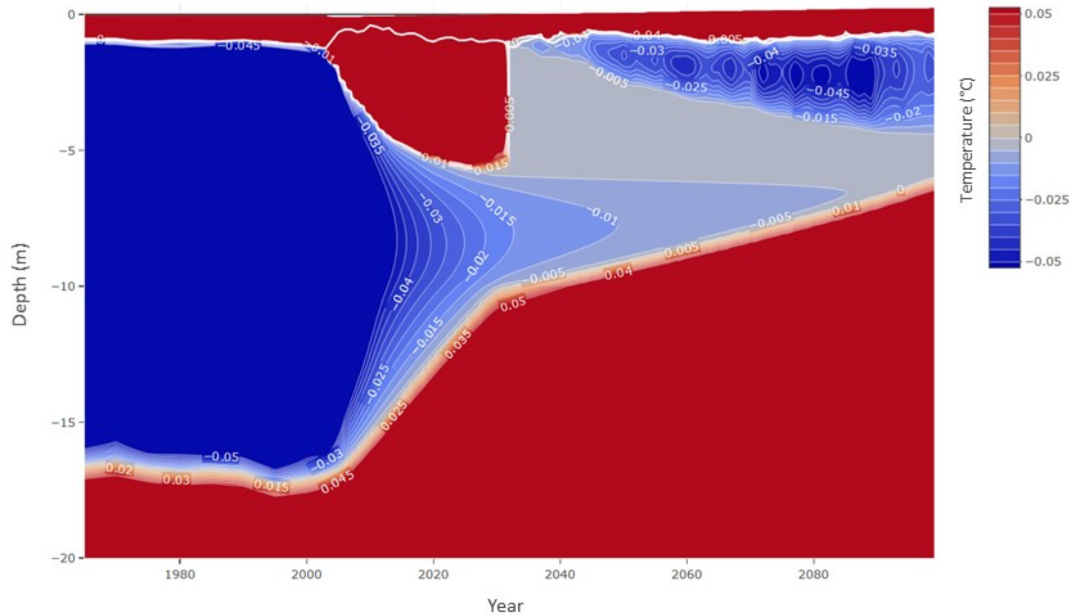

Figure 5-8. Modelled Ground Temperatures (1965-2099) Following Low Burn Severity Fire in 2004 at the WB Site Under RCP4.5. Organic material accumulated at 3.6 mm/year from 2004 to 2099. The base of the active layer, approximated by a temperature threshold of -0.025°C or an unfrozen moisture content of 0.11, is shown as a white line.

5.5.5 Combined Impact of Fire and Climate Warming

The combined impacts of fire disturbance and aggressive climate warming result in the development of two taliks and the complete loss of frozen ground at both sites by the mid-2080s. The first talik is initiated immediately following fire, and the thaw front continues to advance at its base for approximately two decades, after which there is a 20-year period of stability until refreezing begins from the active layer downwards (Figures 5-7 and 5-9). The soil between the active layer and the permafrost beneath the talik partially refreezes but subsequently thaws completely.

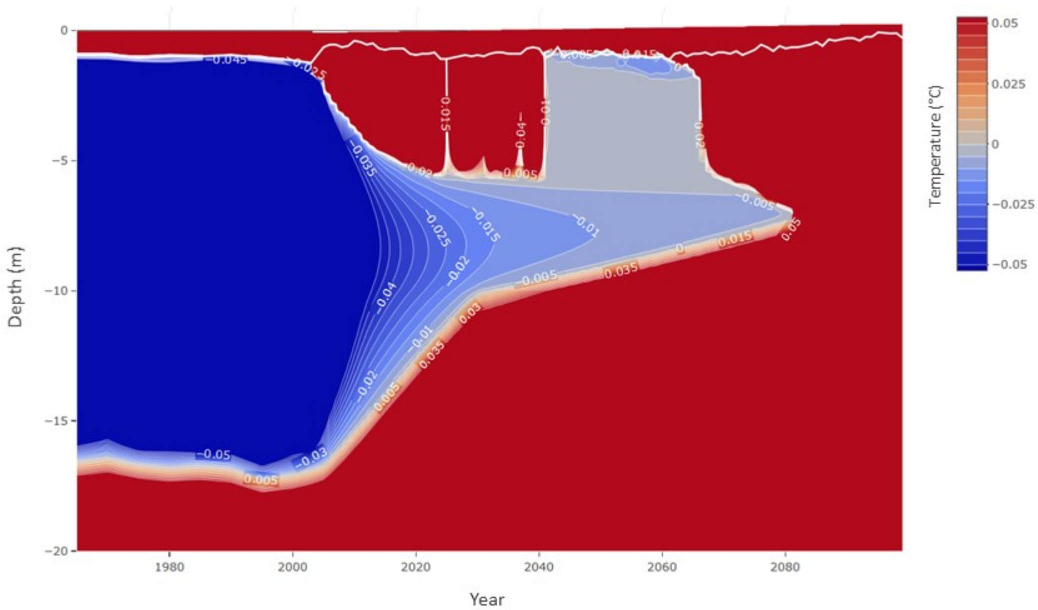

Figure 5-9. Modelled Ground Temperatures (1965-2099) Following Low Burn Severity Fire in 2004 at the WB Site Under RCP8.5. Organic material accumulated at 3.6 mm/year from 2004 to 2099. The base of the active layer, approximated by a temperature threshold of -0.025°C or an unfrozen moisture content of 0.11, is shown as a white line.

5.5.6 Impact of Burn Severity

High burn severity simulations were run for WB to evaluate responses in locations where the entire organic mat was burned, but subsequently redeveloped, under both moderate and aggressive warming scenarios. The fire-initiated talik that forms under RCP4.5 takes a full decade longer to recover than the talik formed in the low burn severity simulation. However, permafrost is still present at the end of the century (Table 5-6). Under RCP8.5, permafrost does not re-aggrade at all following a high burn severity fire, and all frozen ground is lost by 2069 (Figures 5-7 and 5-10). This occurs 11 years sooner than in the low burn severity simulation under RCP8.5.

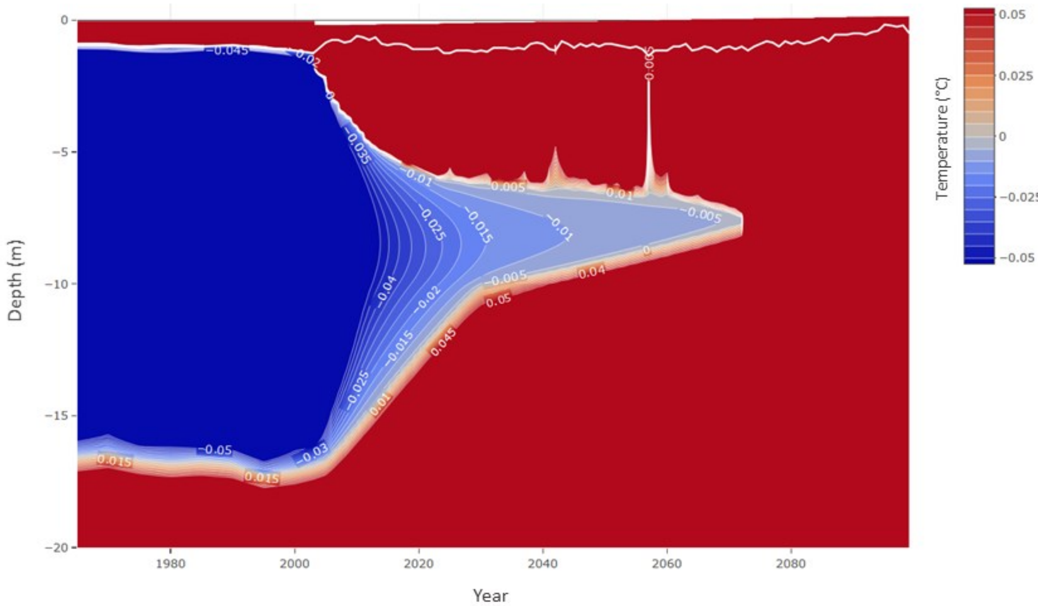

Figure 5-10. Modelled Ground Temperatures (1965-2099) Following High Burn Severity Fire in 2004 at the WB Site Under RCP8.5. Organic material accumulated at 3.6 mm/year from 2004 to 2099. The base of the active layer, approximated by a temperature threshold of -0.025°C or an unfrozen moisture content of 0.11, is shown as a white line.

5.5.7 Impact of Surface Organic Matter Accumulation

Six simulations in which organic matter does not accumulate were produced for WB. They result in thaw from the surface downwards in unburned scenarios under both RCP4.5 and RCP8.5. Under RCP4.5, a climate-initiated talik forms in 2082, which deepens linearly so that only 4.9 m of permafrost remains in 2099 (Table 5-6). Under RCP8.5, a climate-initiated talik begins to form in 2059, 4 years before the talik in the simulation with organic layer accumulation, and there is complete loss of permafrost by 2095 (Table 5-6).

Omitting surface organic matter accumulation results in the total loss of permafrost by the end of the century under both moderate and aggressive climate warming and low and high burn severity simulations. Under RCP4.5, the low burn severity simulation, in which the organic layer decreases by 5 cm, shows loss of all frozen ground by 2082 (Table 5-6). The high burn severity simulation, with no organic material following fire, results in loss of frozen ground by 2066 (Table

5-6). Under RCP8.5, the fire-initiated talik does not refreeze, and all permafrost thaws by 2069 and 2060, under low and high burn severity scenarios, respectively (Table 5-6).

5.6 Discussion

Permafrost vulnerability in black spruce stands in the western North American boreal forest has been described as a combination of (1) permafrost resilience, which relates to the initial development of the permafrost, and (2) permafrost exposure, which can be influenced by climate change and fire disturbance (Jafarov et al., 2013). Here we assess the vulnerability of the permafrost in our boreal forest sites near Nain.

The resilience of the permafrost near Nain relates to its categorization within the climate-ecosystem-permafrost scheme defined by Shur and Jorgenson (2007). Prior to fire disturbance, the permafrost at these sites is interpreted as being climate-driven, ecosystem-protected, reflecting the initial climate-driven formation process, aided by the influence of the cold Labrador Sea current, and the canopy protection offered by the surrounding undisturbed boreal ecosystem (Figure 5-10). This classification is validated by refreezing of the fire-initiated taliks at the two sites in all scenarios in which organic material accumulates. However, the permafrost aggradation process that occurs following talik recovery is no longer climate-driven. Instead, this process is ecosystem-driven by the post-fire accumulation of organic material and the gradual regeneration of the surrounding canopy cover (Figure 5-10). Ecosystem-driven permafrost can become ecosystem-protected as post-fire ecosystem succession progresses, particularly under a continually warming climate (Shur and Jorgenson, 2007; Figure 5-10). Under RCP8.5, climate warming overcomes the ability of the ecological components of the ecosystem to protect the permafrost, resulting in the development of a second, climate-initiated talik that leads to complete loss of perennially frozen ground.

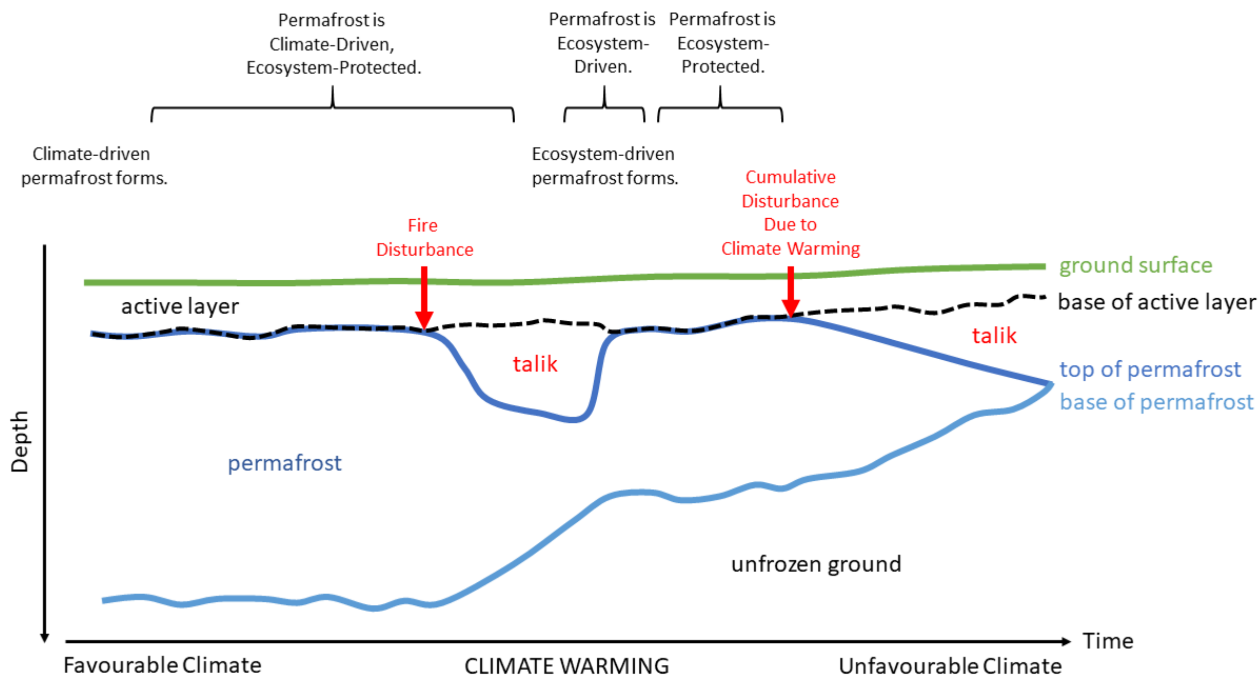

Figure 5-11. Schematic Showing Changes to Permafrost Classification (defined by Shur and Jorgenson, 2007) Following Fire and Under A Warming Climate. The two arrows show the times when the two disturbances are sufficient to thaw the upper layers of permafrost. The schematic is based on the post-fire trajectory of permafrost, modelled under an aggressive climate warming scenario (RCP8.5) with post-fire organic material accumulation. Note that depth is not to scale.

Permafrost exposure is linked to both fire disturbance and climate warming (Jafarov et al., 2013). Our modelling results agree with previous studies that have demonstrated that fire acts to accelerate the ultimate and inevitable loss of permafrost (e.g., Zhang et al., 2015; Gibson et al., 2018; Holloway et al., 2020). Under the same climate scenario, the burned simulations result in thinner and warmer permafrost that thaws out more quickly than the perennially frozen ground in unburned simulations. Under RCP4.5, by 2100, low and high severity fire disturbances at WB result in respective permafrost thicknesses that are 56% and 73% thinner than the 8.1 m of permafrost remaining in the undisturbed simulation. In the Northwest Territories, forest fires are estimated to accelerate the loss of permafrost by an average of 8 years (Zhang et al., 2015). Loss of permafrost following fire disturbance at our sites in coastal Labrador is modelled to occur three to four times faster than in the Northwest Territories, but this is likely due to the higher temperatures and lower ground ice contents (i.e., lower latent heat) of the permafrost at our sites compared to those in the central Northwest Territories (Smith et al., 2015).

Our results demonstrate that climate warming can influence both permafrost resiliency and exposure, as defined by Jafarov et al. (2013). The classification of permafrost conditions at an individual site evolves as the climate warms (Shur and Jorgenson, 2007). As the climate becomes unfavourable for further aggradation, climate-driven, ecosystem-protected permafrost may become ecosystem-protected. This change has implications for the post-disturbance resiliency of the permafrost, as post-fire aggradation and recovery occurred more rapidly following fires that burned in the 20th Century under cooler climate conditions (Zhang et al., 2015). Following fire, climate-driven, ecosystem-protected permafrost can re-aggrade, while ecosystem-protected permafrost is expected to thaw out. The WB and TB fires occurred within three years of one another, so the difference in fire dates should not have had a notable impact on the thermal response of the ground, especially since the mean annual air temperatures were quite similar, at -1.5°C in 2001 and -1.7°C in 2004. However, if a fire were to occur later in this century at the same sites, it is unlikely that the fire-initiated taliks in the ecosystem-protected permafrost would recover. The development of climate-initiated taliks in the latter half of this century under RCP8.5 reflects the sensitivity of the permafrost at the sites to the cumulative impacts of climate warming. The constant, gradual warming that is applied to the simulations results in the initiation of taliks that deepen more linearly than those initiated by fire disturbance. Fire-initiated taliks develop in the immediate post-fire period due to the sudden and cumulative effects of increased heat penetration in summer and decreased heat loss in winter (Gibson et al., 2018). However, post-fire talik development eventually slows as the ecosystem recovers from the disturbance (Yoshikawa et al., 2003; Gibson et al., 2018). In contrast, permafrost degradation due to climate warming occurs much more steadily and gradually.

5.6.1 General Post-Fire Permafrost Response

Our simulations present thinning of the active layer following fire, despite reports of post-fire active layer thickening in other forested sites throughout the Arctic (Jafarov et al., 2013; Zhang et al., 2015; Fisher et al., 2016; Gibson et al., 2018). With the post-fire development of a talik, the definition of the active layer changes from the layer of seasonally thawed ground over permafrost (i.e., the maximum depth of summer thaw), to the layer of seasonally frozen ground over a talik (i.e., the maximum depth of winter freezing). It can be very difficult to differentiate between an active layer and a talik through field-based methods, which may explain why active layer thickening is often reported in post-fire field investigations.

The patterns of permafrost thaw at our sites agree with those of a previous study in the Northwest Territories that concluded that fire disturbance can trigger thawing of permafrost from the base, particularly in forested regions (Zhang et al., 2015). Despite the relatively high geothermal heat flux that was applied to the base of our model domain, the post-fire persistence of permafrost at the WB and TB sites speaks to the resiliency of frozen ground in the region at present.

Simulations in which surface organic material accumulation was omitted caused permafrost to degrade much more rapidly, since the constant organic layer failed to offset the impacts of the increasing air temperatures over time. The organic layer is largely responsible for the thermal offset, which is especially crucial for permafrost persistence under unfavourable climate conditions, such as those represented by RCP4.5 and RCP8.5, and following surface disturbance (e.g., forest fire; Shur and Jorgenson, 2007). Our results support previous findings of the importance of accounting for organic material accumulation in post-fire permafrost modelling studies (Zhang et al., 2015).

5.6.2 Impact of Simplified Model Inputs

The modelling results for TB do not fully reflect site conditions since, as mentioned above, n_t and n_f were those measured at WB. Climatic differences between the sites were addressed by site-specific air temperature records, but applying the same n-factors and their changes through time implies the same snow and shading characteristics, which is incorrect (Chapter 4). However, by using the same n-factors, the sensitivity of the model to differences in soil moisture and sediment composition (more silt and less sand at TB; Tables 5-2 and 5-3) emerge. Even though the climate is slightly warmer at TB, its material properties resulted in thicker and colder permafrost and more rapid talik recovery than at WB (Table 5-6). Thermal property differences between the sites included higher latent heats, due to greater volumetric moisture contents, and greater ratios of frozen to thawed thermal conductivities in the top 10 m of the profile at TB, corresponding to surficial deposits. Higher latent heats help to limit talik development and promote permafrost recovery following fire, providing thaw settlement does not cause ponding (Jorgenson et al., 2010).

Other modelling simplifications included prescribed n-factors. N-factors can vary over short time periods and distances (Karunaratne and Burn, 2003; Karunaratne and Burn, 2004), and n_f is especially dynamic due to its sensitivity to inter-annual differences in snow cover, distribution, and density (Karunaratne and Burn, 2003; Karunaratne and Burn, 2004). N_f can also be impacted by the presence or absence of permafrost, due to the release of latent heat during the freezing of the active layer in the fall (Riseborough and Smith, 1998; Karunaratne and Burn, 2004). Reducing n_f in years in which a talik was present could have delayed the recovery of the talik and further accelerated the loss of permafrost, but this was not done because an appropriate adjustment is not known. A lack of reliable snow accumulation models for the coastal Labrador region prevented the incorporation of dynamic n_f values into the simulations, but future simulations would likely be improved by such an addition.

Post-fire variations in soil moisture, which typically relate to the thickness of remaining organic material (Kasischke and Johnstone, 2005), were also not considered. In many cases, especially in lowland sites, post-fire soil moisture is expected to increase, due to thickening of the active layer, poor drainage, and reduced evapotranspiration (Nossov et al., 2013). However, as the site recovers from the fire disturbance, soil moisture is eventually expected to return to or approach pre-fire conditions. With only instantaneous field-based soil moisture measurements and little reliable validation, we chose not to incorporate dynamic post-fire soil moisture in our modelling process. Future simulations, coupling TEMP/W with SEEP/W, to model the lateral and/or vertical flow of water, could provide further insight into how post-fire soil moisture changes might influence soil freezing properties and characteristics.

5.7 Conclusions

The current and historical climate of our field sites near Nain differ from locations in western North America where most of the existing research on forest fires and permafrost has been carried out. The sites are wetter, accumulate a deeper winter snowpack, and long-term air temperature trends began to increase later than in the West. Despite these differences, our one-dimensional thermal modelling supports the general understanding that fire disturbance, and its associated reduction in organic material thickness and canopy cover, is responsible for accelerating the inevitable loss of permafrost due to climate warming. In the context of the climate-ecosystem-permafrost classes defined by Shur and Jorgenson (2007), the classification of the permafrost at our sites in coastal Labrador changes from climate-driven, ecosystem-modified permafrost prior to fire, to ecosystem-driven permafrost following fire, to ecosystem-protected permafrost prior to complete loss of permafrost due to climate warming. Despite the degradational effects of climate warming and fire disturbance, permafrost persists to at least 2060 and, in many cases, through to the end of this century.

5.8 Acknowledgements

We thank the Nunatsiavut Government for permission to conduct research on the traditional lands of the Labrador Inuit (Permit #9222380). Funding for this research was provided by Polar Knowledge Canada (PI: Carissa Brown) and the Northern Scientific Training Program, and Y. Wang acknowledges financial support from the W. Garfield Weston Foundation and the Natural Sciences and Engineering Research Council of Canada. We would like to thank the Nunatsiavut Research Centre and the Labrador Institute of Memorial University for logistical and in-kind support, and we gratefully acknowledge Frédéric Dwyer-Samuel, Luise Hermanutz, Alain Cuerrier, Caitlin Lapalme, Harold Goudie, Shirley Goudie, Jim Goudie, Gillian Gear, Ches Webb, Joe Webb, William Ikkusek, Edward Sillett, Carla Pamak, Liz Pijogge, Paul McCarney, and Rodd Laing for their collaboration and support of our field investigations. We are grateful to Sai Vanapalli and Konrad Gajewski for their generous access to the required modelling resources.

5.9 References

Banfield, C.E. and Jacobs, J.D. (1998). Regional Patterns of Temperature and Precipitation for Newfoundland and Labrador During the Past Century. *The Canadian Geographer/Le Géographe canadien*, 42(4): 354-364.

Bao, H., Kolke, T., Yang, K., Wang, L., Shrestha, M., Lawford, P. (2016). Development of an Enthalpy-Based Frozen Soil Model and its Validation in a Cold Region in China. *Journal of Geophysical Research: Atmospheres*, 121: 5259-5280.

Batenipour, H., Alfaro, M., Kurz, D., Graham, J. (2013). Deformations and Ground Temperatures at a Road Embankment in Northern Canada. *Canadian Geotechnical Journal*, 51: 260-271.

Bell, T., Putt, M., Sheldon, T. (2011). Landscape Hazard Assessment in Nain: Phase I: Inventory of Surficial Sediment Types and Infrastructure Damage, Final Report to Nunatsiavut Government and Nain Inuit Community Government.

Bengtsson, H., Bravo, H.C., Gentleman, R., Hossjer, O., Jaffee, H., Jiang, D., Langfelder, P., Hickey, P., Montgomery, B. (2019). matrixStats: Functions that Apply to Rows and Columns of Matrices (and to Vectors). R package version 0.55.0. https://cran.r-project.org/web/packages/matrixStats/index.html.

Brandt, J.P. (2009). The Extent of the North American Boreal Zone. *Environmental Reviews*, 17: 101-161.

Brehaut, L.D. and Brown, C.D. (2020). Boreal Tree Regeneration After Fire and Fuelwood Harvesting in Coastal Nunatsiavut. *Arctic Science*, DOI: 10.1139/as-2019-0016.

Brown, D.R.N., Jorgenson, M.T., Douglas, T.A., Romanovsky, V.E., Kielland, K., Hiemstra, C., Euskirchen, E.S., Ruess, R.W. (2015). Interactive Effects of Wildfire and Climate on Permafrost Degradation in Alaskan Lowland Forests. *Journal of Geophysical Research: Biogeosciences*, 120: 1619-1637.

Brown, J., Ferrians, O., Heginbottom, J.A., Melnikov, E. (2002). Circum-Arctic Map of Permafrost and Ground-Ice Conditions, Version 2. *NSIDC: National Snow and Ice Data Center*.

Coops, N.C., Hermosilla, T., Wulder, M.A., White, J.C., Bolton, D.K. (2018). A Thirty Year, Fine-Scale, Characterization of Area Burned in Canadian Forests Shows Evidence of Regionally Increasing Trends in the Last Decade. *PLoS ONE*, 13(5): e0197218.

Crown-Indigenous Relations and Northern Affairs Canada. (2007). Inuit Regions (Inuit Nunangat). Retrieved from https://open.canada.ca/data/en/dataset/f242b881-75e3-40bb-a148-63410b4ce2af.

Danby, R.K. and Hik, D.S. (2007). Responses of White Spruce (*Picea glauca*) to Experimental Warming at Subarctic Alpine Treeline. *Global Change Biology*, 13: 437-451.

Darrow, M.M. (2011). Thermal Modeling of Roadway Embankments Over Permafrost. *Cold Regions Science and Technology*, 65: 474-487.

Dyke, A.S. (2004). An Outline of North American Deglaciation with Emphasis on Central and Northern Canada. *Developments in Quaternary Sciences*, 2: 373:424.

Environment and Climate Change Canada. (2020). Canadian Climate Normal, 1981-2010. Retrieved from www.climate.weather.gc.ca.

Fisher, J.P., Estop-Aragones, C., Thierry, A., Charman, D.J., Wolfe, S.A., Hartley, I.P., Murton, J.B., Williams, M., Phoenix, G.K. (2016). The Influence of Vegetation and Soil Characteristics on Active-Layer Thickness of Permafrost Soils in Boreal Forest. *Global Change Biology*, 22: 3127-3140.

Foster, D.R. (1983). The History and Pattern of Fire in the Boreal Forest of Southeastern Labrador. *Canadian Journal of Botany*, 61(9): 2459-2471.

GEO-SLOPE International, Ltd. (2014). Thermal Modeling with TEMP/W, an Engineering Methodology.

Gibson, C.M., Chasmer, L.E., Thompson, D.K., Quinton, W.L., Flannigan, M.D., Olefeldt, D. (2018). Wildfire as a Major Driver of Recent Permafrost Thaw in Boreal Peatlands. *Nature Communications*, 9:3041.

Government of Newfoundland and Labrador. (2001a). News Release. Retrieved January 7, 2020, from https://www.releases.gov.nl.ca/releases/2001/forest/0514n05.htm

Government of Newfoundland and Labrador. (2001b). News Release. Retrieved January 7, 2020, from https://www.releases.gov.nl.ca/releases/2001/forest/1015n03.htm

Hare, F.K. (1950). Climate and Zonal Divisions of the Boreal Forest Formation in Eastern Canada. *The Geographical Review*, 40(4): 615-635.

Heginbottom, J.A., Dubreuil, M.A., Harker, P.A. (1995). Canada Permafrost, in National Atlas of Canada, 5th edition, Natural Resources Canada.

Holloway, J.E., Lewkowicz, A.G., Douglas, T.A., Li, X., Turetsky, M.R., Baltzer, J.L., Jin, H. (2020). Impact of Wildfire on Permafrost Landscapes: A Review of Recent Advances and Future Prospects. *Permafrost and Periglacial Processes*, DOI: 10.1002/ppp.2048.

Hope, E.S., McKenney, D.W., Pedlar, J.H., Stocks, B.J., Gauthier, S. (2016). Wildfire Suppression Costs for Canada Under a Changing Climate. *PLoS ONE*, 11(8): e0157425.

Instanes, A. (2016). Incorporating Climate Warming Scenarios in Coastal Permafrost Engineering Design – Case Studies from Svalbard and Northwest Russia. *Cold Regions Science and Technology*, 131: 76-87.

Isaksen, K., Hauck, C., Gudevang, E., Odegard, R.S., Sollid, J.L. (2002). Mountain Permafrost Distribution in Dovrefjell and Jotunheimen, Southern Norway, Based on BTS and DC Resistivity Tomography Data. *Norwegian Journal of Geography*, 56: 122-136.

Jafarov, E.E., Romanovsky, V.E., Genet, E., McGuire, A.D., Marchenko, S.S. (2013). The Effects of Fire on the Thermal Stability of Permafrost in Lowland and Upland Black Spruce Forests of Interior Alaska in a Changing Climate. *Environmental Research Letters*, 8: 035030.

Johnston, G.H. (Ed). (1981). Permafrost: Engineering Design and Construction. John Wiley and Sons.

Jorgenson, M.T., Romanovsky, V., Harden, J., Shur, Y., O'Donnell, J., Schuur, E.A.G., Kanevskiy, M., Marchenko, S. (2010). Resilience and Vulnerability of Permafrost to Climate Change. *Canadian Journal of Forest Research*, 40: 1219-1236.

Karunaratne, K.C. and Burn, C.R. (2003). Freezing N-Factors in Discontinuous Permafrost Terrain, Takhini River, Yukon Territory, Canada. In Proceedings of the Eighth International Conference on Permafrost, in Zurich, Switzerland.

Karunaratne, K.C. and Burn, C.R. (2004). Relations Between Air and Surface Temperature in Discontinuous Permafrost Terrain Near Mayo, Yukon Territory. *Canadian Journal of Earth Sciences*, 41: 1437-1451.

Kasischke, E.S. and Johnstone, J.F. (2005). Variation in Postfire Organic Layer Thickness in a Black Spruce Forest Complex in Interior Alaska and its Effects on Soil Temperature and Moisture. *Canadian Journal of Forest Research*, 35: 2164-2177.

Lewkowicz, A.G. (2008). Evaluation of Miniature Temperature-Loggers to Monitor Snowpack Evolution at Mountain Permafrost Sites, Northwestern Canada. *Permafrost and Periglacial Processes*, 19: 323-331.

Majorowicz, J.A. and Minea, V. (2012). Geothermal Energy Potential in the St. Lawrence River Area Quebec. *Geothermics*, 43: 25-36.

Mareschal, J.C., Poirier, A., Rolandone, F., Bienfait, G., Gariepy, C., Lapointe, R., Jaupart, C. (2000). Low Mantle Heat Flow at the Edge of the North American Continent, Voisey Bay, Labrador. *Geophysical Research Letters*, 27(6): 823-826.

McClymont, A.F., Hayashi, M., Bentley, L.R., Christensen, B.S. (2013). Geophysical Imaging and Thermal Modeling of Subsurface Morphology and Thaw Evolution of Discontinuous Permafrost. *Journal of Geophysical Research: Each Surface*, 118: 1826-1837.

Meredith, M., Sommerkorn, M., Cassotta, S., Derksen, C., Ekaykin, A., Hollowed, A., Kofinas, G., Mackintosh, A., Melbourne-Thomas, J., Muelbert, M.M.C., Ottersen, G., Pritchard, H., Schuur, E.A.G. (2019). Polar Regions. In IPCC Special Report on the Ocean and Cryosphere in a Changing Climate.

Moss, R.H., Edmonds, J.A., Hibbard, K.A., Manning, M.R., Rose, S.K., van Vuuren, D.P., Carter, T.R., Emori, S., Kainuma, M., Kram, T., Meehl, G.A., Mitchell, J.F.B., Nakicenovic, N., Riahi, K., Smith, S.J., Stouffer, R.J., Thomson, A.M., Weyant, J.P., Wilbanks, T.J. (2010). The Next Generation of Scenarios for Climate Change Research and Assessment. *Nature*, 463: 747–756.

Mudryk, L.R., Derksen, C., Kushner, P.J., Brown, R. (2015). Characterization of Northern Hemisphere Snow Water Equivalent Datasets, 1981-2010. *American Meteorological Society*, 28: 8037-8051.

Natural Resources Canada (2017). Atlas of Canada, 3rd Edition (1957). Bedrock Geology, Series 016.

Nossov, D.R., Jorgenson, M.T., Kielland, K., Kanevskiy, M.Z. (2013). Edaphic and Microclimatic Controls Over Permafrost Response to Fire in Interior Alaska. *Environmental Research Letters*, 8: 035013.

O'Donnell, J.A., Harden, J.W., McGuire, A.D., Romanovsky, V.E. (2011). Exploring the Sensitivity of Soil Carbon Dynamics to Climate Change, Fire Disturbance and Permafrost Thaw in a Black Spruce Ecosystem. *Biogeosciences*, 8: 1367-1382.

Perreault, P. and Shur, Y. (2016). Seasonal Thermal Insulation to Mitigate Climate Change Impacts on Foundations in Permafrost Regions. *Cold Regions Science and Technology*, 132: 7-18.

Riseborough, D.W. and Smith, M.W. (1998). Exploring the Limits of Permafrost. In Proceedings for the Seventh International Conference on Permafrost, in Yellowknife, Canada.

Roberts, B.A., Simon, N.P.P., Deering, K.W. (2006). The Forests and Woodlands of Labrador, Canada: Ecology, Distribution and Future Management. *Ecological Research*, 21: 868-880.

Rohde, R., Muller, R.A., Jacobsen, R., Muller, E., Perlmutter, S., Rosenfeld, A., Wurtele, J., Groom, D., Wickham, C. (2013). A New Estimate of the Average Earth Surface Land Temperature Spanning 1753 to 2011. *Geoinformation Geostatistics: An Overview*, 1:1.

Serreze, M.C. and Barry, R.G. (2011). Processes and Impacts of Arctic Amplification: A Research Synthesis. *Global and Planetary Change,* 77: 85-96.

Shur, Y.L. and Jorgenson, M.T. (2007). Patterns of Permafrost Formation and Degradation in Relation to Climate and Ecosystems. *Permafrost and Periglacial Processes*, 18: 7-19.

Smith, S. and Riseborough, D.W. (2010). Modelling the Thermal Response of Permafrost Terrain to Right-Of-Way Disturbance and Climate Warming. *Cold Regions Science and Technology*, 60: 92-103.

Treat, C.C., Wisser, D., Marchenko, S., Frolking, S. (2013). Modelling the Effects of Climate Change and Disturbance on Permafrost Stability in Northern Organic Soils. *Mires and Peat*, 12: 1-17.

van Vuuren, D.P., Edmonds, J., Kainuma, M., Riahi, K., Thomson, A., Hibbard, K., Hurtt, G.C., Kram, T., Krey, V., Lamarque, J.-F., Masui, T., Meinshausen, M., Nakicenovic, N., Smith, S.J., Rose, S.K. (2011). The Representative Concentration Pathways: An Overview. *Climatic Change*, 109: 5-31.

Way, R.G. and Lewkowicz, A.G. (2016). Modelling the Spatial Distribution of Permafrost in Labrador-Ungava Using the Temperature at the Top of Permafrost. *Canadian Journal of Earth Sciences*, 53: 1010-1028.

Way, R.G. and Viau, A.E. (2015). Natural and Forced Air Temperature Variability in the Labrador Region of Canada During the Past Century. *Theoretical and Applied Climatology*, 121(5): 413-424.

Williams, T.G. and Flanagan, L.B. (1998). Measuring and Modelling Environmental Influences on Photosynthetic Gas Exchange in Sphagnum and Pleurozium. *Plant, Cell and Environment*, 21: 555-564.

Williams, P.J. and Smith, M.W. (1989). The Frozen Earth, Fundamentals of Geocryology. Cambridge University Press.

Yi, S., McGuire, A.D., Kasischke, E., Harden, J., Manies, K., Mack, M., Turetsky, M. (2010). A Dynamic Organic Soil Biogeochemical Model for Simulating the Effects of Wildfire on Soil Environmental Conditions and Carbon Dynamics of Black Spruce Forests. *Journal of Geophysical Research*, 115: G04015.

Yoshikawa, K., Bolton, W.R., Romanovsky, V.E., Fukuda, M., Hinzman, L.D. (2003). Impacts of Wildfire on the Permafrost in the Boreal Forests of Interior Alaska. *Journal of Geophysical Research*, 108(D1): 8148.

Zhang, Y., Wolfe, S.A., Morse, P.D., Olthof, I., Fraser, R.H. (2015). Spatiotemporal Impacts of Wildfire and Climate Warming on Permafrost Across a Subarctic Region, Canada. *Journal of Geophysical Research: Earth Surface*, 120: 2338-2356.

CHAPTER 6 : CONCLUSIONS

6.1 Summary of Findings

This dissertation incorporates a combination of field investigations and modelling efforts to improve our understanding of the post-fire response of the coastal boreal forests of the eastern Canadian subarctic. The project addresses the complex post-fire interactions between snow, vegetation, and frozen ground in the coastal Labrador region, within the context of a warming climate. Field methods were drawn from various disciplines, including ecology, permafrost science, and snow science, and observations were collected during both summer and winter to achieve a comprehensive overview of post-fire ground and surface conditions at three sites in Nunatsiavut.

Permafrost was inferred to be present in the undisturbed forests of the two sites near Nain, owing to the fine-grained, frost-susceptible substrate and the ecosystem protection offered by the forest canopy of the surrounding boreal environment. The presence of permafrost in forested lowland locations throughout Labrador is thought to be limited, so these patches of frozen ground represent some of the first contemporary observations of permafrost in these kinds of environments. The post-fire trajectory of this frozen ground was examined using one-dimensional thermal modelling in TEMP/W. The simulations, extending to 2100, demonstrate the resiliency of the climate-driven, ecosystem-protected permafrost that was found beneath the coastal boreal forests near Nain. Fire disturbance triggers the development of a supra-permafrost talik, which has lasting impacts on the ground thermal regime and accelerates the inevitable loss of frozen ground to the increasing air and ground temperatures that are associated with a warming climate. However, the low severity of these fire disturbances, coupled with post-fire ecological succession, permits ecosystem-driven permafrost to form and to eventually mature into ecosystem-protected permafrost. This ecosystem-protected permafrost is much more sensitive to change and is not likely to recover following further disturbance, such as additional forest fires or the cumulative effects of climate warming. At the southern site near Postville, no permafrost was detected, reflecting the warmer climate and the sparse distribution of permafrost in this area.

Post-fire vegetation was dominated by shrubs, but their thermal impact was limited by the deep snow cover that accumulates in both burned and unburned regions of our sites and by the presence of other erect vegetation, including standing dead and regenerating trees. The impacts of shrubs in snow-trapping and advancing snowmelt on the tundra are diminished in this post-fire boreal environment. While snow depths were indeed higher in the burned areas as expected, this is likely not due to snow-trapping around shrubs. Instead, differences in snow distribution are believed to be associated with the interception of falling snow by forest canopy, resulting in shallower snow cover in the unburned forest and deeper snow cover in the burned area.

The results from coastal Labrador broadly agree with those reported for the western North American boreal forest, but the wetter climate, longer fire intervals, and deeper snowpacks are associated with an accelerated loss of frozen ground following fire. Fire is modelled to accelerate the loss of permafrost in coastal Labrador by approximately three times the rate reported for the Northwest Territories (Zhang et al., 2015). This may be partly due to the more sensitive initial ground temperatures and lower ground ice contents at the study sites, but poor post-fire ecological protection may also play a role. The long fire intervals for the coastal Labrador region result in slow, continuous recruitment of trees over many decades (Brehaut and Brown, 2020), unlike the pulse recruitment that occurs within the first decade following fire in the western North American boreal forest (Johnstone et al., 2004). The slow regeneration extends the period when the canopy does not intercept snow in winter or provide shade in summer. With a warming climate, permafrost is especially vulnerable in this post-disturbance stage, particularly if the ecological protection that is typically offered by a regenerating forest canopy is delayed. The multi-decadal post-fire forest regeneration process that is associated with the longer fire intervals of the coastal Labrador region therefore accelerates the post-fire loss of frozen ground in the region beyond the rates reported in the West.

6.2 Research Limitations and Future Research Directions

The high costs and logistical obstacles associated with fieldwork in remote regions of coastal Labrador raised challenges in terms of equipment availability and representational sampling. Our small sampling scheme, running along two or three parallel transects per site, does not necessarily address the variability that might exist across the forest fire extents. For example, the BR fire disturbed an area of approximately 150 km^2, so it is impossible to claim that our results can be extended across this entire region. Our sampling locations were positioned relatively close to shore, near our boat-access point, so our results do not represent conditions at higher elevations within the burned regions. Furthermore, our transects were established to facilitate geophysical investigations using ERT. However, the linear nature of the ERT method raised issues of spatial dependency in associated variables, like shrub height or density and snow depth. Operational and logistical constraints complicated the ERT investigations, and only two surveys could be performed per site. Additional surveys, covering deeper areas in the respective burned and unburned regions, would greatly improve our spatial understanding of post-fire site conditions.

The thermal model was validated against ground surface temperature data at one site, measured over only one year. While the modelled ground surface temperatures agreed with the measured values, the modelling would have been greatly improved by temperature validations at depth in a borehole. However, this was not possible, due to the coarse surficial materials and permitting restrictions for the overall research project. Two-dimensional modelling, incorporating lateral heat and water flow across the transect, would also greatly improve our understanding of local permafrost degradation across burned to unburned transition zones. The computational burden of the TEMP/W program complicated the thermal modelling process, and additional sensitivity analyses for other inputs, including the n-factors, were not performed for the purposes of this dissertation. These sensitivity analyses should be a focus of future studies, to investigate the range of n-factors and associated conditions, like snow depth, that might continue to permit permafrost persistence and re-aggradation following fire.

Despite these limitations, this research represents a significant first step towards understanding the conditions and response of frozen ground following forest fire disturbance in the coastal boreal forests of the eastern Canadian subarctic.

6.3 References

Brehaut, L.D. and Brown, C.D. (2020). Boreal Tree Regeneration After Fire and Fuelwood Harvesting in Coastal Nunatsiavut. *Arctic Science*, DOI: 10.1139/as-2019-0016.

Johnstone, J.F., Chapin III, F.S., Foote, J., Kemmett, S., Price, K., Viereck, L. (2004). Decadal Observations of Tree Regeneration Following Fire in Boreal Forests. *Canadian Journal of Forest Research*, 34: 267-273.

Zhang, Y., Wolfe, S.A., Morse, P.D., Olthof, I., Fraser, R.H. (2015). Spatiotemporal Impacts of Wildfire and Climate Warming on Permafrost Across a Subarctic Region, Canada. *Journal of Geophysical Research: Earth Surface*, 120: 2338-2356.

CHAPTER 7 : APPENDICES

Appendix A: Supplemental Tables for Chapter 4.

Table 7-1. Summary Statistics for Environmental Variables Measured Along Burned and Unburned Portions of Two 80 m-long Transects at TB.

Burned Unburned	Variable	Mean	Standard Deviation	Maximum	Minimum	Count (n)
BURNED	Snow Depth (cm)	120	20	198	93	82
	Near-Surface Resistivity (Ωm)	2183	1279	5796	519	70
	Organic Layer Thickness (cm)	16	9	38	5	81
	Soil Temperature (°C)	14.7	2.57	20.0	10.2	42
	Soil Moisture (vol cm^3/cm^3)	0.24	0.11	0.55	0.05	42
	Total Canopy Cover (%)	50	21	82	12	82
	Understory Canopy Cover (%)	21	18	65	-23	82
	Maximum Shrub Height (cm)	90	49	215	25	75
	Shrub Density ($stems/m^2$)	136	94	328	0	82
UNBURNED	Snow Depth (cm)	114	25	189	60	80
	Near-Surface Resistivity (Ωm)	2758	1837	8809	767	76
	Organic Layer Thickness (cm)	23	10	50	2	80
	Soil Temperature (°C)	12.1	3.3	17.8	6.1	38
	Soil Moisture (vol cm^3/cm^3)	0.22	0.18	0.79	0.07	38
	Total Canopy Cover (%)	68	14	82	18	80
	Understory Canopy Cover (%)	11	12	60	-11	80
	Maximum Shrub Height (cm)	95	56	215	25	58
	Shrub Density ($stems/m^2$)	52	50	216	0	78

Table 7-2. Summary Statistics for Environmental Variables Measured Along Burned and Unburned Portions of Two 80 m-long Transects at WB.

Burned Unburned	Variable	Mean	Standard Deviation	Maximum	Minimum	Count (n)
BURNED	Snow Depth (cm)	110	26	190	40	82
	Near-Surface Resistivity (Ωm)	3349	1892	11547	1473	80
	Organic Layer Thickness (cm)	12	6	38	2	82
	Soil Temperature (°C)	8.4	2.0	10.8	5.1	42
	Soil Moisture (vol cm^3/cm^3)	0.23	0.09	0.41	0.10	42
	Total Canopy Cover (%)	44	16	81	15	82
	Understory Canopy Cover (%)	22	16	65	-5	82
	Maximum Shrub Height (cm)	56	17	110	25	69
	Shrub Density (stems/m^2)	61	45	216	0	82
UNBURNED	Snow Depth (cm)	143	32	210	61	80
	Near-Surface Resistivity (Ωm)	1613	556	2871	705	76
	Organic Layer Thickness (cm)	18	9	50	0	80
	Soil Temperature (°C)	7.6	0.9	10.4	5.3	38
	Soil Moisture (vol cm^3/cm^3)	0.19	0.06	0.37	0.09	38
	Total Canopy Cover (%)	60	15	80	18	80
	Understory Canopy Cover (%)	10	14	58	-13	80
	Maximum Shrub Height (cm)	54	27	146	25	63
	Shrub Density (stems/m^2)	43	36	140	0	78

Table 7-3. Summary Statistics for Environmental Variables Measured Along Burned and Unburned Portions of Three Transects (40 m, 40 m, and 50 m-long) at BR.

Burned Unburned	Variable	Mean	Standard Deviation	Maximum	Minimum	Count (n)
BURNED	Snow Depth (cm)	173	23	224	122	65
	Near-Surface Resistivity (Ωm)	385	898	5278	65	36
	Organic Layer Thickness (cm)	17	8	39	8	65
	Soil Temperature (°C)	16.4	1.5	20.4	14.1	38
	Soil Moisture (vol cm^3/cm^3)	0.30	0.12	0.72	0.12	38
	Total Canopy Cover (%)	57	20	83	21	65
	Understory Canopy Cover (%)	13	14	56	-28	65
	Maximum Shrub Height (cm)	107	94	450	42	62
	Shrub Density (stems/m^2)	88	76	400	0	63
UNBURNED	Snow Depth (cm)	155	17	201	110	68
	Near-Surface Resistivity (Ωm)	412	70	3218	60	40
	Organic Layer Thickness (cm)	27	10	50	0	68
	Soil Temperature (°C)	16.1	1.6	19.6	12.1	42
	Soil Moisture (vol cm^3/cm^3)	0.19	0.10	0.50	0.07	42
	Total Canopy Cover (%)	68	12	87	31	68
	Understory Canopy Cover (%)	10	10	47	-16	68
	Maximum Shrub Height (cm)	77	23	400	26	57
	Shrub Density (stems/m^2)	41	45	152	0	68

Appendix B: Example of R Code for Calculating Annual Maximum, Minimum, and Mean Ground Temperatures from TEMP/W Outputs.

```
#install.packages("matrixStats")
library(matrixStats)

#set working drive in folder
setwd("C:\\Users\\yifen\\Desktop\\WB_CSV")
#getwd()
#dir()

BURN4.5_1965<-read.csv("WB_BURN_4.5_1965_2004.csv", skip=1)
#dim(BURN4.5_1965)
#str(BURN4.5_1965)
BURN4.5_1965_matrix<-data.matrix(BURN4.5_1965)

YEAR<-1965

#WEBB BAY
start_year<-
c(1965,2009,2014,2018,2019,2024,2029,2034,2039,1965,2049,2054,2059,2064,2069,2074,2079,2084,2089,2
094,2099)

#TIKKOATOKAK BAY
#start_year<-
c(1965,2006,2011,2016,2018,2021,2026,2031,2036,2041,2046,2051,2056,2061,2066,2071,2076,2081,2086,2
091,2096)

if (YEAR %in% start_year){
  start<-3
} else {
  start<-(end+1)
}

if((YEAR %% 4) == 0) {
  if((YEAR %% 100) == 0) {
    if((YEAR %% 400) == 0) {
      ndays<-365
    } else {
      ndays<-364
    }
  } else {
    ndays<-365
  }
} else {
  ndays<-364
}

start
ndays
end<-(start+ndays)
end

for (umc_temp in c(-0.001, -0.002, -0.003, -0.004, -0.005, -0.006, -0.007, -0.008, -0.009, -
0.01)){
  #create depth column
  depth=BURN4.5_1965[,1]
  #create mean column, computing mean of every depth
  means=rowMeans(BURN4.5_1965[,start:end])
  #create max column, computing max of every depth, requires matrixStats package, data must be
stored in matrix
  maxs=rowMaxs(BURN4.5_1965_matrix[,start:end])
  #create min column, computing min of every depth, requires matrixStats package, data must be
stored in matrix
  mins=rowMins(BURN4.5_1965_matrix[,start:end])
  #create range column, computing difference between maximum and minimum values at every depth
  DIFF=maxs-mins

  #create new dataframe with max, min, mean, and range values at every depth
  trumpet4.5_1965<-data.frame(DEPTH=depth, MAX=maxs, MEAN=means, MIN=mins, RANGE=DIFF)
  #check dataframe contents
  #head(trumpet4.5_1965)
  #tail(trumpet4.5_1965)
```

```
  #create zero annual amplitude column, TRUE = below dzaa, FALSE = above dzaa
  DZAA<-ifelse(trumpet4.5_1965$RANGE<0.1, "TRUE", "FALSE")
  #create base of permafrost column, TRUE = below base of permafrost, FALSE = above base of
permafrost
  PMF_BASE<-ifelse(trumpet4.5_1965$MAX>(umc_temp), "TRUE", "FALSE")
  #create top of permafrost column, TRUE = below top of permafrost, FALSE = above top of
permafrost
  PMF_TOP<-ifelse(trumpet4.5_1965$MAX<(umc_temp), "TRUE", "FALSE")
  #create active layer column, TRUE = within AL, FALSE = beneath AL
  ALmin<-ifelse(trumpet4.5_1965$MIN<(umc_temp), "TRUE", "FALSE")

  #create new dataframe with max, min, mean, range, dzaa, base_pmf, top, and base_al values at
every depth
  trumpet4.5_1965<-data.frame(DEPTH=depth, MAX=maxs, MEAN=means, MIN=mins, RANGE=DIFF, DZAA=DZAA,
BASE_PMF=PMF_BASE, TOP_PMF=PMF_TOP, BASE_AL=ALmin)
  #check dataframe contents
  #head(trumpet4.5_1965)
  #tail(trumpet4.5_1965)

  #DEPTH AND TEMPERATURE OF ZERO ANNUAL AMPLITUDE
  #determine row position of DZAA
  (which.min(trumpet4.5_1965$DZAA))-1
  #return row of DZAA
  trumpet4.5_1965[((which.min(trumpet4.5_1965$DZAA))-1),]
  #return temperature at depth of zero annual amplitude
  TZAA<-trumpet4.5_1965[((which.min(trumpet4.5_1965$DZAA))-1),3]
  TZAA
  #return DZAA
  D_ZAA<-trumpet4.5_1965[((which.min(trumpet4.5_1965$DZAA))-1),1]
  D_ZAA

  #DEPTH OF BASE OF PERMAFROST
  #determine row position of base of permafrost
  which.min(trumpet4.5_1965$BASE_PMF)-1
  #return row of base of permafrost
  trumpet4.5_1965[((which.min(trumpet4.5_1965$BASE_PMF))-1),]
  #return temperature of base of permafrost
  trumpet4.5_1965[((which.min(trumpet4.5_1965$BASE_PMF))-1),3]
  #return depth of base of permafrost
  PMF_B<-trumpet4.5_1965[(which.min(trumpet4.5_1965$BASE_PMF)),1]
  PMF_B

  #invert the rows of the trumpet curve data frame
  trumpet4.5_1965_invert<-trumpet4.5_1965[order(nrow(trumpet4.5_1965):1),]
  #print(trumpet4.5_1965_invert)

  #DEPTH AND TEMPERATURE OF TOP OF PERMAFROST
  #determine row position of top of permafrost
  which.max(trumpet4.5_1965_invert$TOP_PMF)
  #return row of top of permafrost
  trumpet4.5_1965_invert[((which.max(trumpet4.5_1965_invert$TOP_PMF))),]
  #return maximum temperature at top of permafrost
  trumpet4.5_1965_invert[((which.max(trumpet4.5_1965_invert$TOP_PMF))),4]
  #return depth of top of permafrost
  PMF_T<-trumpet4.5_1965_invert[((which.max(trumpet4.5_1965_invert$TOP_PMF))),1]
  PMF_T
  TTOP<-trumpet4.5_1965_invert[((which.max(trumpet4.5_1965_invert$TOP_PMF))),3]
  TTOP

  #DEPTH OF BASE OF ACTIVE LAYER (WHEN TALIK IS PRESENT)
  #determine row position of base of active layer
  which.min(trumpet4.5_1965_invert$BASE_AL)-1
  #return row of base of active layer
  trumpet4.5_1965_invert[((which.min(trumpet4.5_1965_invert$BASE_AL)-1)),]
  #return temperature of base of active layer
  trumpet4.5_1965_invert[((which.min(trumpet4.5_1965_invert$BASE_AL)-1)),4]
  #return depth of base of active layer
  AL_B_TALIK<-trumpet4.5_1965_invert[((which.min(trumpet4.5_1965_invert$BASE_AL)-1)),1]
  AL_B_TALIK

  #DEPTH OF BASE OF ACTIVE LAYER (WHEN TALIK IS ABSENT)
  #determine row position of base of active layer
  which.min(trumpet4.5_1965_invert$BASE_PMF)
  #return row of base of active layer
  trumpet4.5_1965_invert[((which.min(trumpet4.5_1965_invert$BASE_PMF))),]
  #return temperature of base of active layer
```

```
  trumpet4.5_1965_invert[((which.min(trumpet4.5_1965_invert$BASE_PMF))),4]
  #return depth of base of active layer
  AL_B<-trumpet4.5_1965_invert[((which.min(trumpet4.5_1965_invert$BASE_PMF))),1]
  AL_B

  #DEPTH AND TEMPERATURE OF GROUND SURFACE
  Y<-trumpet4.5_1965[(nrow(trumpet4.5_1965)),1]
  Y
  TGS<-trumpet4.5_1965[(nrow(trumpet4.5_1965)),3]
  TGS

  #TALIK PRESENCE OR ABSENCE
  #determine presence or absence of suprapermafrost talik
  talik<-ifelse(abs(max(AL_B_TALIK,AL_B)-PMF_T)==0, "ABSENT", "PRESENT")
  talik
  #return talik thickness
  talik_thickness<-abs(PMF_T-max(AL_B,AL_B_TALIK))
  talik_thickness

  #plot trumpet curve
  xrange<-c(-12,22)
  yrange<-c(-20,1)
  png(filename = "trumpet4.5_1965.png", units = "px")
  plot(xlim=xrange, ylim=yrange, trumpet4.5_1965$DEPTH~trumpet4.5_1965$MAX, type="l", col="red",
ylab="Depth (m)", xlab="Temperature (C)", main="1965")
  points(trumpet4.5_1965$DEPTH~trumpet4.5_1965$MIN,type="l",col="blue")
  points(trumpet4.5_1965$DEPTH~trumpet4.5_1965$MEAN,type="l")
  abline(a=NULL,b=NULL,h=NULL,v=0,col="BLACK")
  dev.off()

  #create new data frame
  summary_4.5_1965<-data.frame(YEAR=YEAR, SURFACE=Y, TGS=TGS, BASE_AL=max(AL_B_TALIK,AL_B),
AL_THICKNESS=abs(max(AL_B_TALIK,AL_B)-Y), BASE_PMF=PMF_B, TOP_PMF=PMF_T, TTOP=TTOP,
PMF_THICKNESS=abs(PMF_B-PMF_T), TALIK=talik, TALIK_THICKNESS=talik_thickness, DZAA=D_ZAA,
TZAA=TZAA, THERM_OFF=abs(TTOP-TGS), UMC=umc_temp)
  summary_4.5_1965
  #write.csv(summary_4.5_1965,"summary_4.5_BURN.csv")
  write.table(summary_4.5_1965, file = "summary_4.5_BURN.csv", sep = ",", append=TRUE,
quote=FALSE, col.names=FALSE)

}

#append columns to csv file
#write.csv((cbind(trumpet4.5_1965$DEPTH,trumpet4.5_1965$MAX)),"trumpet_MAX_4.5_BURN.csv")
#write.csv((cbind(trumpet4.5_1965$DEPTH,trumpet4.5_1965$MIN)),"trumpet_MIN_4.5_BURN.csv")
#write.csv((cbind(trumpet4.5_1965$DEPTH,trumpet4.5_1965$MEAN)),"trumpet_MEAN_4.5_BURN.csv")
#write.csv((cbind(trumpet4.5_1965$DEPTH,trumpet4.5_1965$RANGE)),"trumpet_RANGE_4.5_BURN.csv")
trumpet_max<-read.csv("trumpet_MAX_4.5_BURN.csv")
trumpet_min<-read.csv("trumpet_MIN_4.5_BURN.csv")
trumpet_mean<-read.csv("trumpet_MEAN_4.5_BURN.csv")
trumpet_range<-read.csv("trumpet_RANGE_4.5_BURN.csv")
vector_max_1965<-trumpet4.5_1965$MAX
length(vector_max_1965)<-456
col_MAX<-cbind(trumpet_max,vector_max_1965)
vector_min_1965<-trumpet4.5_1965$MIN
length(vector_min_1965)<-456
col_MIN<-cbind(trumpet_min,vector_min_1965)
vector_mean_1965<-trumpet4.5_1965$MEAN
length(vector_mean_1965)<-456
col_MEAN<-cbind(trumpet_mean,vector_mean_1965)
vector_range_1965<-trumpet4.5_1965$RANGE
length(vector_range_1965)<-456
col_RANGE<-cbind(trumpet_range,vector_range_1965)
write.csv(col_MAX,"trumpet_MAX_4.5_BURN.csv")
write.csv(col_MIN,"trumpet_MIN_4.5_BURN.csv")
write.csv(col_MEAN,"trumpet_MEAN_4.5_BURN.csv")
write.csv(col_RANGE,"trumpet_RANGE_4.5_BURN.csv")
```

Appendix C: Supplemental Modelling Simulation Results for Chapter 5.

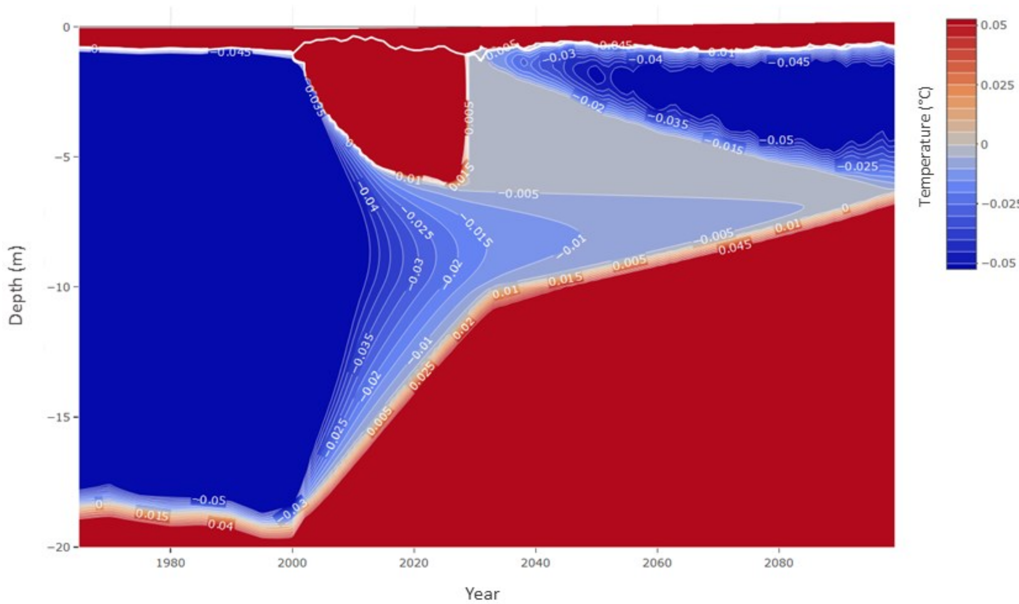

Figure 7-1. Modelled Ground Temperatures (1965-2099) Following Low Burn Severity Fire in 2001 at the TB Site Under RCP4.5. Organic material accumulated at 2.9 mm/year from 2001 to 2099. The base of the active layer, approximated by a temperature threshold of -0.025°C or an unfrozen moisture content of 0.11, is shown as a white line.

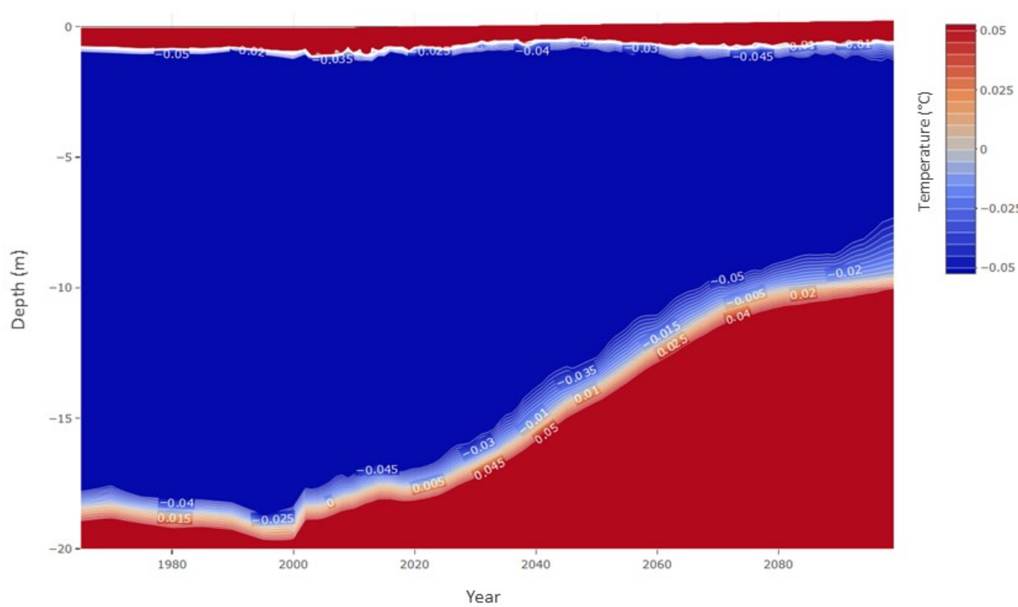

Figure 7-2. Modelled Ground Temperatures (1965-2099) at Unburned TB Site Under RCP4.5. Organic material accumulated at 2.9 mm/year from 2001 to 2099. The base of the active layer, approximated by a temperature threshold of -0.025°C or an unfrozen moisture content of 0.11, is shown as a white line.

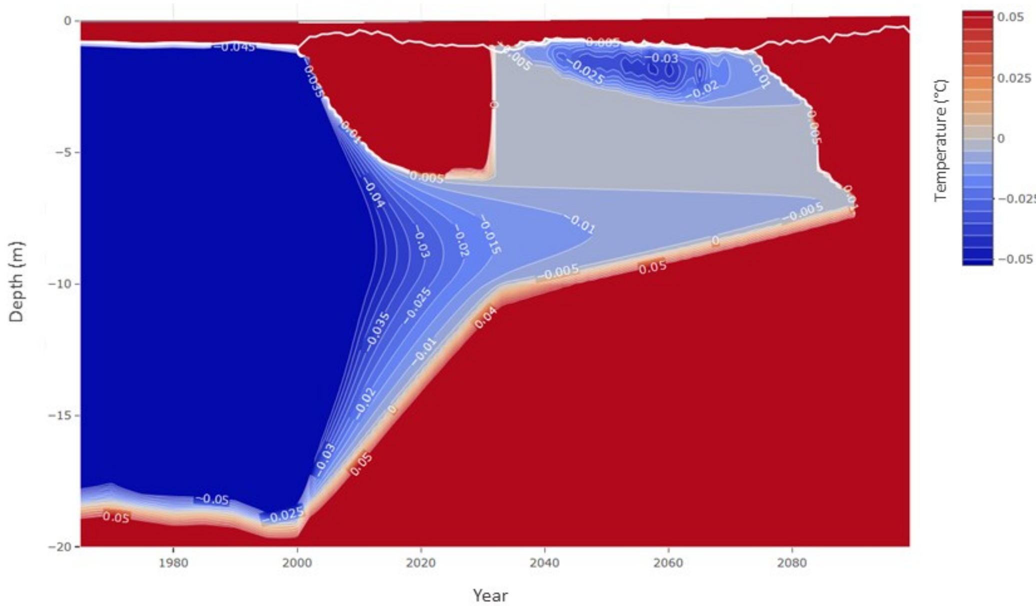

Figure 7-3. Modelled Ground Temperatures (1965-2099) Following Low Burn Severity Fire in 2001 at the TB Site Under RCP8.5. Organic material accumulated at 2.9 mm/year from 2001 to 2099. The base of the active layer, approximated by a temperature threshold of -0.025°C or an unfrozen moisture content of 0.11, is shown as a white line.

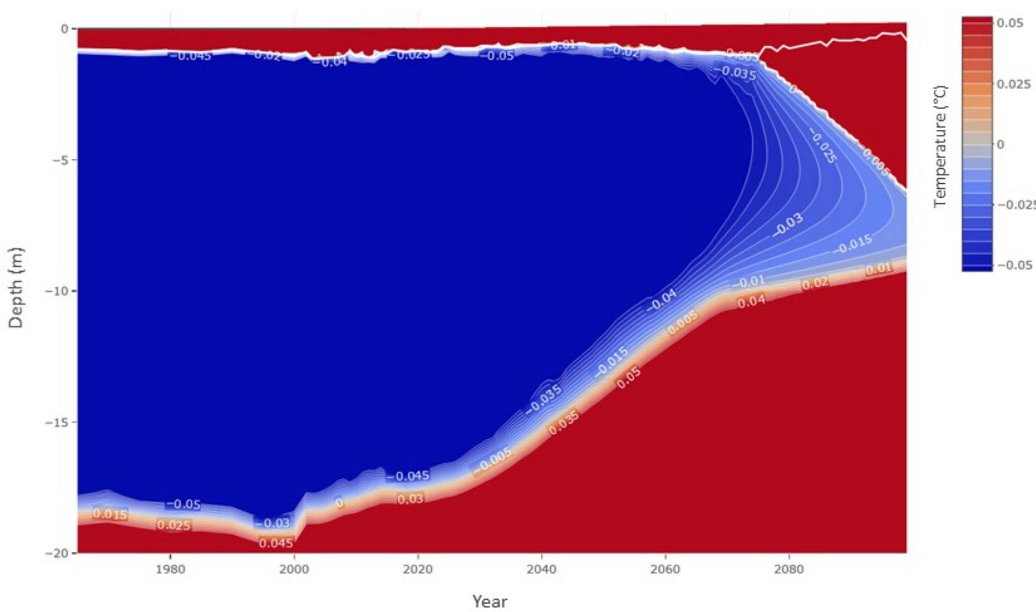

Figure 7-4. Modelled Ground Temperatures (1965-2099) at Unburned TB Site Under RCP8.5. Organic material accumulated at 2.9 mm/year from 2001 to 2099. The base of the active layer, approximated by a temperature threshold of -0.025°C or an unfrozen moisture content of 0.11, is shown as a white line.

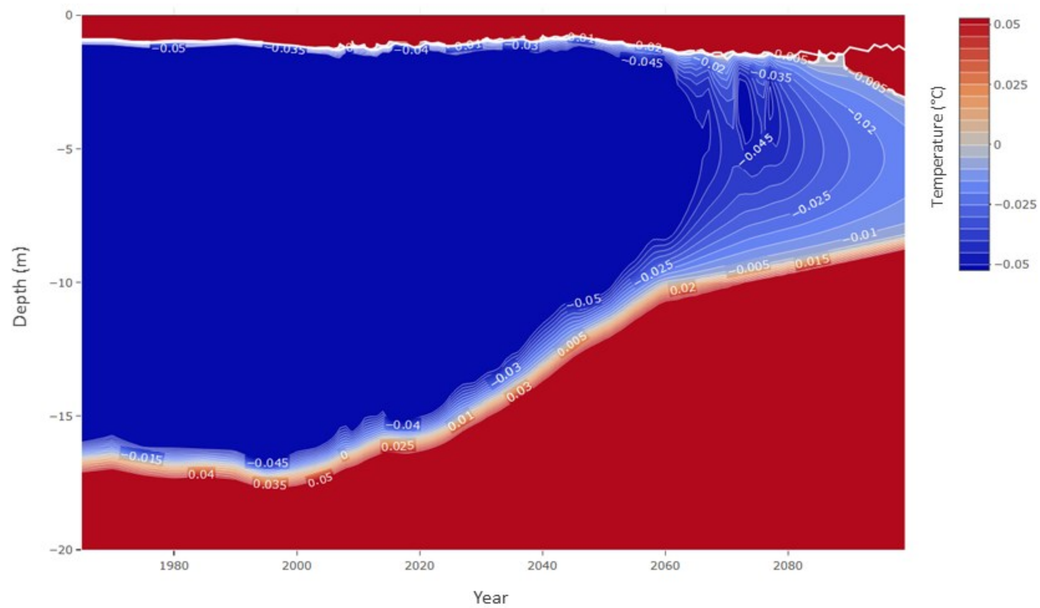

Figure 7-5. Modelled Ground Temperatures (1965-2099) at Unburned WB Site Under RCP4.5. Organic mat accumulation did not occur. The base of the active layer, approximated by a temperature threshold of -0.025°C or an unfrozen moisture content of 0.11, is shown as a white line.

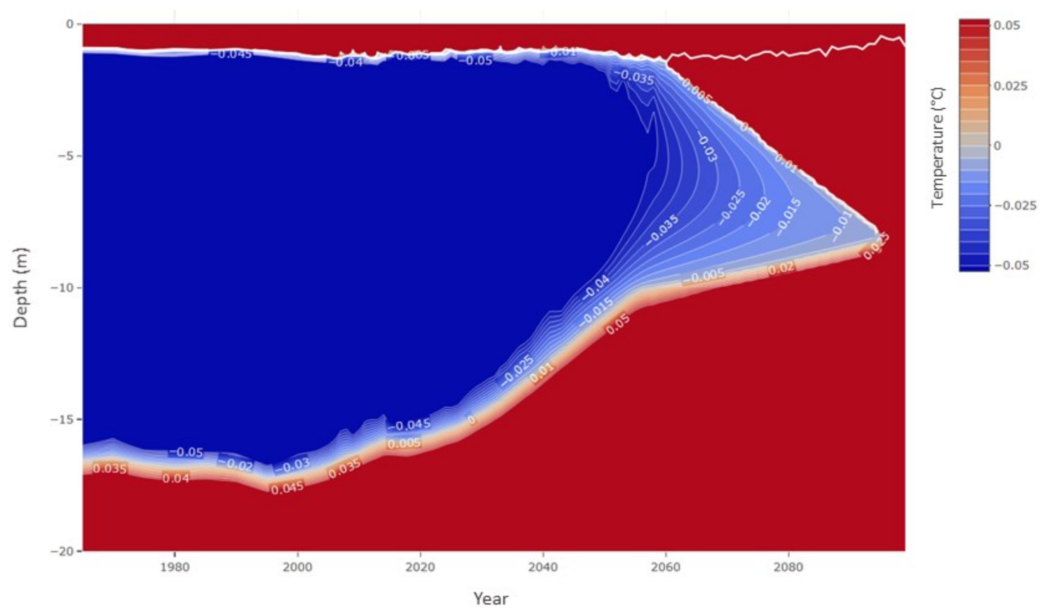

Figure 7-6. Modelled Ground Temperatures (1965-2099) at Unburned WB Site Under RCP8.5. Organic mat accumulation did not occur. The base of the active layer, approximated by a temperature threshold of -0.025°C or an unfrozen moisture content of 0.11, is shown as a white line.

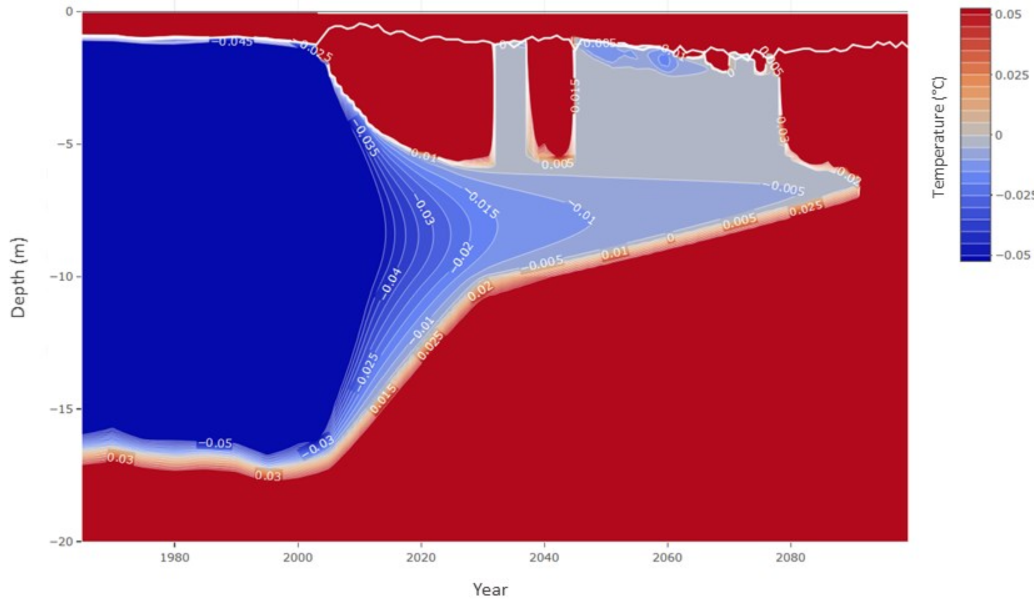

Figure 7-7. Modelled Ground Temperatures (1965-2099) Following Low Burn Severity Fire in 2004 at the WB Site Under RCP4.5. Organic mat accumulation did not occur. The base of the active layer, approximated by a temperature threshold of -0.025°C or an unfrozen moisture content of 0.11, is shown as a white line.

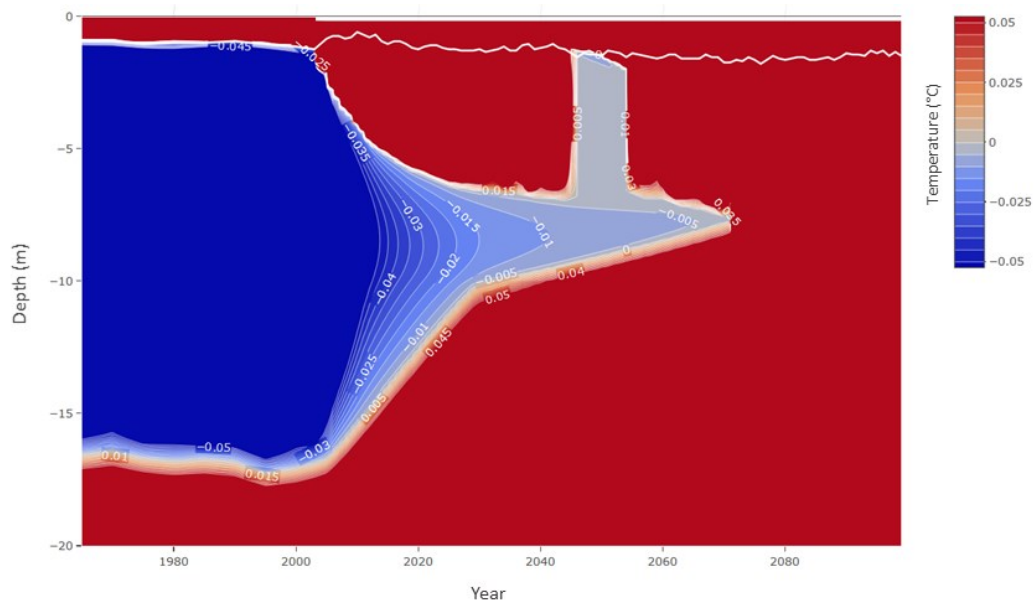

Figure 7-8. Modelled Ground Temperatures (1965-2099) Following High Burn Severity Fire in 2004 at the WB Site Under RCP4.5. Organic mat accumulation did not occur. The base of the active layer, approximated by a temperature threshold of -0.025°C or an unfrozen moisture content of 0.11, is shown as a white line.

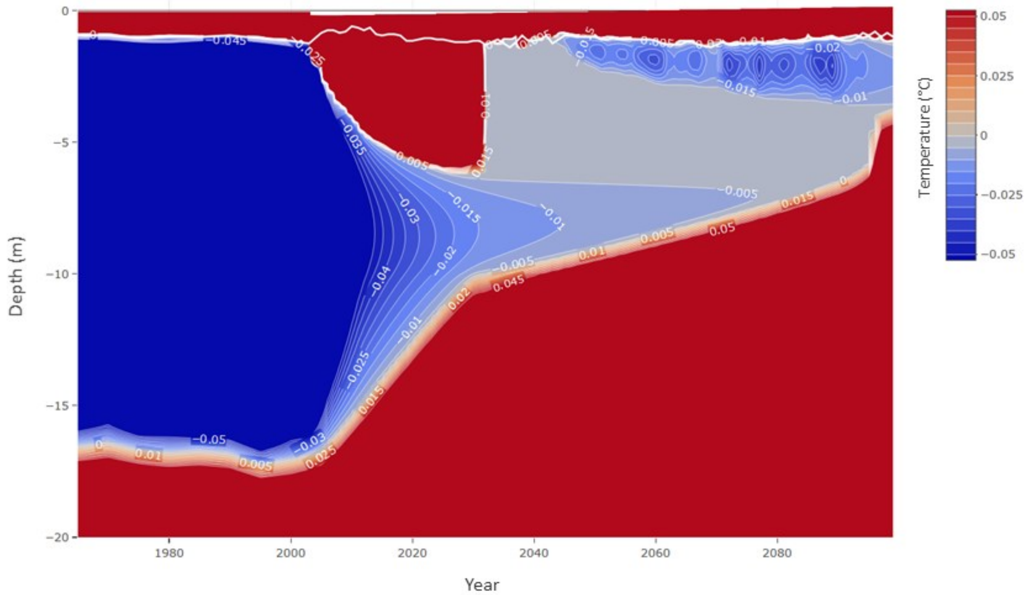

Figure 7-9. Modelled Ground Temperatures (1965-2099) Following High Burn Severity Fire in 2004 at the WB Site Under RCP4.5. Organic material accumulated at 3.6 mm/year from 2004 to 2099. The base of the active layer, approximated by a temperature threshold of -0.025°C or an unfrozen moisture content of 0.11, is shown as a white line.

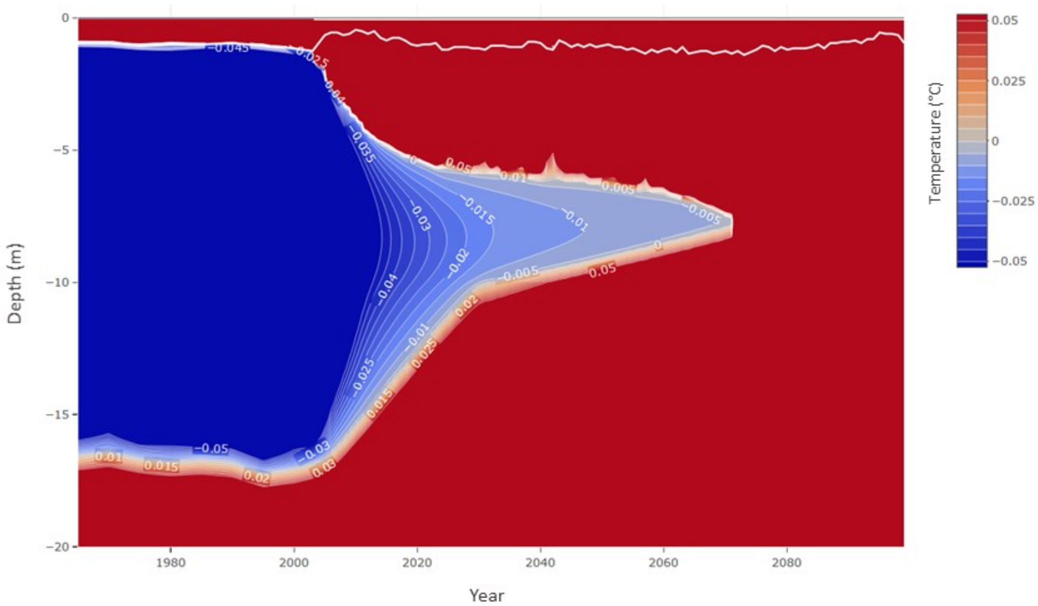

Figure 7-10. Modelled Ground Temperatures (1965-2099) Following Low Burn Severity Fire in 2004 at the WB Site Under RCP8.5. Organic mat accumulation did not occur. The base of the active layer, approximated by a temperature threshold of -0.025°C or an unfrozen moisture content of 0.11, is shown as a white line.

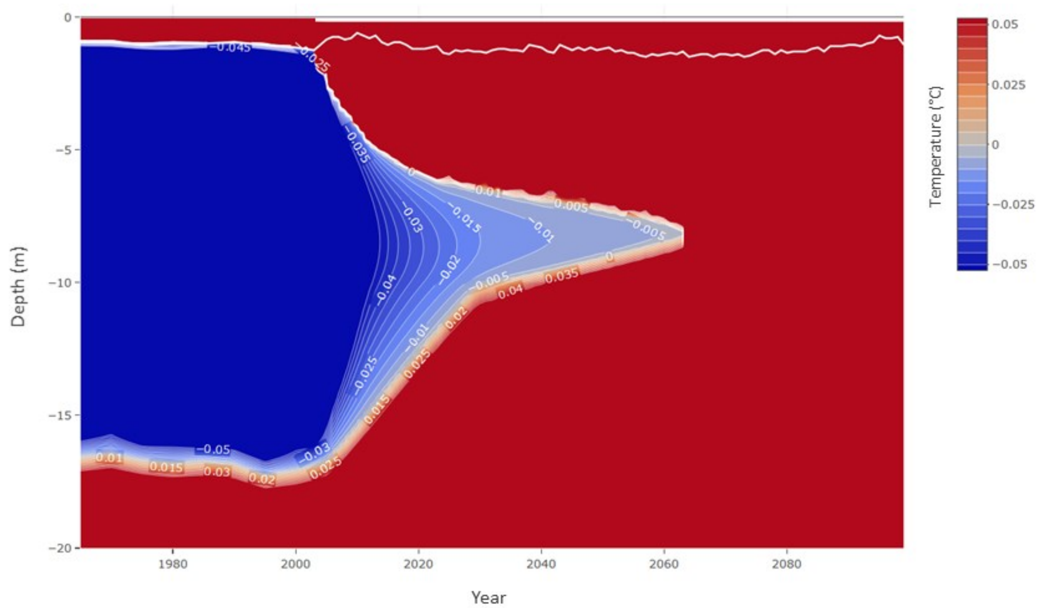

Figure 7-11. Modelled Ground Temperatures (1965-2099) Following High Burn Severity Fire in 2004 at the WB Site Under RCP8.5. Organic mat accumulation did not occur. The base of the active layer, approximated by a temperature threshold of -0.025°C or an unfrozen moisture content of 0.11, is shown as a white line.